



## 저작자표시 2.0 대한민국

이용자는 아래의 조건을 따르는 경우에 한하여 자유롭게

- 이 저작물을 복제, 배포, 전송, 전시, 공연 및 방송할 수 있습니다.
- 이차적 저작물을 작성할 수 있습니다.
- 이 저작물을 영리 목적으로 이용할 수 있습니다.

다음과 같은 조건을 따라야 합니다:



저작자표시. 귀하는 원저작자를 표시하여야 합니다.

- 귀하는, 이 저작물의 재이용이나 배포의 경우, 이 저작물에 적용된 이용허락조건을 명확하게 나타내어야 합니다.
- 저작권자로부터 별도의 허가를 받으면 이러한 조건들은 적용되지 않습니다.

저작권법에 따른 이용자의 권리는 위의 내용에 의하여 영향을 받지 않습니다.

이것은 [이용허락규약\(Legal Code\)](#)을 이해하기 쉽게 요약한 것입니다.

[Disclaimer](#) 

공학박사 학위논문

**Enhancing the Performance and Stability of  
Electrode Materials for Photovoltaic Devices**

태양전지용 전극 물질의 성능 및  
수명 특성 향상 연구

2015년 2월

서울대학교 대학원

재료공학부

김 재 익

# Enhancing the Performance and Stability of Electrode Materials for Photovoltaic Devices

## 태양전지용 전극 물질의 성능 및 수명 특성 향상 연구

지도교수 박 병 우

이 논문을 공학박사 학위논문으로 제출함  
2014년 12월

서울대학교 대학원  
재료공학부  
김 재 익

김재익의 공학박사 학위논문을 인준함.

2014년 12월

위 원 장	김 기 범
부위원장	박 병 우
위 원	박 찬
위 원	유 상 임
위 원	박 예 준

Ph.D. Thesis

**Enhancing the Performance and Stability of  
Electrode Materials for Photovoltaic Devices**

**Jae Ik Kim**

February 2015

WCU Hybrid Materials Program,

Department of Materials Science and Engineering,

Seoul National University

## **Abstract**

Toward high efficiency and low cost as the ultimate goal of solar cells, the electrode materials have been intensively researched due to its important roles in photo-conversion efficiency. In case of transparent contact electrode, ZnO-based transparent conducting oxides (TCOs) have received much attention due to its excellent light-scattering performance and abundance. However, the stability in humid environment is still an unsolved problem, which prevents ZnO-based TCOs from actual applications in the solar cells requiring long-term stability. Therefore, full understanding of the underlined mechanisms on TCO degradation in harsh environments is critical for reliability.

In this thesis, the stability and degradation mechanisms of ZnO-based TCOs are examined under the humid and hot atmosphere. The Chap. 1 describes the general scientific context and the research field in which this thesis is included. First, a brief overview of the photovoltaic technologies and advantages of the thin-film silicon solar cells are given. Second, the TCO materials are introduced and their use as a transparent contact electrode in solar cell is explained. Finally, the motivation and objectives of this work are summarized.

In Chap. 2, the degradation mechanism of transparent conducting film is examined in detail. A complete understanding of the reliability for ZnO based transparent conducting oxides is essential for actual applications in photovoltaic

devices or displays requiring long-term stability. The stability and degradation mechanisms under a controlled damp-heat environment (humid and hot atmosphere) for sputter-deposited aluminum-doped zinc oxide (ZnO:Al) thin films were quantitatively studied. The continuous degradations of carrier concentration and mobility with the Fermi-level shift were observed, and these behaviors were resolved by separating the changes in the carrier-transport characteristics of the intragrain and grain boundary. By correlating the temperature dependence of electrical characteristics with x-ray photoelectron spectroscopy, the degradation is well explained by the increase of chemisorbed OH<sup>-</sup> in the grain boundaries. Lastly, all results and conclusion of the thesis are summarized in Chap. 3.

**Keywords:** Thin-Film Solar Cells, Photovoltaics, Transparent Conducting Oxides, Al-doped ZnO, Damp-Heat Test, Fermi-Level Shift, Effective Energy Barrier, Band Diagram

**Student Number: 2010-30776**

# Table of Contents

<b>Abstract</b>	<b>i</b>
<b>List of Figures</b>	<b>v</b>
<b>List of Table</b>	<b>xv</b>
<b>Chapter 1. Overview</b>	<b>1</b>
<b>1.1. General Introduction to Solar Cells</b>	<b>1</b>
<b>1.1.1. Classification of Solar Cells</b>	<b>5</b>
<b>1.1.2. Efficiency of Solar Cells</b>	<b>5</b>
<b>1.1.3. Si Solar Cells</b>	<b>9</b>
<b>1.1.4. Transparent Contacts</b>	<b>9</b>
<b>1.2. Transparent Conducting Oxide</b>	<b>12</b>
<b>1.2.1. Overview of Transparent Conducting Oxide</b>	<b>12</b>
<b>1.2.2. Structural Characteristic of ZnO</b>	<b>13</b>
<b>1.2.3. Electronic Characteristic of ZnO</b>	<b>15</b>
<b>1.2.3.1. Intrinsic Defects in ZnO</b>	<b>17</b>
<b>1.2.4. Electrical Transport in Polycrystalline ZnO films</b>	<b>17</b>
<b>1.2.4.1. Dislocating Scattering</b>	<b>18</b>
<b>1.2.4.2. Grain Barrier Limited Transport</b>	<b>20</b>
<b>1.2.5. Optical Characteristic of ZnO</b>	<b>27</b>
<b>1.2.6. ZnO-based TCO in Thin Film Silicon Solar Cells</b>	<b>31</b>
<b>1.3. Motivation and Objectives</b>	<b>34</b>
<b>1.4. References</b>	<b>39</b>
<b>Chapter 2. Quantitative Analyses of Damp-Heat-Induced Degradation in     Transparent Conducting Oxides</b>	<b>45</b>
<b>2.1. Introduction</b>	<b>45</b>
<b>2.2. Experimental Section</b>	<b>46</b>

2.3. Results and Discussion	47
2.4. Conclusions	71
2.5. References	72
<b>Chapter 3. Summary</b>	<b>78</b>
<b>Appendix</b>	
<b>A. 1. Oriented Hierarchical TiO<sub>2</sub> Nanotubes on Flexible Substrate: Evolution of Nanostructure and Application in Dye-Sensitized Solar Cells</b>	<b>80</b>
A.1.1. Introduction	80
A.1.2. Experimental Section	82
A.1.2.1. Synthesis of 1-D Nanostructures	82
A.1.2.2. Device Fabrication	83
A.1.2.3. Characterization	84
A.1.3. Results and Discussion	85
A.1.4. Conclusions	103
A.1.5. References	104
<b>A. 2. Surface-Plasmon-Coupled Photoluminescence from CdS Nanoparticles with Au Films</b>	<b>110</b>
A.2.1. Introduction	110
A.2.2. Experimental Section	111
A.2.3. Results and Discussion	113
A.2.4. Conclusions	118
A.2.5. References	121
<b>A. 3. List of Publications and Presentations</b>	<b>127</b>
A.3.1. Publications (International)	127
A.3.2. Presentation (International)	128
A.3.3. Presentation (Domestic)	130
국문 초록	131
감사의 글	133



## List of Figures

### Chapter 1.

Fig. 1-1. (Color) Schematic for photovoltaic process and loss process in  $pn$ -junction solar cell: (1) lattice thermalization losses, (2) transparency loss, (3) recombination loss, (4) junction loss, (5) contact voltage loss. From Ref. [2].

Fig. 1-2. (Color) Solar cells classification: silicon type, compound semiconductor type, and organics.

Fig. 1-3. (Color) Typical structures of conventional solar cells: (a) CdTe, (b) CIGS, and (c) thin film Si solar cell. From Ref. [3].

Fig. 1-4. (Color) Best research-cell efficiency from National Renewable Energy Laboratory (NREL). From Ref. [4].

Fig. 1-5. (Color) Schematic structure of  $pn$ -junction silicon solar cell.

Fig. 1-6. (Color) Schematic comparison of the optical path through a flat interface (a) and a rough interface (b) of the thin-film solar cell. The

rough interface scattered the incoming light leading to a longer optical path through the active material.

Fig. 1-7. (Color) The crystal structure of ZnO: perspective view perpendicular to the  $c$ -axis (left) and view along the  $c$ -axis on the zinc terminated plane (right). From Ref. [19].

Fig. 1-8. (Color) The energy levels of native defects in ZnO. The donor defects are  $Zn_i^{\bullet\bullet}, Zn_i^{\bullet}, Zn_i^{\times}, V_o^{\bullet\bullet}, V_o^{\bullet}, V_o$ , and the acceptor defects are  $V_{Zn}^{\bullet\bullet}, V_{Zn}^{\bullet}$ , respectively. From Ref. [16].

Fig. 1-9. (Color) The Grain size  $L$ , doping  $N$ , and with grain barriers of height  $\Phi_B$  caused by a continuous distribution of electron trap states of density  $N_t$ . Two different transport paths for electrons are indicated as thermionic emission across the barrier TE and tunneling through the barrier  $T$ . From Ref. [19].

Fig. 1-10. (Color) Barrier height at the grain barriers as a function of the electron concentration in grains (grain size  $L = 100$  nm and trap density  $N_t = 5 \times 10^{12} \text{ cm}^{-2}$ ). From ref. [19].

Fig. 1-11. (Color) Schematic band diagrams in the grains for different doping concentration  $N$  in the grain size of  $L$ . The situations (1-3) correspond to carrier concentrations (1-3) in Fig. 1-10. The barrier height increases with increasing  $N$  up to a maximum at  $N_{\max} = N/L$  (2). Further increasing  $N$  decreases the barrier height (3). From Ref. [19].

Fig. 1-12. (Color) Schematic band structure with parabolic conduction and valance bands separated by optical bandgap  $E_g^{op}$  (a), after Al doping assumed to have the sole effect of filling the lowest states in the conduction band, so that the  $E_g^{op}$  is widened by a BM effect (b), represents the bandgap renormalization in the case of many-body interaction (c). From Ref. [36].

Fig. 1-13. (Color) Reported resistivity ( $\rho$ ) of impurity-doped binary compound TCO films, 1972–2005: impurity-doped SnO<sub>2</sub> ( $\square$ ), In<sub>2</sub>O<sub>3</sub> ( $\Delta$ ) and ZnO ( $\bullet$ ). From Ref. [12].

Fig. 1-14. (Color) Degradation of carrier concentration and Hall mobility of ZnO:Al (four different thicknesses) after damp-heat (humid and hot

atmosphere) treatment. From Ref. [45].

Fig. 1-15. (Color) Current-voltage characteristics of an unencapsulated a-Si:H solar cell fabricated with LPCVD ZnO:B electrodes for various damp heat exposure (80°C, 100% humidity) times. From Ref. [48].

Fig. 1-16. (Color) Optical and Hall mobility and (b) optical and Hall carrier density of the 2  $\mu\text{m}$  thick LPCVD ZnO:B film as a function of the damp heat exposure (40 °C, 100% humidity) time. From Ref. [48].

## Chapter 2.

Fig. 2-1. (Color) Hall resistivity, carrier mobility, and carrier concentration of ZnO:Al films as a function of damp-heat (DH) exposure time.

Fig. 2-2. (Color) Plot of  $\alpha^2$  vs.  $h\nu$  near the bandedge for ZnO:Al films at various DH exposure times. For comparison, the absorption from nondegenerate ZnO is also included.

Fig. 2-3. (Color) Comparison of the XPS core-level spectra (Zn 2p peak) of the ZnO and ZnO:Al films with and without DH exposure.

Fig. 2-4. (Color) Comparison of the XPS core-level spectra of the ZnO and ZnO:Al films with and without DH exposure. Deconvoluted O 1s peak of the films. Each inset shows a scheme of the chemisorbed hydroxyl groups along the grain boundaries and accumulated positive carriers towards the depleted regions at the given DH exposure condition.

Fig. 2-5. (Color) X-ray diffraction of ZnO:Al films at various DH exposure times. The peak intensities and positions from the hexagonal ZnO

(JCPDS #36-1451) are shown as solid bars.

Fig. 2-6. (Color) Schematic band diagrams for the ZnO and ZnO:Al films (with and without DH exposure). The Fermi-level shift (from the XPS spectra of Fig. 2-3), band-filling change (from the carrier concentration (Fig. 2-1) and Eq. (2)), and the optical bandgap  $E_g^{op}$  (from Fig. 2-2) are summarized with a schematic bandgap renormalization. The Fermi level for the nondegenerate ZnO was assumed to be  $\sim 0.3$  eV below the conduction-band minimum [24].

Fig. 2-7. (Color) IR reflectance with various DH exposure times, with the fitting results (solid lines) using the Drude model.

Fig. 2-8. (Color) Changes in the grain-boundary resistivity  $\rho_{GB}$  (calculated by Eq. (5)), Hall resistivity  $\rho_{Hall}$ , and intragrain resistivity  $\rho_{intra}$  as a function of DH exposure time.

Fig. 2-9. (Color) Temperature dependence on electrical characteristics with various DH exposure times: Hall-carrier concentration.

Fig. 2-10. (Color) Temperature dependence on electrical characteristics with various DH exposure times: Hall-carrier mobility.

Fig. 2-11. (Color) Temperature dependence on electrical characteristics with various DH exposure times. Plot of  $\mu_{Hall}\sqrt{T}$  vs. inverse temperature, with the fitted lines by Eq. (15).

Fig. 2-12. (Color) Temperature dependence on electrical characteristics with various DH exposure times: Changes in the effective energy barrier  $E_{b,eff}$  obtained from the slopes in Fig. 2-11 as a function of DH exposure.

Fig. 2-13. (Color) Schematic figure showing the change in effective grain-boundary barrier  $E_{b,eff}$  (Figs. 2-11 and 12) caused by the damp-heat tests, with other energy levels from Fig. 2-6.

## **Appendix 1.**

Fig. A1-1. (Color) X-ray diffraction of nanostructured titanium foils at various hydrothermal dehydration times.

Fig. A1-2. (Color) Cross-sectional SEM images of 1-D nanostructures on titanium foils at various hydrothermal dehydration times: (a-b) 0 h, (c) 1.5 h, (d) 2.5 h, and (e) 4.5 h. (f) Grain size along the [100] and [001] directions for the nanostructures as a function of hydrothermal dehydration time.

Fig. A1-3. (Color) Typical TEM and high-resolution TEM images of prepared nanostructures at various hydrothermal dehydration times: (a) 0 h, (b) 1.5 h, and (c) 4.5 h. (d) Schematic crystallographic structure of single-crystal TiO<sub>2</sub> (anatase).

Fig. A1-4. (Color) X-ray diffraction of nanostructured titanium foils with various hydrothermal dehydration times (after annealing at 450°C for 1 h).

Fig. A1-5. (Color) Grain size along the [100] and [001] directions for the nanostructures as a function of hydrothermal dehydration time (after



annealing at 450°C for 1 h). The grain size of TiCl<sub>4</sub> treated sample is also shown.

Fig. A1-6. (Color) Photocurrent-voltage curves of the DSSCs based on the nanostructured photoanodes (on the titanium foil) at various hydrothermal dehydration times.

Fig. A1-7. (Color)) UV-Vis absorption spectra of N719 desorbed from photoanodes in 0.1 M NaOH solution.

Fig. A1-8. (Color) Experimental decay results of  $V_{oc}$  for the DSSCs. The inset shows the electron lifetimes derived from the decay results.

Fig. A1-9. (Color) Nyquist plots for the DSSCs (hydrothermal dehydration time of 4.5 h) with and without TiCl<sub>4</sub> treatment.

Fig. A1-10. (Color) Schematic flow of nanostructured electrodes with various treatments, and a scheme for the crystal structures of H<sub>2</sub>Ti<sub>2</sub>O<sub>5</sub>·H<sub>2</sub>O and anatase TiO<sub>2</sub> in the inset.

## Appendix 2.

Fig. A2-1. (Color) Photoluminescence spectra of CdS nanoparticles with different thicknesses of Au film: (a) as-deposited and (b) annealed at 400°C for 30 min. The inset shows a schematic figure of a sample geometry and PL configuration.

Fig. A2-2. (Color) Dispersion relation of surface plasmon at a planar Au/PMMA interface of a three-layer system for various Au film thicknesses. The light line in PMMA ( $n \cong 1.61$  for the index of refraction) is shown as a dashed line. The inset shows the calculated density of surface-plasmon (SP) states as a function of photon energy for different Au thicknesses.

Fig. A2-3. (Color) Diffused reflectance of Au film on glass substrate for various thicknesses of Au film: (a) as-deposited and (b) annealed at 400°C for 30 min.

Fig. A2-4. (Color) (a) The calculated PL enhancement factor and lateral roughness as a function of nominal thickness of Au film with and without annealing. The density of surface-plasmon (SP) states at

2.25 eV (from the inset of Fig. A2-2) is shown as a dashed line. The AFM images of Au film sputtered on glass substrate at (b) 4.5 nm thickness without annealing, (c) 4.5 nm thickness with annealing, (d) 30 nm thickness without annealing, and (e) 30 nm thickness with annealing.

## List of Table

### Chapter 2.

Table. 2-1. Fitted parameters ( $\omega_p$ ,  $\tau$ ) and calculated values of optical carrier concentration ( $n_{opt}$ ) and mobility ( $\mu_{opt}$ ) for the ZnO:Al films with various DH exposure times.

Table. 2-1. Measured values of Hall-carrier concentration ( $n_{Hall}$ ) and mobility ( $\mu_{Hall}$ ), calculated values of intragrain-carrier concentration ( $n_{opt}$ ), mobility ( $\mu_{intra}$ ), Hall resistivity ( $\rho_{Hall}$ ), intragrain resistivity ( $\rho_{intra}$ ), and grain-boundary resistivity ( $\rho_{GB}$ ) for the ZnO:Al films with various DH exposure times.

### Appendix 1.

Table A1-1. Photovoltaic performance of the DSSCs. Short-circuit current density ( $J_{sc}$ ), open-circuit voltage ( $V_{oc}$ ), fill factor ( $FF$ ), power-conversion efficiency ( $\eta$ ) of the DSSCs, dye adsorption, and average thickness with various hydrothermal dehydration times on the nanostructured photoelectrodes.

# Chapter 1. Overview

## 1.1. General Introduction to Solar Cells

A Solar cell (also called photovoltaic cell) is an electrical device that converts the photon energy directly into electricity through the photovoltaic effect [1]. In 1839, first photovoltaics were discovered by French physicist Edmond Becquerel. In his experiment, silver chloride (AgCl) or silver bromide (AgBr) was placed in an acidic solution and illuminated while connected to platinum electrodes, generating voltage and current. The first practical photovoltaic cell using silicon *pn* junction was developed by Daryl Chapin, Calvin Fuller, and Gerald Pearson who were at Bell Labs in 1954.

The schematic illustration for solar cell operation is shown in Fig. 1-1 [2]. In general, *pn*-junction solar cell is composed of semiconductor diode. The semiconductor absorbs incoming photons and converts them into electron-hole pairs. In an ideal case, the incident photons with an energy  $h\nu > E_{gap}$  will contribute to photogeneration. Therefore, the maximum limit for the photogenerated current density is limited by the number of photons with higher energy than bandgap of absorber layer. In the second step of the energy conversion process, the generated electrons and holes are separated and drifted to the cathode (or anode) by internal electric field. The solar-cell efficiency ( $\eta$ ) at

maximum power point is given by three key parameters, open-circuit voltage ( $V_{oc}$ ), short-circuit current density ( $J_{sc}$ ), and the fill factor ( $FF$ ):  $\eta = (V_{oc} J_{sc} FF) / P_{in}$ . The incident power ( $P_{in}$ ) is decided by the properties of the light spectrum incident upon the solar cell.

The operation process of solar cell is as follows. The  $V_{oc}$  is limited by bandgap energy, cannot exceed  $E_{gap}/q$ , and it has lower values than bandgap energy because of the charge recombination. At the  $V_{oc}$ , all the photo carriers recombine within the solar cell diode. In case of the cell with the minimized recombination characteristics, the  $V_{oc}$  can be more closely approach the limit value ( $E_{gap}/q$ ). The  $I_{sc}$  is current flux which is collected by electrode at zero voltage, and it is related to the number of absorbing photon and charge collection capability of electrode.

Figure 1-1 also shows a loss mechanisms that limit the efficiency of *pn*-junction solar cells. The most significant loss mechanisms are due to relaxation of ‘hot’ carriers that are created upon absorption of a high energy photon (process 1) and transmission of photons with energies below the bandgap of the absorber material (process 2). The excess energy of high energy photons is rapidly dissipated as heat by thermalization of the electron and hole to the edges of the conduction and valence band. Especially in solar cells based on small band-gap semiconductors, these losses are more significant. On the other hand, the transmission losses contribute more to the losses for wider band-gap solar cells,

because a large part of the solar spectrum cannot be absorbed. Process 3 shows the recombination of electron-hole pairs, and this loss process can be minimized through maintaining long minority carrier lifetimes in the semiconductor materials. Lastly, the process 4 and 5 exhibit the junction loss and contact voltage loss, respectively.

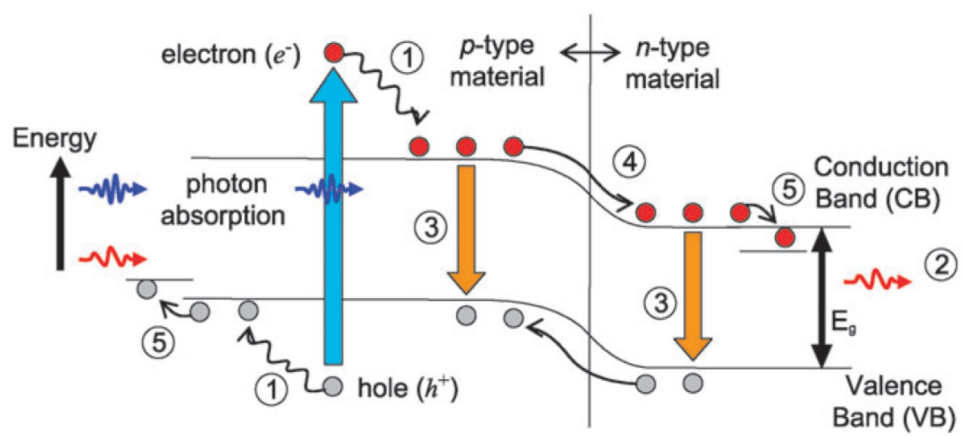


Fig. 1-1. (Color) Schematic for photovoltaic process and loss process in  $pn$ -junction solar cell: (1) lattice thermalization losses, (2) transparency loss, (3) recombination loss, (4) junction loss, (5) contact voltage loss. From Ref. [2].



### **1.1.1. Classification of Solar Cells**

The solar cells could be divided into inorganic type and organic type, as shown in Fig. 1-2. Silicon type is classified with crystalline and amorphous by their crystallinity and also divided into bulk types or thin film types their thickness. Compound semiconductor type has II-VI, III-VI, III-V compounds that have high efficiency, and they applied to satellites. For example, typical structures of conventional compound solar cells are shown in Fig. 1-3 [3]. The organic types have polymer solar cell and dye-sensitized solar cell (DSSC) which have low energy conversion efficiency compare to silicon or compound semiconductor type solar cells. However, the advantages of organic types are to fabricate low cost and to apply to flexible solar cells. In additional, DSSCs are suitable to adapt on building integrated photovoltaic system because they have high transparency, various color and shape. However, the organic type solar cells has the advantages of manufacturing costs and applicability of flexible.

### **1.1.2. Efficiency of Solar Cells**

M. A. Green et. al. have been reported annually a report that is listed the highest independently confirmed efficiencies for solar cells (Fig. 1-4) [4]. The highest efficiency of DSSCs is 12.3% that was reported by Grätzel group in 2011.

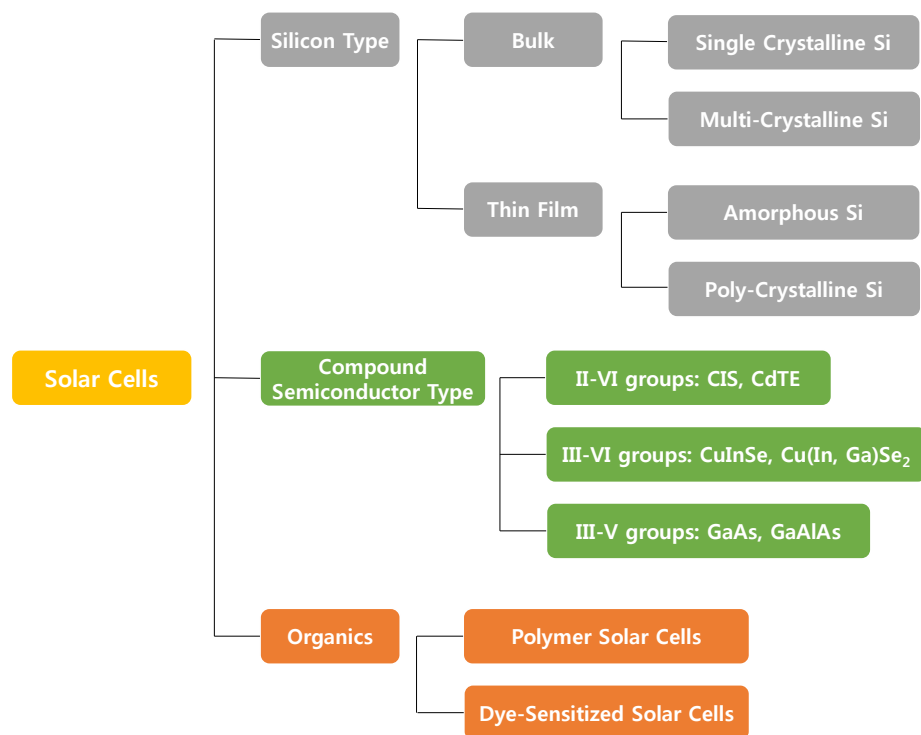


Fig. 1-2. (Color) Solar cells classification: silicon type, compound semiconductor type, and organics.

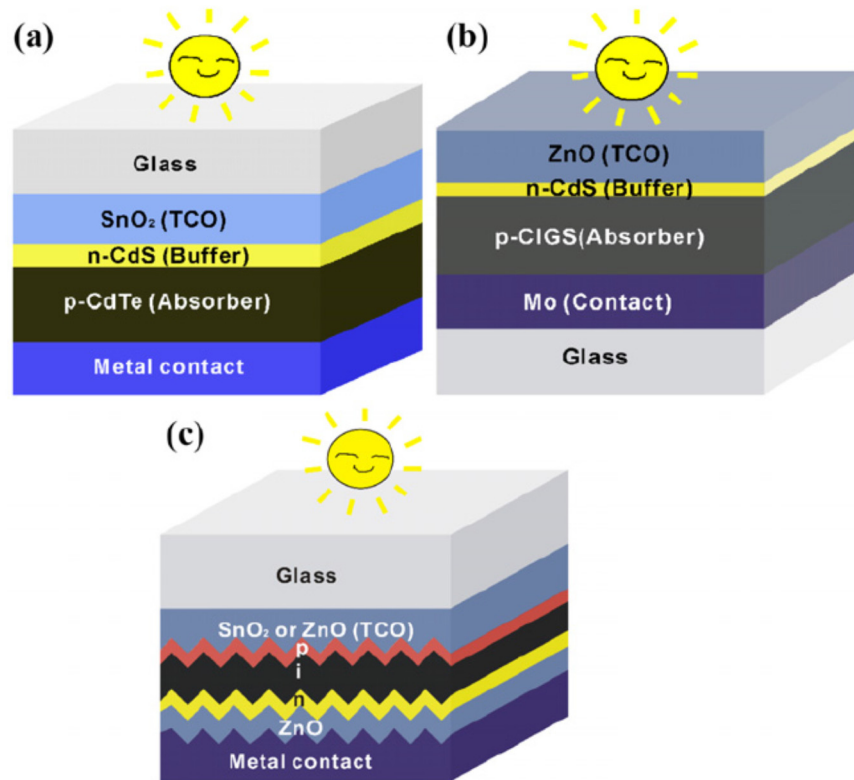


Fig. 1-3. (Color) Typical structures of conventional solar cells: (a) CdTe, (b) CIGS, and (c) thin film Si solar cell. From Ref. [3].

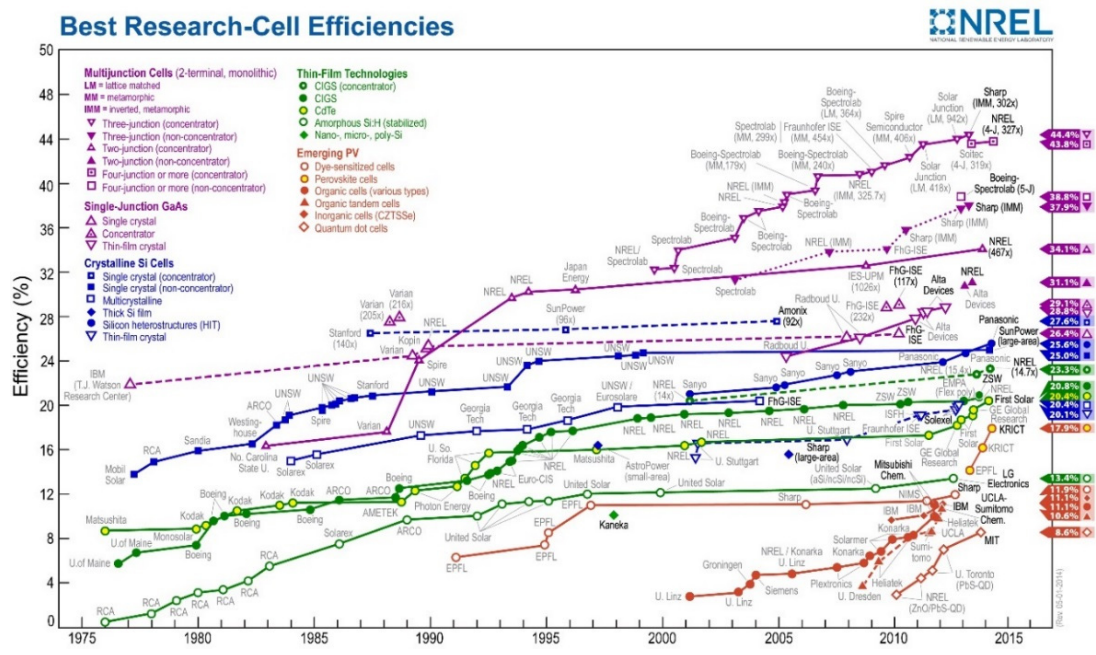


Fig. 1-4. (Color) Best research-cell efficiency from National Renewable Energy Laboratory (NREL). From Ref. [4].

### 1.1.3. Si Solar Cells

The silicon (Si) based solar cells are semiconductor diodes that consist of  $pn$  junction and convert the photo energy into electricity energy as shown in Fig. 1-5.

### 1.1.4. Transparent Contacts

The electrical current produced by the solar cells is extracted through electrical contact layers deposited on each side of the  $pn$  structure. The contact layer deposited on the face of the cell that is exposed to the light source, needs to be transparent in order to let the photon enter into the solar cell. To achieve this, the transparent conductive oxides (TCOs) having high electrical conductivity and high optical transparency are widely used. The most commonly used TCO are indium tin oxide (ITO), fluorine-doped  $\text{SnO}_2$  (FTO), and impurity doped ZnO.

On the other hand, due to particularly thin absorber layer (typically 300 nm for  $\alpha$ -Si:H cells and 2  $\mu\text{m}$  for  $\mu\text{cSi:H}$  cells [5]) of thin-film silicon solar cells, a front contact possessing a surface morphology that scatters the light is necessary to achieve a high current. As shown in Fig. 1-6, rough diffusing layers considerably increase the light path through the absorber and thus the amount of absorbed photons. This light scattering phenomenon can increase the solar cell current by 20~40 % [6]. The excellent light scattering properties can be achieved via sputter deposition and surface texturing by wet-chemical etching, particularly for front TCOs [7].

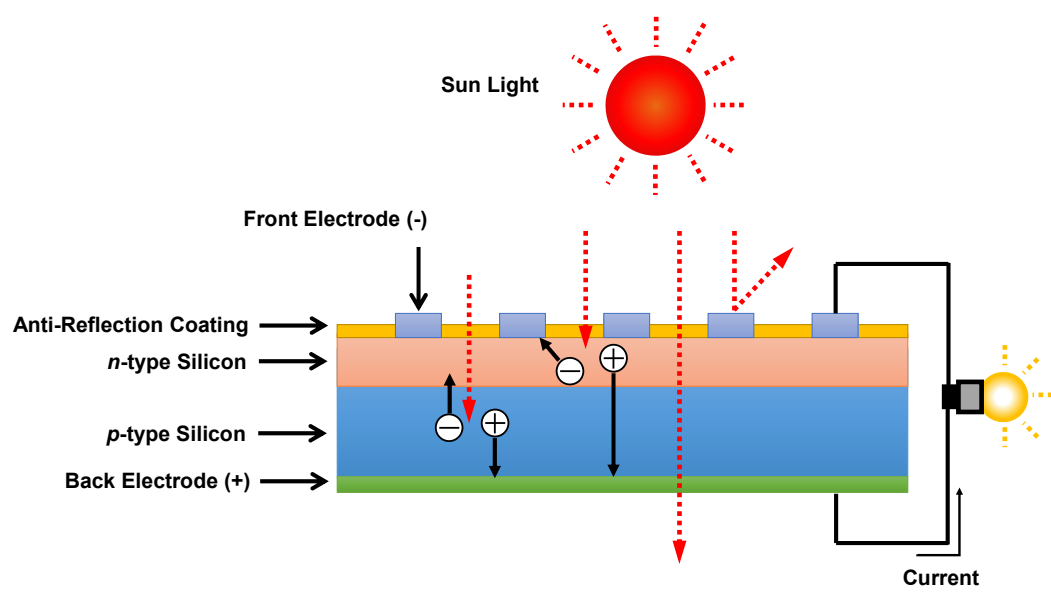


Fig. 1-5. (Color) Schematic structure of  $pn$ -junction silicon solar cell.

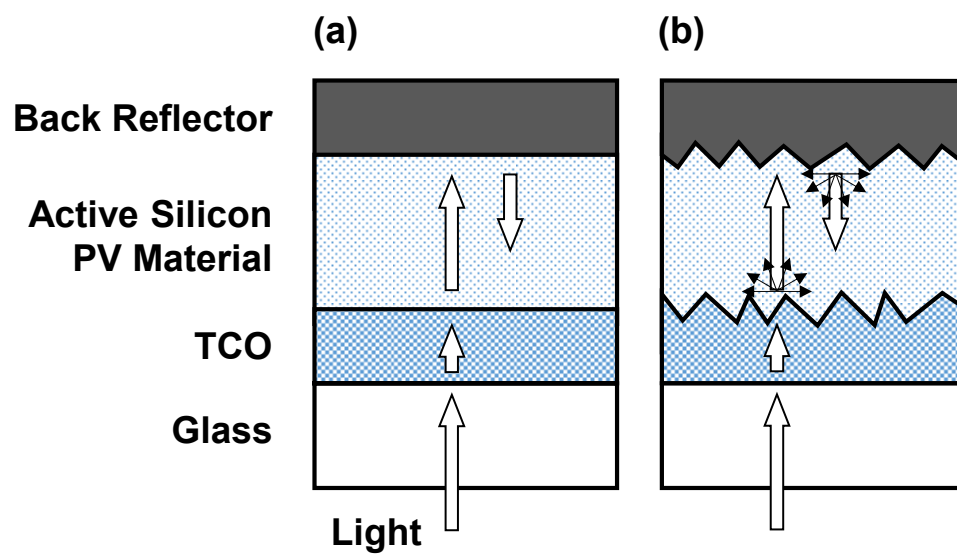


Fig. 1-6. (Color) Schematic comparison of the optical path through a flat interface (a) and a rough interface (b) of the thin-film solar cell. The rough interface scattered the incoming light leading to a longer optical path through the active material.

## **1.2. Transparent Conducting Oxide**

### **1.2.1. Overview of Transparent Conducting Oxide**

Most wide bandgap materials are electrically insulating, while most conducting materials are opaque to light at visible wavelengths. However, there are exceptions to this rule - a class of oxide semiconductors which are rather good conductors of electricity while simultaneously being transparent in the visible region of the electromagnetic spectrum - have generated much interest. In spite of being known about for over half a century, there remains substantial controversy over the origins of conductivity in these materials, making them one of the least understood classes of semiconductor today.

Termed transparent conducting oxides (TCOs), these materials have already found extensive practical application in devices requiring a transparent contact. Typical examples include current-spreading layers in light-emitting diodes (LED), transparent contacts in solar cells and liquid crystal display (LCD), thermal insulation for windows, and electrochromatic, or smart, windows [8-11].

In general, TCOs for use as thin film electrodes in solar cells should have a minimum carrier concentration on the order of  $10^{20} \text{ cm}^{-3}$  for low resistivity and a bandgap higher than 3.2 eV to avoid absorption of light over most of the solar spectra [12]. Mobility in these films is limited by ionized impurity scattering and is on the order of  $40 \text{ cm}^2/\text{Vs}$ .



### 1.2.2. Structural Characteristic of ZnO

ZnO crystal has a hexagonal wurtzite and cubic zincblende structure. The wurtzite structure is more stable at ambient conditions. In general, deposited ZnO films exhibit the preferential texture along the  $c$ -axis ((0001) texture). The Figure 1-7 shows the hexagonal unit cell ( $a = 0.325$  nm,  $c = 0.52066$  nm) of the ZnO, which contains 2 molecules. The oxide and zinc centers are tetrahedral. The zinc atoms are surrounded by oxygen atoms with a nearly tetrahedral form. Along the  $c$ -axis the Zn-O distance is smaller ( $d_{Zn-O} = 0.190$  nm) than for the other three neighboring oxygen atoms ( $d_{Zn-O} = 0.198$  nm) [13].

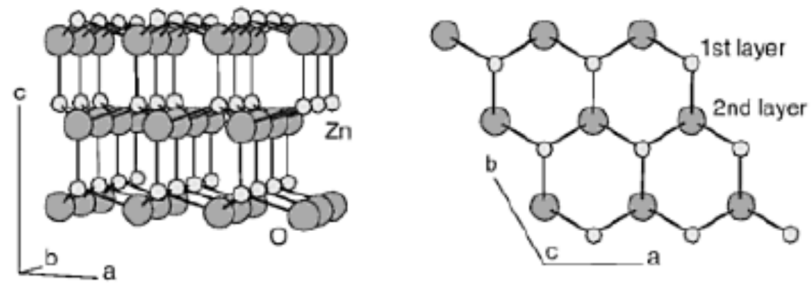


Fig. 1-7. (Color) The crystal structure of ZnO: perspective view perpendicular to the  $c$ -axis (left) and view along the  $c$ -axis on the zinc terminated plane (right). From Ref. [13].

### 1.2.3. Electronic Characteristic of ZnO

ZnO has a relatively large direct bandgap of 3.2-3.4 eV at 300 K. Most of ZnO has *n*-type character, even in the absence of intentional doping [14]. Nonstoichiometry caused by displacement or removal of lattice atoms is typically the origin of *n*-type character [15]. There are some intrinsic defects with different ionization energies in ZnO. Figure 1-8 shows the defect states within the bandgap of ZnO schematically [16]. The notation means: *i* = interstitial site, Zn = zinc, O = oxygen, and *V* = vacancy. The terms indicate the atomic sites, and superscripted terms indicate charges, where a prime indicates negative charge, a dot indicates positive charge, and a cross indicates zero charge, with the charges in proportion to the number of symbols. The oxygen vacancies and Zn interstitials are known to be the predominant ionic defect types [16]. However, the defect dominates in native, undoped ZnO is still a matter of controversy. Meanwhile, controllable *n*-type doping can be achieved by substituting Zn with group-III elements such as In, Ga, Al.

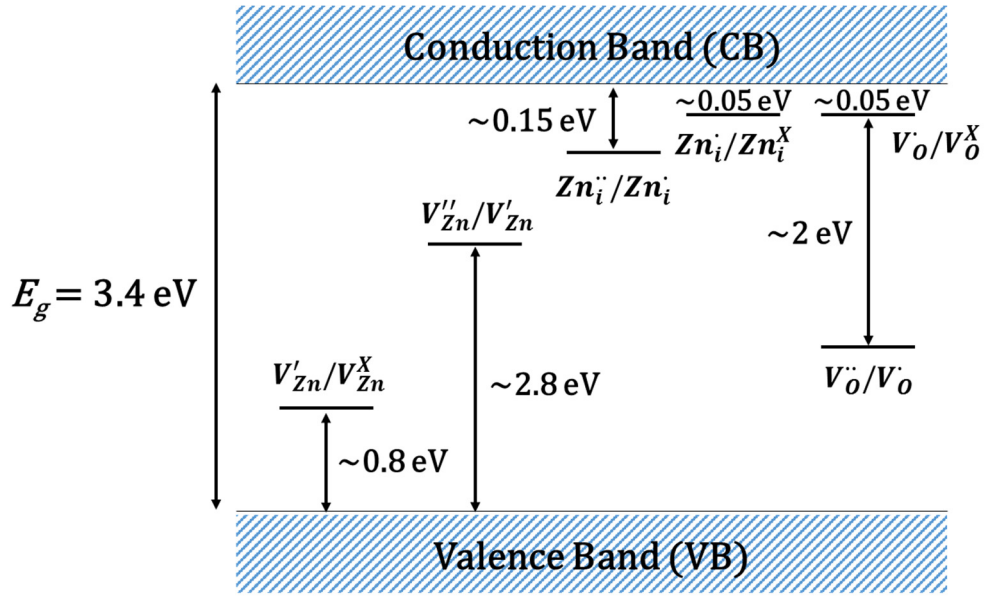


Fig. 1-8. (Color) The energy levels of native defects in ZnO. The donor defects are  $\text{Zn}^{\bullet\bullet}_i, \text{Zn}^{\bullet}_i, \text{Zn}^{\text{X}}_i, V^{\bullet\bullet}_\text{O}, V^{\bullet}_\text{O}, V_\text{O}$ , and the acceptor defects are  $V''_{\text{Zn}}, V'_{\text{Zn}}$ , respectively. From Ref. [16].

### **1.2.3.1. Intrinsic Defects in ZnO**

The native defects have long been thought to be a dominant factor controlling conductivity in TCOs due to the difficulty in achieving high quality material [17]. In particular, the size mismatch between the rather large metal cations and small oxygen anions in these compounds would natively be expected to make oxygen vacancies [18]. However, with recent advances in growth techniques, it has become possible to grow thin films of oxide materials, as required for device applications, with rather high structural quality [19,20]. But, oxygen vacancies are still regarded as the primary cause of conductivity in TCOs, and this remains a contentious issue.

### **1.2.4. Electrical Transport in Polycrystalline ZnO films**

Electrical properties of polycrystalline ZnO films were investigated by Hartnagel, Minami, and Ellmer [21-23]. With respect to the application of the ZnO as transparent electrode, it is the aim to achieve a resistivity as low as possible with the constraint of a high transparency, both by increasing the mobility and carrier concentration. Polycrystalline ZnO films usually grow with the *c*-axes of the crystallites oriented approximately perpendicular to the film plane. Thus, the electrical transport in polycrystalline ZnO films, which is measured laterally, occurs generally perpendicular to the *c*-axes of the crystallites.

### 1.2.4.1. Dislocating Scattering

The dislocating scattering process is a natural scattering process in polycrystalline materials, since polycrystalline films exhibit a high concentration of crystallographic defects, especially dislocations [24]. However, this process is rarely used to explain experimental data of carrier transport in polycrystalline semiconductors and especially transparent conducting oxides, because the fact that in most works on transport properties of polycrystalline films the density of defects was not determined. Pödör investigated the *n*-type Ge crystals and could his results describe by taking into account scattering by charged dislocations leading to a mobility given by [25]:

$$\mu_{H_{disl}} = r_{H_{disl}} \frac{15\sqrt{2}(\epsilon_r)^{3/2} a^2 \sqrt{nkT}}{4\pi e^3 r^2 \sqrt{m^*} N_{disl}}, \quad (1)$$

where  $a$  is the distance between acceptor centers along the dislocation line that catch electrons from the crystalline volume,  $f$  is the occupation number of these acceptors,  $N_{disl}$  is the density of dislocations, and  $r_{H_{disl}}$  ( $\sim 1.1781$ ) is the Hall factor. Look and Sizelove deduced that the dislocations with a negatively charged core act as scattering centers by using temperature-dependent carrier transport measurements [26]. Recently, the line charge density of dislocations was measured directly by electron holography in ZnO films yielding line charge densities of about  $10^7 \text{ cm}^{-1}$ , and the heteroepitaxial ZnO films grown on GaN films on sapphire substrates were

analyzed by transmission electron microscopy. The films are characterized by the stacking fault density in the range of  $10^{18} \text{ cm}^{-3}$ . These stacking faults are mostly generated by the precipitation of Zn interstitials accompanied by the formation of oxygen vacancies in the vicinity of a stacking fault [27]. Since oxygen vacancies exhibit a charge of  $Z = 2$ , and its scattering power is higher than that of singly ionized dopants like the group III elements in ZnO ( $\text{Al}^+$ ,  $\text{B}^+$ ,  $\text{Ga}^+$ ,  $Z = 1$ ) leading to a reduced mobility.

Recent density-functional calculations have shown that the point defect formation enthalpies in zinc oxide are very small [28]. It is noteworthy that ZnO exhibits a high radiation hardness, which is likely due to a rapid annealing of Frenkel pairs, again caused by low defect formation energies, which lead to high diffusion coefficients [29]. Zinc oxide is a polar semiconductor, thus the electrical charges are induced by stress along the  $c$ -axis. It means that the intrinsic stress, because of lattice mismatch and/or of growth defects, could induce charges at extended defects or grain barriers leading to additional scattering.

#### 1.2.4.2. Grain Barrier Limited Transport

The polycrystalline thin film exhibit a vast amount of grain barriers (depending on their mean grain size), which constitute crystallographically disturbed regions, leading to electronic defects in the bandgap of semiconductors. In modeling the carrier transport, defects are localized at the grain boundaries and act as traps for the majority carriers from the adjoining grains [30]. The trapped electrons set up a negative charge at the grain boundaries which gives rise to a depletion region in the grains due to the accumulation of counterions having a positive charge, namely the donor atoms. This produces a potential barrier at the grain boundaries that resembles a back-to-back Schottky barrier and impedes the motion of carriers when a voltage is applied across the polycrystalline material. In TCO films, which are typically *n*-type, a depletion region is generated on both sides of the grain barrier accompanied by the energetic barrier of height  $\Phi_b$  for the electrons, since the electron trapping characteristics of the defects.

The carrier transport in polycrystalline silicon film was described comprehensively by Seto [31]. He assumed that the  $\delta$ -shaped density of electron trap states in the bandgap, which are completely filled. The schematic band diagram according to Seto's model is shown in Fig. 1-9. The carrier transport across the grain barriers is described by the classical thermionic emission (TE). For very high carrier concentrations in the grains, the depletion width is very narrow,



thus enabling quantum-mechanical tunneling of the barriers by the electrons. The model yields an effective mobility  $\mu_{\text{eff}}$  dominated by thermionic emission across the grain barriers with an energetic height  $\Phi_B$ :

$$\mu_{\text{eff}} = \mu_0 \exp \left( - \frac{\Phi_B}{kT} \right), \quad (2)$$

where  $\Phi_B$  is the energetic barrier height at the grain boundary,  $k$  is the Boltzmann constant, and  $T$  is the sample temperature, respectively. The prefactor  $\mu_0$  in Eq. 2 can be described as the mobility inside the grain given by [31]:

$$\mu_0 = \frac{eL}{\sqrt{2\pi m^* kT}}. \quad (3)$$

Depending on the doping concentration in the grains, two expressions for the barrier height can be derived:

$$\Phi_B = \frac{\pi e^2 L^2 n}{2\varepsilon} \quad \text{for } LN > N_t, \quad (4)$$

$$\Phi_B = \frac{\pi e^2 Q_t^2}{2\varepsilon n} \quad \text{for } LN < N_t, \quad (5)$$

where  $e$  is the elementary charge,  $N$  is the carrier density in the bulk of the grain,  $N_t$  is the charge carrier trap density at the boundary,  $\varepsilon$  is the dielectric constant, and  $L$  is the grain size, respectively. For  $LN > N_t$ , the traps are only partially filled and the crystallites are completely depleted, while for  $LN < N_t$ , only part of the grain is depleted and the traps are filled completely. The maximum barrier height  $\Phi_{B, \text{max}}$

occurs for a doping concentration of  $N(\Phi_{B,\max}) = N/L$ , accompanied by the minimum effective mobility according to Eq. 2.

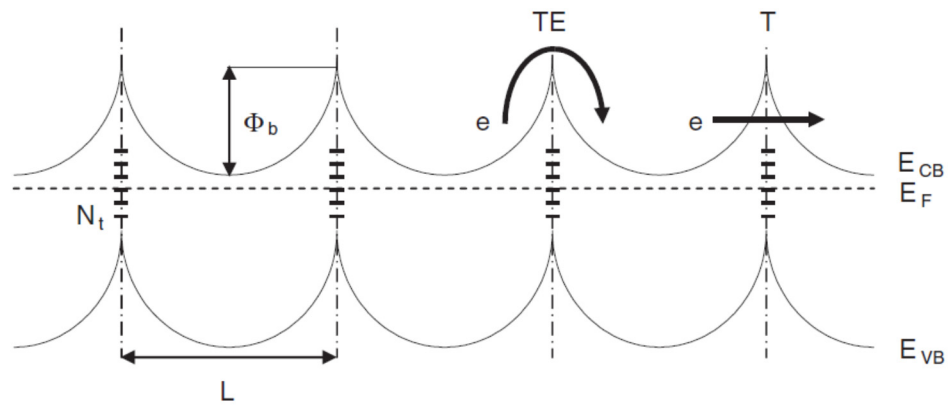


Fig. 1-9. (Color) The Grain size  $L$ , doping  $N$ , and with grain barriers of height  $\Phi_b$  caused by a continuous distribution of electron trap states of density  $N_t$ . Two different transport paths for electrons are indicated as thermionic emission across the barrier TE and tunneling through the barrier  $T$ . From Ref. [13].

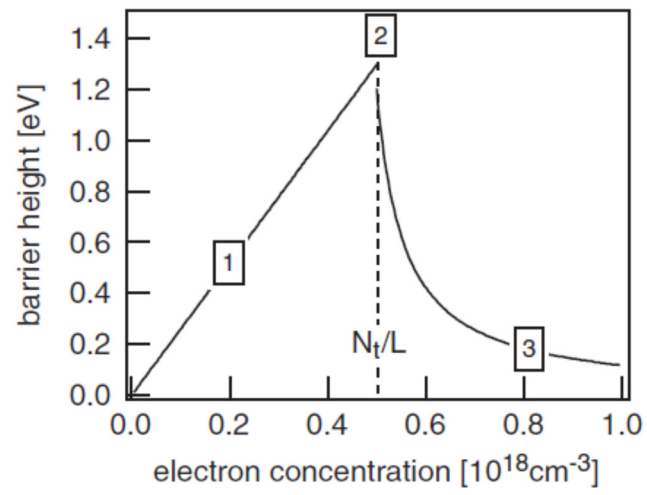


Fig. 1-10. (Color) Barrier height at the grain barriers as a function of the electron concentration in grains (grain size  $L = 100 \text{ nm}$  and trap density  $N_t = 5 \times 10^{12} \text{ cm}^{-2}$ ). From ref. [13].

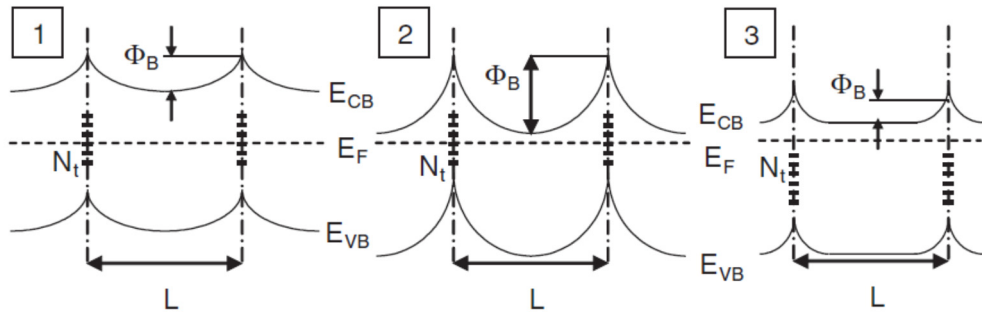


Fig. 1-11. (Color) Schematic band diagrams in the grains for different doping concentration  $N$  in the grain size of  $L$ . The situations (1-3) correspond to carrier concentrations (1-3) in Fig. 1-10. The barrier height increases with increasing  $N$  up to a maximum at  $N_{\max} = N_t/L$  (2). Further increasing  $N$  decreases the barrier height (3). From Ref. [13].

Figure 1-10 displays the barrier height as a function of the carrier concentration for a fixed grain size, calculated from Eq. 4 and 5 with an assumption of a trap density of  $5 \times 10^{12} \text{ cm}^{-2}$  and a grain size of 100 nm. For three situations (1-3) marked in Fig. 1-10, the band structure is schematically shown in Fig. 1-11. In the original models of Seto, only thermionic emission was taken into account. For high carrier concentrations ( $N > 10^{20} \text{ cm}^{-3}$ ) additional tunneling through the barriers takes place, which increases the current flow between the grains. If the original thermionic model is applied for such high carrier concentration lowering the barrier heights are calculated as expected from Eq. 4. Concerning the prefactor  $\mu_0$ , which is viewed as the intragrain mobility, in many cases too low values are extracted from the experiments [32]. Additional carrier scattering processes take place in the grains, for example point defect and dislocation scattering. In the Seto model, it is assumed that every grain barrier exhibits the same barrier height, an idealization of a real polycrystalline film.

### 1.2.5. Optical Characteristic of ZnO

ZnO has a high transparency in the visible region due to the bandgap of 3.2-3.4 eV. When light passes through ZnO materials, if the photon energy is smaller than the optical-bandgap energy  $E_g^{op}$ , the photon will through the material without any absorption. If the photon energy is higher than  $E_g^{op}$ , then absorption is occurred when electrons in the valence band absorb energy from incoming photons and excited to higher energy state in the conduction band. Hence, optical-bandgap energy of ZnO materials can be deduced from optical absorption spectra. When light with a continuous spectral in visible range passes through a ZnO film at normal incident angle, its behavior follows this equation assuming that reflection loss occurs only at the front surface.

$$I = I_o (1-R) e^{-\alpha x}. \quad (6)$$

where  $I$  and  $I_o$  are the intensities of transmitted and incident light respectively,  $\alpha$  is absorption coefficient of the ZnO,  $R$  is the reflectance, and  $x$  is the length of the light path inside the film. The absorbance of the ZnO film can be measured by UV/Visible spectrometer. From absorbance, the absorption coefficient can be obtained following equation:

$$\text{absorbance} = -\log (I / I_o). \quad (7)$$

Absorption coefficient near the onset of absorption edge is related to optical-bandgap energy described as Tauc's relation [33]:

$$\alpha^2 \propto (h\nu - E_g^{op}). \quad (8)$$

Therefore, from plots of the  $\alpha^2$  vs.  $h\nu$ , the optical-bandgap energy ( $E_g^{op}$ ) can be estimated. Their fundamental absorption edge lies in the UV range and will shift to higher energies with the increase of carrier concentration, which can be caused by filling of the states near the bottom of the conduction band, and this phenomenon is called the Burstein-Moss (BM) effect [34,35]. However, the carrier dependence of the measured bandgap shift is generally much less than that expected from the band-filling model (BM effect). To account for this discrepancy, a bandgap renormalization model was proposed, where the bandgap narrowing is considered as a result of the modification of electronic states because of the mutual exchange and Coulomb interactions between the added free electrons in the conduction band and their scattering against ionized impurity [36,37]. In more detail, there are four major contributions to the bandgap narrowing: (1) shift  $\Delta E_{x(maj)}$  of the bandedge due to exchange interaction (majority carriers); (2) shift  $\Delta E_{cor(mino)}$  of the bandedge due to carrier-carrier or electron-hole interaction (minority carriers), also designated as the correlation energy; (3) shift  $\Delta E_{i(maj)}$  of the bandedge due to carrier-impurity interactions (majority carriers); and (4) shift  $\Delta E_{i(mino)}$  of the bandedge due to carrier-impurity interactions (minority carriers) [38]. The shifts  $\Delta E_{x(maj)}$  and  $\Delta E_{cor(mino)}$  are also known as shifts due to many-body interactions, or simply many-



body effect. All shifts are into the bandgap and the total bandgap narrowing  $\Delta E_g$  is obtained by adding all the shifts,

$$\Delta E_g = \Delta E_{x(\text{maj})} + \Delta E_{\text{cor}(\text{mino})} \Delta E_{i(\text{maj})} + \Delta E_{i(\text{mino})}. \quad (8)$$

Based on Jain's analysis, the bandgap narrowing model may be quantitatively expressed in the form of [38]:

$$\frac{\Delta E_g}{R} = 1.83 \frac{\Lambda}{N_b^{1/3}} \frac{1}{r_s} + \frac{0.95}{r_s^{3/4}} + \left[ 1 + \frac{R_{(\text{mino})}}{R} \right] \frac{1.57}{N_b r_s^{3/2}}, \quad (8)$$

where  $R$  is the effective Rydberg energy for a carrier bound to a dopant atom,  $\Lambda$  is the correction factor that accounts for anisotropy of the bands in  $n$ -type semiconductors and interaction between the heavy- and light-hole bands in  $p$ -type semiconductors, and  $N_b$  is the number of equivalent band extrema.  $r_s$  is the average distance between majority carriers, normalized to the effective Bohr radius  $(3/4\pi)^{1/3} n_e^{-1/3} / a^*$ . This modification leads to an increase in the energy of the valence band maximum and decrease in the energy of the conduction-band minimum. The net change in optical bandgap can therefore be taken as a difference of the two contributions, band filling and bandgap renormalization. The details of the derivation of these shifts can be found in Ref. 6. Figure 1-12 shows the BM effect and bandgap renormalization schematically in the Al-doped ZnO films.

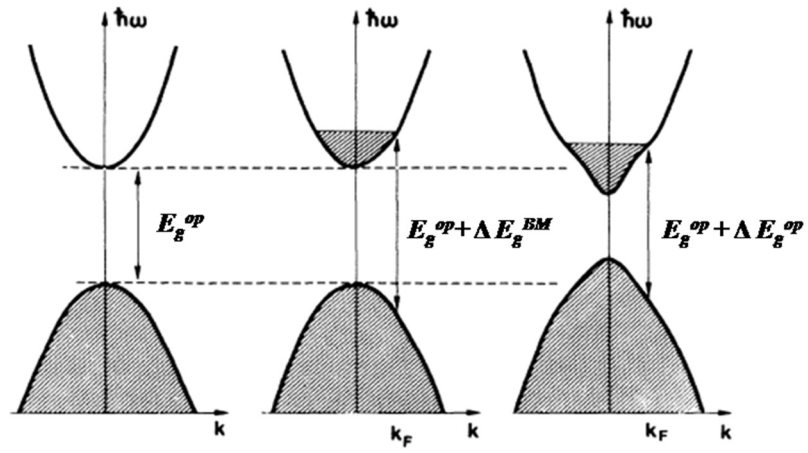


Fig. 1-12. (Color) Schematic band structure with parabolic conduction and valance bands separated by optical bandgap  $E_g^{op}$  (a), after Al doping assumed to have the sole effect of filling the lowest states in the conduction band, so that the  $E_g^{op}$  is widened by a BM effect (b), represents the bandgap renormalization in the case of many-body interaction (c). From Ref. [36].

### 1.2.6. ZnO-based TCO in Thin Film Silicon Solar Cells

As mentioned briefly in chapter 1.1.4, transparent conducting oxide (TCO) films are important components of thin-film silicon solar cells. Such highly conducting and transparent TCO layers are commonly used as contact layers of *p-i-n* solar cell structures [39,40]. Since the lateral conductance of doped silicon layers is insufficient to prevent resistive losses, the TCO contact layer is used to avoid a high series resistance [39]. Moreover, front contact TCO layers serve the purposes of an effective coupling of light into the solar cell by refractive index matching and, an efficient light trapping by scattering of light into the cell at rough TCO/silicon interface. For the choice of proper TCO layer, several criteria are of importance:

- (i) High optical transparency in the solar spectrum range.
- (ii) High electrical conductivity (high carrier mobility).
- (iii) Grown or patterned thin films with surface texture for light scattering.
- (iv) Non toxicity and sustainability.
- (v) Low material cost.
- (vi) High chemical stability of the bulk and of the contact to silicon.
- (vii) Long-term stability.

To date, the most common TCO used in such applications is Sn-doped  $\text{In}_2\text{O}_3$  (ITO), where carrier densities exceeding  $10^{21} \text{ cm}^{-3}$  and resistivities below  $10^{-4} \Omega\cdot\text{cm}$  have been achieved [41]. However, indium is a relatively expensive, which is desired not only for TCOs, but also, for example, as an active component in the rapidly expanding range of InGaN-based optoelectronic and photovoltaic devices [42,43]. Therefore, much recent research has been focused on alternative materials. These include the pure and impurity-doped binary materials ZnO,  $\text{SnO}_2$ , and  $\text{Ga}_2\text{O}_3$ , and also multi-component oxides such as indium-gallium-zinc-oxide and cubic spinel compounds such as  $\text{CdIn}_2\text{O}_4$  and  $\text{SnZn}_2\text{O}_4$ . Especially, ZnO-based TCOs have recently received intense interests due to their low cost, abundance, and non-toxicity. Furthermore, excellent light-scattering properties can be achieved via sputter deposition and surface texturing by wet-chemical etching, particularly for front TCOs in silicon thin-film solar cells, which suggest a great potential toward effective light trapping for enhancing power-conversion efficiencies [44]. It also should be noted that the obtained minimum resistivities of impurity-doped ZnO films is still decreasing, whereas those of impurity-doped  $\text{SnO}_2$  and  $\text{In}_2\text{O}_3$  films have essentially remained unchanged for more than the past years (Fig. 1-13) [12].

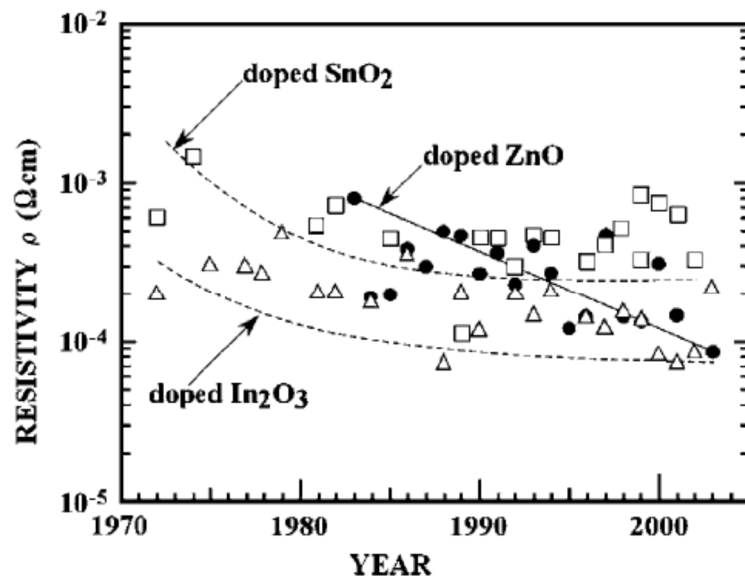


Fig. 1-13. (Color) Reported resistivity ( $\rho$ ) of impurity-doped binary compound TCO films, 1972–2005: impurity-doped  $\text{SnO}_2$  ( $\square$ ),  $\text{In}_2\text{O}_3$  ( $\Delta$ ) and  $\text{ZnO}$  ( $\bullet$ ). From Ref. [12].

### 1.3. Motivation and Objectives

In terms of electrical stability, aluminium doped ZnO thin films have a critical problem in that the resistivity increases with exposure to harsh environment (e.g., damp heat test, relative humidity of 85% and temperature of 85°C), as shown in Fig. 14 [45]. Other ZnO-based TCO films such as ZnO:In, ZnO:Ga, and ZnO:B showed similar electrical degradations [46,47]. This instability eventually affects the reliability of the solar cell using a ZnO-based transparent electrodes. After damp-heat exposure, the solar cell deposited with the ZnO based TCO layer as electrodes shows strongly degraded electrical characteristics due to an increase of the serial resistance of the cell (Fig. 15) [47].

Ballif's study provides insight into the basic aspects of interpretation of degradation mechanism [48]. By combining analyses of the electrical and optical properties of the films, they were able to attribute the degradation to an increase of electron grain boundary scattering (Fig. 16). In this reason, the thick ZnO:Al films (> 800 nm) with a relatively large grain size could form a compact structure, and they showed a smaller increase in resistivity compared to that of the very thin ZnO:Al films (< 300 nm) with small grain size [49].

However, the environmental stability is still an unsolved problem, which prevents the ZnO-based TCOs from actual applications in devices requiring long-term stability [50]. For this reason, great efforts have been dedicated to

understand environmental reliability, though previous research has mainly focused on methodological and technical aspects. Thus, very little is known about the essential degradation mechanisms. The aim of this thesis is to better understand the underlined mechanisms on TCO degradation in harsh environments.

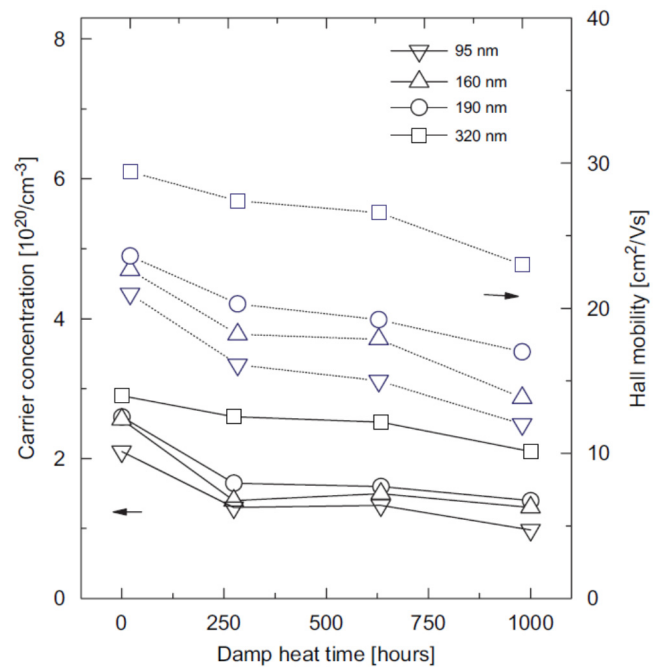


Fig. 1-14. (Color) Degradation of carrier concentration and Hall mobility of ZnO:Al (four different thicknesses) after damp-heat (humid and hot atmosphere) treatment. From Ref. [45].



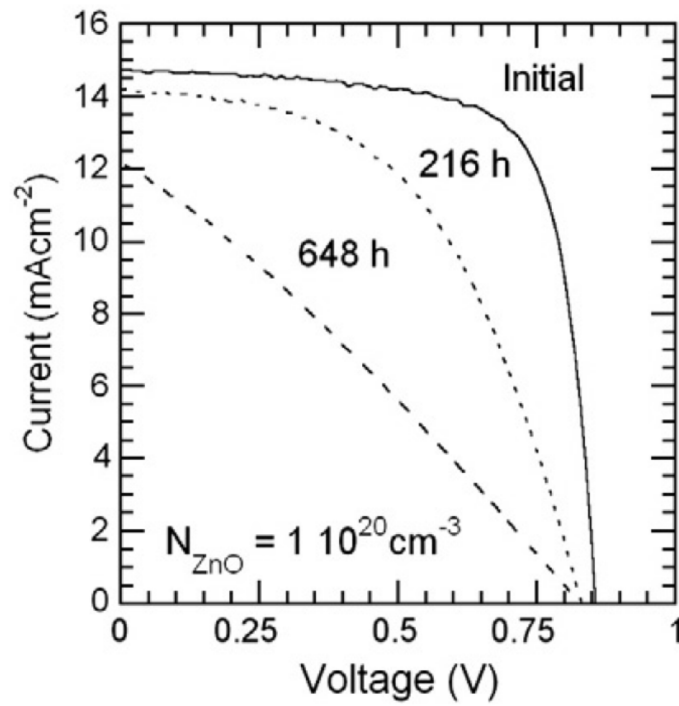


Fig. 1-15. (Color) Current-voltage characteristics of an unencapsulated a-Si:H solar cell fabricated with LPCVD ZnO:B electrodes for various damp heat exposure (80°C, 100% humidity) times. From Ref. [48].

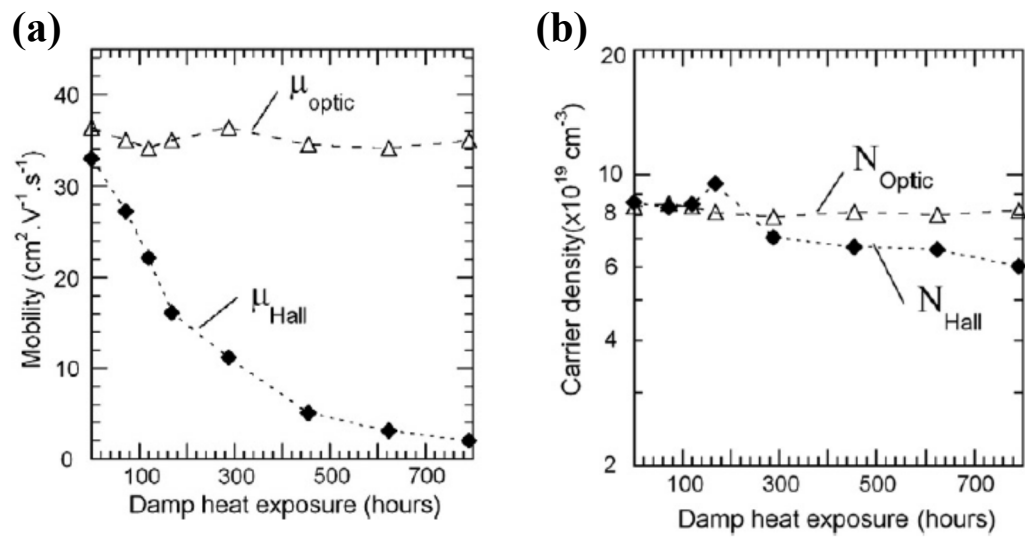


Fig. 1-16. (Color) Optical and Hall mobility and (b) optical and Hall carrier density of the 2  $\mu\text{m}$  thick LPCVD ZnO:B film as a function of the damp heat exposure (40 °C, 100% humidity) time. From Ref. [48].

## 1.4. References

1. J. Nelson, "The Physics of Solar Cells," *Imperial College Press* UK (2003).
2. B. M. van der Ende, L. Arts, and A. Meijerink, "Lanthanide Ions as Spectral Converters for Solar Cells," *Phys. Chem. Chem. Phys.* **11**, 11081 (2009).
3. Y. Kuang, M. D. Vece, J. K. Rath, L. van Dijk, and R. E. I. Schropp, "Elongated Nanostructures for Radial Junction Solar Cells," *Rep. Prog. Phys.* **76**, 106502 (2013).
4. National Center for Photovoltaics, Nat. Renewable Energy Lab., Golden, CO, USA. Chart of best research-cell efficiencies. (2014). [Online]. Available: <http://www.nrel.gov/ncpv>.
5. A. V. Shah, H. Schade, M. Vanecek, J. Meier, E. Vallat-Sauvain, N. Wytsch, U. Kroll, C. Droz, and J. Bailat, "Thin-Film Silicon Solar Cell Technology," *Prog. Photovoltaics*, **12**, 113 (2004).
6. J. Hüpkes, B. Rech, S. Calnan, O. Kluth, U. Zastrow, H. Siekmann, M. Wuttig, "Material Study on Reactively Sputtered Zinc Oxide for Thin Film Silicon Solar Cells," *Thin Solid Films*, **502**, 286 (2006).
7. M. Berginski, J. Hüpkes, M. Schulte, G. Schöpe, H. Stiebig, B. Rech, "The Effect of Front ZnO:Al Surface Texture and Optical Transparency on Efficient Light Trapping in Silicon Thin-Film Solar Cells," *J. Appl. Phys.* **101**, 074903-1 (2002).
8. A. Porch, D. V. Morgan, R. M. Perks, M. O. Jones, and P. P. Edwards, "Transparent Current Spreading Layers for Optoelectronic Devices," *J. Appl. Phys.* **96**, 4211 (2004).

9. A. N. Tiwari, G. Khrypunov, F. Kurdzesau, D. L. Bätzner, A. Romeo, and H. Zogg, “CdTe Solar Cell in a Novel Configuration,” *Prog. Photovoltaics* **12**, 33 (2004).
10. G. S. Chae, “A Modified Transparent Conducting Oxide for Flat Panel Displays Only,” *Japan. J. Appl. Phys.* **40** 1282 (2001).
11. I. Hamberg and C. G. Granqvist, “Evaporated Sn-doped In<sub>2</sub>O<sub>3</sub> Films: Basic Optical Properties and Applications to Energy-Efficient Windows,” *J. Appl. Phys.* **60**, R123 (1986).
12. T. Minami, “Transparent Conducting Oxide Semiconductors for Transparent Electrodes,” *Semicond. Sci. Technol.* **20**, S35 (2005).
13. K. Ellmer, A. Klein, and B. Rech, “Transparent Conductive Zinc Oxide: Basics and Applications in Thin Film Solar Cells,” *Springer* (2008).
14. Ü. Özgür, Ya. I. Alivov, C. Liu, A. Teke, M. A. Reshchikov, S. Doğan, V. Avrutin, S.-J. Cho, and H. Morkoç, “A Comprehensive Review of ZnO Materials and Devices,” *J. Appl. Phys.* **98**, 041301 (2005).
15. D. C. Look, J. W. Hemsky, and J. R. Sizelove, “Residual Native Shallow Donor in ZnO,” *Phys. Rev. B* **82**, 2552-2555 (1999).
16. L. Schmidt-Mende and J. L. MacManus-Driscoll, “ZnO-Nanostructures, Defects, and Devices,” *Mater. Today* **10**, 40-48 (2007).
17. K. Ellmer, “Past Achievements and Future Challenges in the Development of Optically Transparent Electrodes,” *Nat. Photonics* **6**, 809 (2012).
18. P. D. C. King and T. D. Veal, “Conductivity in Transparent Oxide Semiconductors,” *J. Phys.: Condens. Matter* **23**, 334214 (2011).

19. A. Bourlange, D. J. Payne, R. G. Egddell, J. S. Foord, P. P. Edwards, M. O. Jones, A. Schertel, P. J. Dobson, and J. L. Hutchison, "Growth of  $\text{In}_2\text{O}_3(100)$  on Y-Stabilized  $\text{ZrO}_2(100)$  by O-Plasma Assisted Molecular Beam Epitaxy," *Appl. Phys. Lett.* **92**, 092117 (2008).
20. M. E. White, M. Y. Tsai, F. Wu, and J. S. Speck, "Plasma-Assisted Molecular Beam Epitaxy and Characterization of (101) On -Plane Sapphire," *J. Vac. Sci. Technol. A* **26**, 1300 (2008).
21. H. L. Hartnagel, A. L. Dawar, A. K. Jain, and C. Jagadish, "Semiconducting Transparent Thin Films," *Institute of Physics Publishing* Bristol (1995).
22. T. Minami, "New *n*-Type Transparent Conducting Oxides," *MRS Bull.* **25**, 38 (2000).
23. K. ellmer, "Resistivity of Polycrystalline Zinc Oxide Films: Current Status and Physical Limit," *J. Phys. D: Appl. Phys.* **34**, 3097 (2001).
24. I. Sieber, N. Wanderka, I. Urban, I. Dörfel, E. Schierhorn, F. Fenske, and W. Fuhs, "Electron Microscopic Characterization of Reactively Sputtered ZnO Films with Different Al-Doping Levels," *Thin Solid Films* **330**, 108 (1998).
25. B. Pödör, "Electron Mobility in plastically Deformed Germanium," *Phys. Stat. Sol.* **16**, K167 (1966).
26. D. C. Look and J. R. Sizelove, "Dislocation Scattering in GaN," *Phys. Rev. Lett.* **82**, 1237 (1999).
27. D. Gerthsen, D. Litvinov, T. Gruber, C. Kirchner, and A. Waag, "Origin and Consequences of a High Stacking Fault Density in Epitaxial ZnO Layers," *Appl. Phys. Lett.* **81**, 3972 (2002).

28. P. Erhart and K. Albe, "First-Principles Study of Intrinsic Point Defects in ZnO: Role of Band Structure, Volume Relaxation, and Finite-Size Effects," *Phys. Rev. B* **73**, 115207 (2006).
29. C. Coskun, D. C. Look, G. C. Farlow, and J. R. Sizelove, "Radiation Hardness of ZnO at Low Temperature," *Semicond. Sci. Technol.* **19**, 752 (2004).
30. V. Srikant, V. Sergo, and D. R. Clarke, "Epitaxial Aluminum-Doped ZnO Oxide Thin Films on Sapphire: II, Defect Equilibria and Electrical Properties," *J. Am. Ceram. Soc.* **78**, 1935 (1995).
31. J. Y. Seto, "The Electrical Properties of Polycrystalline Silicon Films," *J. Appl. Phys.* **46**, 5247 (1975).
32. G. Baccarani, B. Ricco, and G. Spadini, "Transport Properties of Polycrystalline Silicon Films," *J. Appl. Phys.* **49**, 5565 (1978).
33. Y. Kim, W. Lee, D.-R. Jung, J. Kim, S. Nam, H. Kim, and B. Park, "Optical and Electronic Properties of Post-Annealed ZnO:Al Thin Films," *Appl. Phys. Lett.* **96**, 171902-1 (2010).
34. E. Burstein, "Anomalous Absorption Limit in InSb," *Physics Review* **93**, 632 (1954).
35. T. S. Moss, "The Interpretation of the Properties of Indium Antimonide," *Proceedings of the Physical Society. Section B* **67**, 775 (1954).
36. B. E. Sernelius, K.-F. Berggren, Z.-C. Jin, I. Hamberg, and C. G. Granqvist, "Band-Gap Tailoring of ZnO by means of Heavy Al Doping," *Phys. Rev. B* **37**, 10244 (1988).

37. S. C. Jain, J. M. McGregor, and Roulston, "Band-Gap Narrowing in Novel III-V Semiconductors," *J. Appl. Phys.* **68**, 3747 (1990).
38. S. C. Jain and D. J. Roulston, "A Simple Expression for Band Gap Narrowing (BGN) In Heavily Doped Si, Ge, GaAs and  $\text{Ge}_x\text{Si}_{1-x}$  Strained Layers," *Solid-State Electron.* **34**, 453 (1991).
39. D. E. Carlson and C. R. Wronski, "Amorphous Silicon, Topics in Applied Physics," *Springer*, Berlin (1979).
40. J. Müller, B. Rech, J. Springer, and M. Vanecek, "TCO and Light Trapping in Silicon Thin Film Solar Cells," *Sol. Energ. Mat. Sol. C.* **48**, 351 (1997).
41. C. G. Granqvist and A. Hultåker, "Transparent and Conducting ITO Films: New Developments and Applications," *Thin Solid Films* **411**, 1 (2002).
42. F. A. Ponce and D. P. Bour, "Nitride-Based Semiconductors for Blue and Green Light-Emitting Devices," *Nature* **386**, 351 (1997).
43. J. Wu, W. Walukiewicz, K. M. Yu, W. Shan, J. W. Ager III, E. E. Haller, H. Lu, W. J. Schaff, W. K. Metzger, and S. Kurtz, "Superior Radiation Resistance of  $\text{In}_{1-x}\text{Ga}_x\text{N}$  Alloys: Full-Solar-Spectrum Photovoltaic Material System," *J. Appl. Phys.* **94**, 6477 (2003).
44. M. Berginski, J. Hüpkes, M. Schulte, G. Schöpe, H. Stiebig, and B. Rech, "The Effect of Front  $\text{ZnO:Al}$  Surface Texture and Optical Transparency on Efficient Light Trapping in Silicon Thin-Film Solar Cells," *J. Appl. Phys.* **101**, 074903 (2002).

45. W. Lin, R. Ma, J. Xue, and B. Kang, "RF Magnetron Sputtered ZnO:Al Thin Films on Glass Substrates: A Study of Damp Heat Stability on their Optical and Electrical Properties," *Solar Energ. Mater. Solar C.* **91**, 1902 (2007).
46. P. Nunes, E. Fortunato, and R. Martins, "Influence of the Post-Treatment on the Properties of ZnO Thin Films," *Thin Solid Films* **383**, 277 (2001).
47. B. D. Ahn, J. H. Kim, H. S. Kang, C. H. Lee, S. H. Oh, K. W. Kim, G.-E. Jang, and S. Y. Lee, "Thermally Stable, Highly Conductive, and Transparent Ga-Doped ZnO Thin Films," *Thin Solid Films* **516**, 1382 (2008).
48. J. Steinhauser, S. Meyer, M. Schwab, S. Fay, C. Ballif, U. Kroll, D. Borrello, "Humid Environment Stability of Low Pressure Chemical Vapor Deposited Boron Doped Zinc Oxide used as Transparent Electrodes in Thin Film Silicon Solar Cells," *Thin Solid Films* **520**, 558 (2011).
49. T. Tohsophon, J. Hupkes, S. Calnan, W. Reetz, B. Rech, W. Beyer, and N. Sirikulrat, "Damp Heat Stability and Annealing Behavior of Aluminum Doped Zinc Oxide Films Prepared by Magnetron Sputtering," *Thin Solid Films*, **673**, 511 (2006).
50. J. Y. Huang, L. Zhong, C. M. Wang, J. P. Sullivan, W. Xu, L. Q. Zhang, S. X. Mao, N. S. Hudak, X. H. Liu, A. Subramanian, H. Y. Fan, L. A. Qi, A. Kushima, and J. Li, "In Situ Observation of the Electrochemical Lithiation of a Single SnO<sub>2</sub> Nanowire Electrode," *Science* **330**, 1515 (2010).



## Chapter 2.

### **\*Quantitative Analyses of Damp-Heat-Induced Degradation in Transparent Conducting Oxides**

#### **2.1. Introduction**

Transparent conducting oxides (TCOs) have been widely used for various applications requiring their optoelectronic multi-functionalities, such as photovoltaic devices, liquid crystal displays (LCD), organic light-emitting diodes (OLED), touch panels, etc. [1-9]. Among various TCOs, ZnO-based TCOs have recently received intense interests to replace commercially used indium tin oxide (ITO) or fluorine-doped tin oxide (FTO) due to their low cost, abundance, and non-toxicity. Furthermore, excellent light-scattering properties can be achieved via sputter deposition and surface texturing by wet-chemical etching, particularly for front TCOs in silicon thin-film solar cells, which suggest a great potential toward effective light trapping for enhancing power-conversion efficiencies [10].

However, the environmental stability is still an unsolved problem especially when exposed to harsh environment, which prevents the ZnO-based TCOs from

---

\*The work presented in Chapter 2 was published in *Sol. Energy Mater. Sol. Cells* **122**, 282 (2014) entitled, “Quantitative Analyses of Damp-Heat-Induced Degradation in Transparent Conducting Oxides,”  
**Jae Ik Kim**, Woojin Lee, Taehyun Hwang, Jongmin Kim, Seung-Yoon Lee, Suji Kang, Hongsik Choi, Saeromi Hong, Helen Hejin Park, Taeho Moon,\* and Byungwoo Park.\*

actual applications in devices requiring long-term stability [11-16]. For this reason, great efforts have been dedicated to understand environmental reliability, though previous research has mainly focused on methodological and technical aspects. Thus, very little is known about the essential degradation mechanisms.

In this work, quantitative investigation on degradation behavior in a controlled damp-heat (DH) environment (humid and hot atmosphere) is introduced for aluminum-doped ZnO (ZnO:Al) thin films. The electrical degradation behavior was thoroughly analyzed in aspects of both energy-level shifts in band diagrams and changes in carrier-transport characteristics of the intragrain and grain boundary separately. Also, the correlation between the degradation behavior and nanostructural change was resolved.

## **2.2. Experimental Section**

ZnO:Al thin films (thickness of 1.5  $\mu\text{m}$ ) were deposited on Corning Eagle XG glasses by rf magnetron sputtering using the ZnO:Al targets doped with 1.6 wt. %  $\text{Al}_2\text{O}_3$ . The sputtering was performed under an Ar atmosphere at 400°C, with an rf power of 75 W and an operating pressure of 5 mTorr. For comparison, ZnO thin films were prepared without any doping. After deposition, the ZnO:Al films were exposed to a damp-heat atmosphere of a relative humidity of 85% and a temperature of 85°C, for up to 800 h.

The Hall resistivity of thin films was measured by four-point probe, and the carrier concentration was estimated from the Hall measurement (HL5500PC: BIO-RAD) using a van der Pauw method at 300 K. The Hall-carrier mobility was deduced from the relation  $\rho = 1/ne\mu$ , where  $\rho$ ,  $n$ ,  $e$ , and  $\mu$  are the resistivity, carrier concentration, electron charge, and carrier mobility, respectively. Transport characteristics were investigated from the temperature dependence on electrical properties in the range of 80 to 340 K.

The crystallinity of the ZnO:Al films were analyzed by x-ray diffraction (XRD, New D8 Advance: Bruker). The change in conduction-band filling was investigated with the optical bandgap ( $E_g^{op}$ ) estimated from the UV/Vis absorption spectra (Lambda 35: Perkin-Elmer). The infrared reflectance was investigated to separately analyze the electrical characteristics of the intragrain and grain boundary by Fourier-transform infrared spectrometer (FT-IR, IFS 66v/S: Bruker). The chemical state and Fermi-level shift of the ZnO:Al films were analyzed by x-ray photoelectron spectroscopy (XPS, AXIS-HSI: KRATOS).

## 2.3. Results and Discussion

Figure 2-1 shows the changes in electrical properties of the ZnO:Al thin films as a function of DH exposure. The continuous degradation behavior of the Hall resistivity was observed from initially  $\sim 6.7 \times 10^{-4}$  to  $\sim 1.9 \times 10^{-3} \Omega \text{ cm}$  after 800

h. Note that the degradation is related to the decrease of both carrier mobility and carrier concentration with the DH exposure.

To characterize the carrier-concentration degradation, the optical bandgap was estimated by Tauc's relation [5]:

$$\alpha^2 \propto (h\nu - E_g^{op}), \quad (1)$$

where  $\alpha$  is the absorption coefficient,  $h\nu$  is the photon energy, and  $E_g^{op}$  is the optical bandgap (Fig. 2-2). The  $E_g^{op}$  values are reduced from initially 3.73 eV to 3.60 eV after 800-h DH exposure. To compare the band structure and illustrate the effect of conduction-band filling, the  $E_g^{op}$  from the nondegenerate ZnO sample was also acquired to be 3.26 eV. The conduction-band filling was quantitatively estimated to be  $\sim 0.59$  eV and  $\sim 0.43$  eV for 0-h and 800-h DH exposure, respectively, from the Burstein-Moss model [17,18]:

$$E_F - E_{CB} = \left( \frac{\hbar^2}{2m_e^*} \right) (3\pi^2 n)^{2/3}, \quad (2)$$

where  $E_F$ ,  $E_{CB}$ ,  $n$ , and  $m_e^*$  are, respectively, the Fermi level, conduction-band minimum, carrier concentration, and effective electron mass ( $\cong 0.28 m_e$  where  $m_e$  is the electron rest mass [19]).

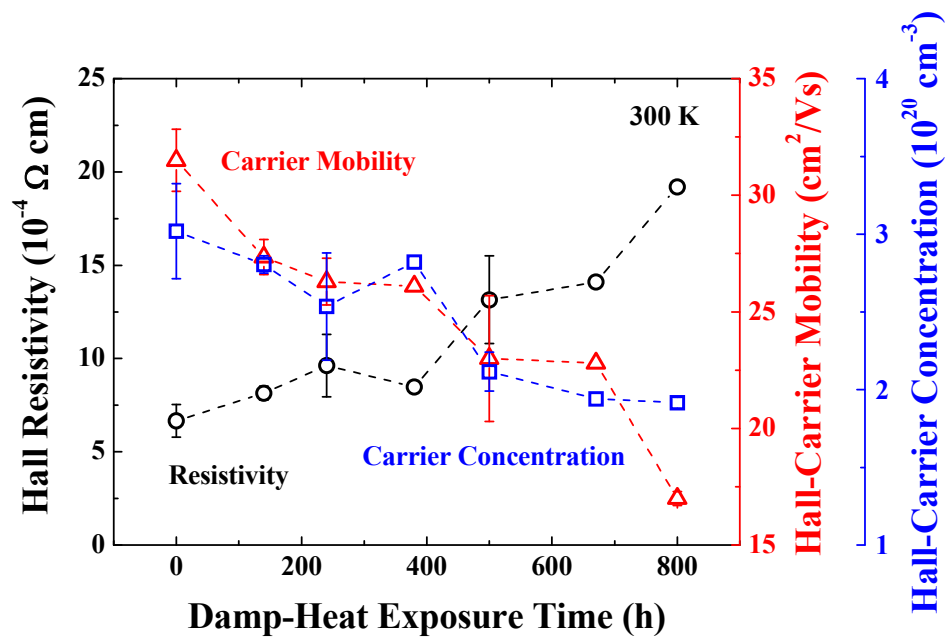


Fig. 2-1. (Color) Hall resistivity, carrier mobility, and carrier concentration of ZnO:Al films as a function of damp-heat (DH) exposure time.

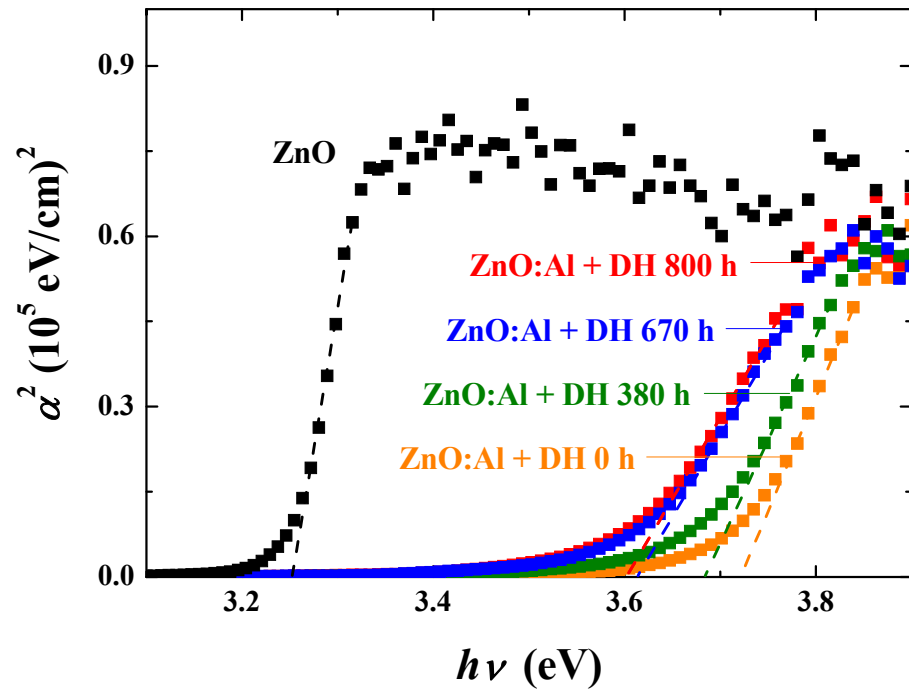


Fig. 2-2. (Color) Plot of  $\alpha^2$  vs.  $h\nu$  near the bandedge for ZnO:Al films at various DH exposure times. For comparison, the absorption from nondegenerate ZnO is also included.

To correlate the energy-level shifts of  $E_g^{op}$  and the carrier-concentration degradation, the XPS core-level spectra of Zn 2p were analyzed as shown in Fig. 2-3. For the pristine ZnO:Al compared to ZnO, the upshift of the Fermi level by  $\sim 0.6$  eV is shown due to the electron population within the conduction band. After the DH treatment of 800 h, the Fermi energy is decreased by  $\sim 0.1$  eV, which is well correlated with the  $E_g^{op}$  analyses and conduction-band filling deduced from Eq. (2).

The O 1s peaks of the ZnO:Al films were also analyzed to identify the chemisorbed hydroxyl groups in humid atmosphere, as shown in Fig. 2-4. With two XPS peaks at  $\sim 530.9$  eV ( $O^{2-}$  binding with Zn or substitutional Al) and  $\sim 532.5$  eV ( $OH^-$  in metal-OH bonds [20,21]), the integrated-intensity ratio of  $OH^-/O^{2-}$  was  $\sim 23\%$  for the initial ZnO:Al film, while the ratio significantly increases to  $\sim 44\%$  after the DH exposure of 800 h. This result clearly indicates the increase of chemisorbed  $OH^-$  with the exposure to the humid environment, probably along the grain boundaries which are easy diffusion paths for the  $OH^-$  species [22]. The full-width at half maximum (FWHM) of the XRD patterns was unchanged as shown in Fig. 2-5. This result supports that the crystallinity of the ZnO:Al thin films are hardly affected by the DH environment, and the degradation centers are located mainly along the grain boundaries due to the hydroxyl groups [23].

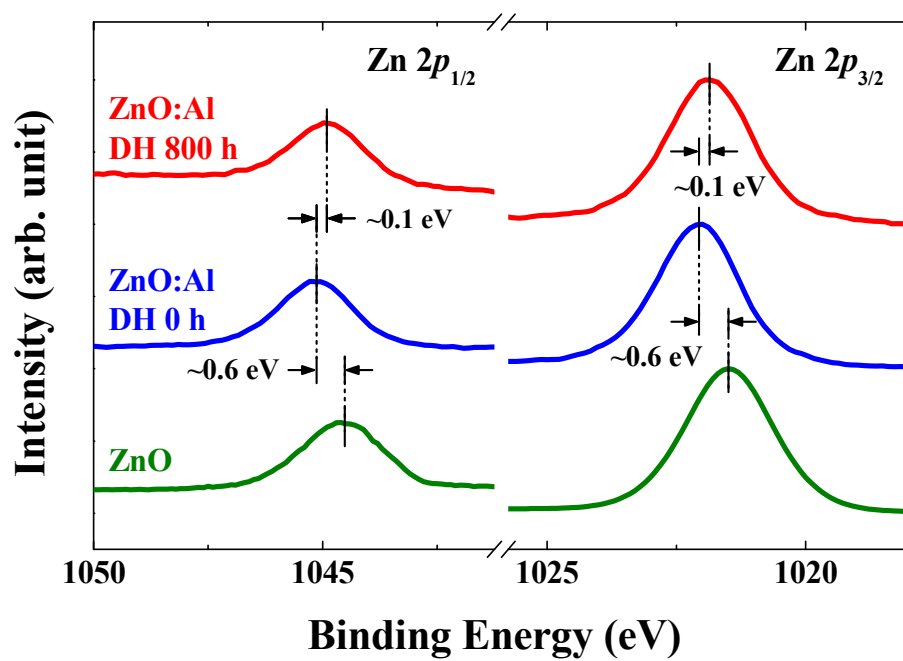


Fig. 2-3. (Color) Comparison of the XPS core-level spectra (Zn 2p peak) of the ZnO and ZnO:Al films with and without DH exposure.



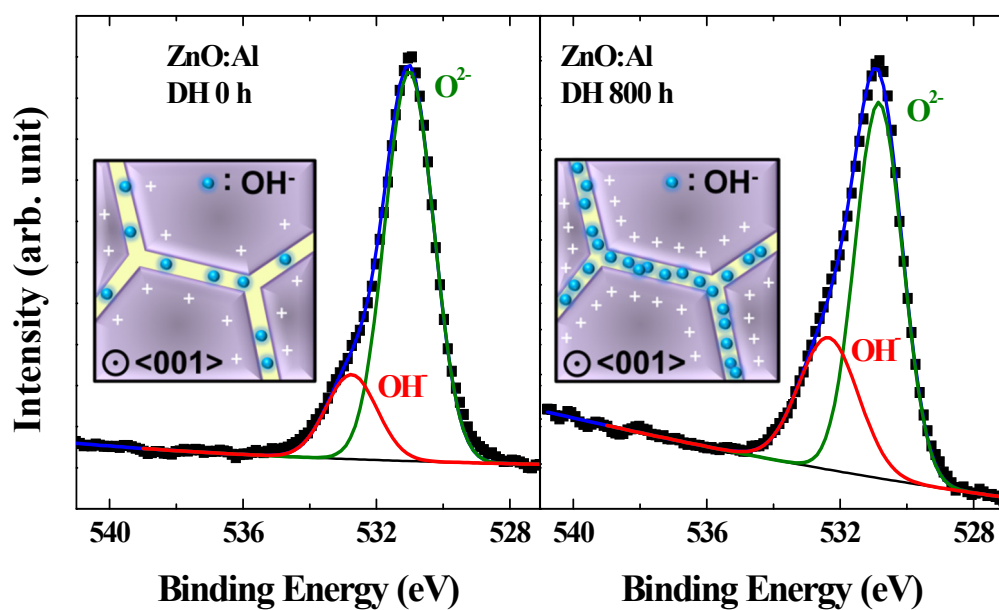


Fig. 2-4. (Color) Comparison of the XPS core-level spectra of the ZnO and ZnO:Al films with and without DH exposure. Deconvoluted O 1s peak of the films. Each inset shows a scheme of the chemisorbed hydroxyl groups along the grain boundaries and accumulated positive carriers towards the depleted regions at the given DH exposure condition.

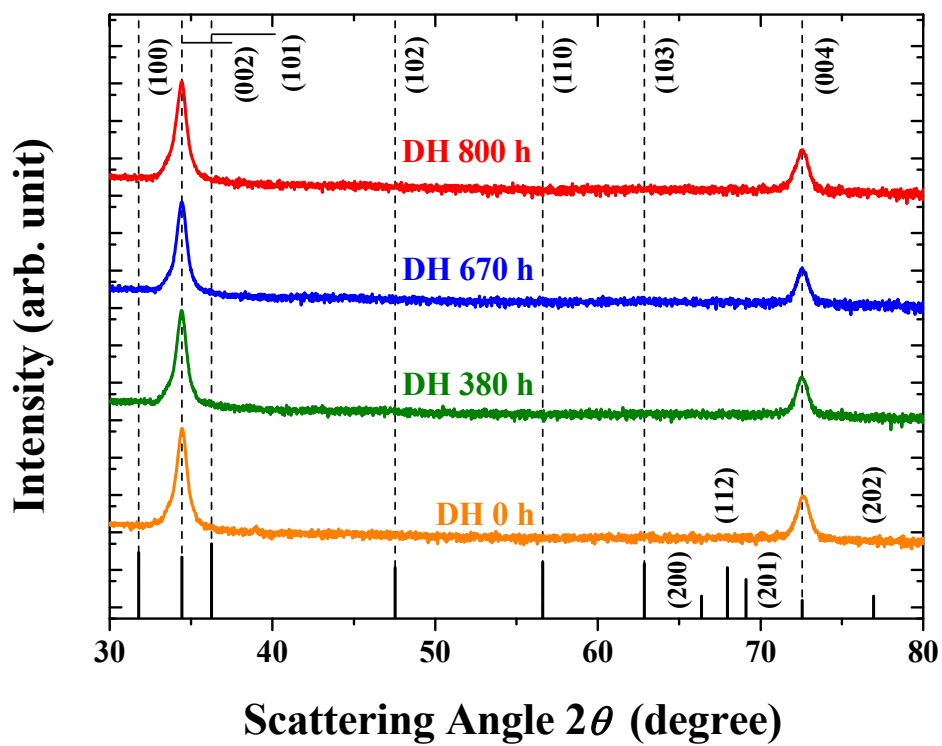


Fig. 2-5. (Color) X-ray diffraction of ZnO:Al films at various DH exposure times.

The peak intensities and positions from the hexagonal ZnO (JCPDS #36-1451) are shown as solid bars.

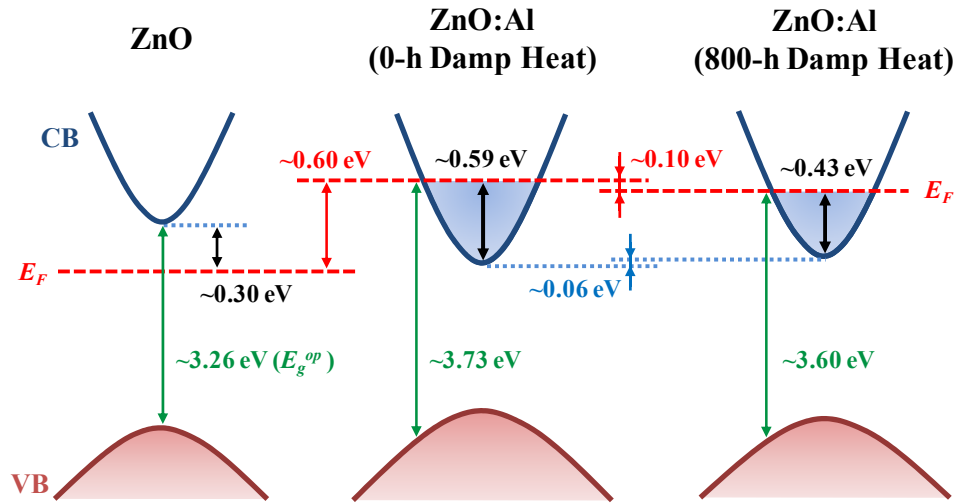


Fig. 2-6. (Color) Schematic band diagrams for the ZnO and ZnO:Al films (with and without DH exposure). The Fermi-level shift (from the XPS spectra of Fig. 2-3), band-filling change (from the carrier concentration (Fig. 2-1) and Eq. (2)), and the optical bandgap  $E_g^{op}$  (from Fig. 2-2) are summarized with a schematic bandgap renormalization. The Fermi level for the nondegenerate ZnO was assumed to be  $\sim 0.3$  eV below the conduction-band minimum [25].

Based on the observations such as the Fermi-level shift ( $\sim 0.10$  eV from Fig. 2-3), optical-bandgap energy ( $\sim 3.73$  to  $\sim 3.60$  eV from Fig. 2-2), and change in conduction-band filling ( $\sim 0.59$  to  $\sim 0.43$  eV from Fig. 2-1 and Eq. (2)), the energy-level shifts caused by the DH exposure are quantitatively described in band diagrams (Fig. 2-6). It shows that the bandgap-renormalization contribution from the conduction and valence bands appears to be  $\sim 0.06$  eV, which matches well with value from the bandgap-renormalization model ( $\sim 0.05$  eV) [24]. As a reference, the band structure for the undoped ZnO was included to illustrate the change in the optical bandgap and conduction-band filling for the doped ZnO, in which the Fermi level was determined to be approximately 0.3 eV below the conduction-band minimum [25].

The buildup of trap states induced by chemisorbed hydroxyl group exists in the grain boundary, and this in turn induces charge-carrier trapping that causes carrier-concentration degradation [13,26,27].

To support that the degradation centers are located in grain boundaries, infrared-reflectance spectra were also investigated to separately analyze the electrical characteristics of intragains. The reflectance due to the collective oscillation of free-electron gas can be described by the Drude model [28,29]. The derivation of the dielectric function is as follows.

The equation of motion for the displacement  $x$  of the electron induced by the

AC electric field  $\mathbf{E}(t)$  (with consideration of damping rate  $\gamma$ ) is:

$$m_0 \frac{d^2 x}{dt^2} + m_0 \gamma \frac{dx}{dt} = -e\mathbf{E}(t), \quad (3)$$

$dx/dt$  is the electron velocity  $\mathbf{v}$  and scattering time  $\tau = 1/\gamma$  ( $\gamma$  is the damping rate).

Therefore:

$$m_0 \frac{d\mathbf{v}}{dt} + \frac{m_0 \mathbf{v}}{\tau} = -e\mathbf{E}. \quad (4)$$

Since  $m_0 \mathbf{v}$  is the momentum  $\mathbf{p}$ , so that:

$$\frac{d\mathbf{p}}{dt} = -\frac{\mathbf{p}}{\tau} - e\mathbf{E}, \quad (5)$$

where it has replaced the damping rate  $\gamma$  by the reciprocal of the damping time  $\tau$ . In an AC field of the form  $\mathbf{E}(t) = \mathbf{E}_0 e^{-i\omega t}$ , a solution of the electron motion has the form of  $x = x_0 e^{-i\omega t}$ . It means that the electron velocity also has a time variation of the form  $\mathbf{v} = \mathbf{v}_0 e^{-i\omega t}$ . On substituting this into Eq. (4), we obtain:

$$\mathbf{v}(t) = \frac{-e\tau}{m_0} \frac{1}{1 - i\omega\tau} \mathbf{E}(t). \quad (6)$$

Current density  $\mathbf{j}$  is related to the velocity  $\mathbf{v}$  and field  $\mathbf{E}$  through:

$$\mathbf{j} = -Ne\mathbf{v} = \sigma \mathbf{E}, \quad (7)$$

where  $\sigma$  is the electrical conductivity. On combining Eqns. (6) and (7), we obtain the AC conductivity  $\tilde{\sigma}(\omega)$ :

$$\tilde{\sigma}(\omega) = \frac{\sigma_0}{1 - i\omega\tau}, \quad (8)$$

where  $\sigma_0$  is the conductivity measured with DC electric fields ( $\sigma_0 = Ne^2\tau / m_0$ ).

The dielectric function can be written as:

$$\tilde{\varepsilon}(\omega) = 1 - \frac{4\pi ne^2}{m_0(\omega^2 + i\omega/\tau)}. \quad (9)$$

By comparing Eqns. (8) and (9), we see that the AC conductivity and the dielectric constant are related to each other through:

$$\tilde{\varepsilon}(\omega) = 1 + \frac{4\pi i}{\omega \tilde{\rho}(\omega)}, \quad (10)$$

where we have replaced the ac conductivity by the reciprocal of the ac resistivity  $\tilde{\rho}(\omega)$ . The free electron model (Eq. (10)) can be applied to doped semiconductors if it has some appropriate modifications. These are the effective mass and the contribution to the polarization due to the optical response of the bound electrons. This gives:

$$\tilde{\varepsilon}'(\omega) = \varepsilon_\infty + \frac{4\pi i}{\omega \tilde{\rho}(\omega)}, \quad (11)$$

$$\tilde{\rho}(\omega) = \frac{4\pi(1 - i\omega\tau)}{\omega_p^2\tau}, \quad (12)$$

where  $\tilde{\varepsilon}'(\omega)$ ,  $\varepsilon_\infty$ ,  $\tilde{\rho}(\omega)$ ,  $\omega_p$ , and  $\tau$  are the modified dielectric function, the high-frequency dielectric constant (assumed equal to 4.0 for ZnO), ac resistivity, plasma frequency, and scattering time, respectively. From  $\omega_p$  and  $\tau$  fitted with the

reflectance spectra of Fig. 2-7,  $\tilde{\rho}(\omega)$  can be estimated (Table 2-1). At infrared frequencies, the mean-free path of electrons is within the range of a few nm (with the scattering time on the order of femtoseconds [16]), which is much smaller than the typical grain size in this experiment ( $\sim 75$  nm: explained after the following Eq. (14)). Therefore, the intragrain properties can be achieved by optical methods [28-30].

In order to characterize the changes in grain-boundary resistivity, the Hall measurements (zero frequency) and optical measurements with  $\tilde{\rho}(0) \cong \rho_{intra} = 4\pi / \omega_p^2 \tau$  (Eq. (12)) were compared, where  $\rho_{intra}$  is the intragrain resistivity. The Hall resistivity  $\rho_{Hall}$  of polycrystalline thin films can be expressed with two serial components of  $\rho_{intra}$  and grain-boundary resistivity  $\rho_{GB}$  (see the inset in Fig. 2-8) [31,32]:

$$\rho_{Hall} = \frac{L_{intra}}{L_{intra} + L_{GB}} \rho_{intra} + \frac{L_{GB}}{L_{intra} + L_{GB}} \rho_{GB}, \quad (13)$$

where  $L_{intra}$  is the width of the neutral region in the grain, and  $L_{GB}$  is the width of grain boundary including adjacent depleted regions in the grain. Then, the grain-boundary resistivity is given by:

$$\rho_{GB} = \rho_{Hall} \left(1 + \frac{L_{intra}}{L_{GB}}\right) - \rho_{intra} \frac{L_{intra}}{L_{GB}}. \quad (14)$$

The grain size ( $L_{intra} + L_{GB}$ ) was measured to  $\sim 75$  nm by SEM and AFM, and the

$L_{GB}$  was assumed to be ~2 nm [18,33,34]. Consequently, the strong dependence of the grain-boundary resistivity on the DH exposure time is clearly observed, as shown in Fig. 2-8 and Table 2-2, confirming that the degradations arise from the grain boundaries.

The carrier-transport properties were also examined from the temperature dependence on the electrical characteristics. The samples show a strong metallic behavior of which the carrier concentration is independent of temperature due to the degeneracy by high doping, as shown in Fig. 2-9 [35]. The thermionic-field emission of electrons through the grain boundary having an effective energy barrier  $E_{b,eff}$  can be described by the Schottky-barrier model [36,37]:

$$\mu_{Hall} = \frac{eL}{\sqrt{2\pi m_e^* kT}} \exp\left(-\frac{E_{b,eff}}{kT}\right), \quad (15)$$

where  $\mu_{Hall}$ ,  $k$ ,  $T$ ,  $e$ , and  $L$  are the Hall-carrier mobility, Boltzmann constant, temperature, the electron charge, and grain size ( $L_{intra} + L_{GB}$ ), respectively. To figure out the scattering mechanism, the results were plotted by  $\mu_{Hall}\sqrt{T}$  vs.  $T^{-1}$ , and all the samples show exponential dependence indicating that grain-boundary scattering is a dominant mechanism despite the degeneracy with high carrier concentration (Figs. 2-10 and 2-11). The effective energy barrier increased from  $6.8 \pm 0.1$  to  $7.6 \pm 0.2$  meV with the increasing DH exposure, as shown in Fig. 2-12. (Note that the effective energy barrier is in the ~10 meV range for the



carrier concentration  $n \cong 5 \times 10^{19} \text{ cm}^{-3}$ , as previously reported [38].) The increase of potential-energy barrier can be well explained by the chemisorbed hydroxyl groups existing along the grain boundaries. The increases of the trap-state density and the accumulated positive carriers towards the depleted regions lead to a higher and wider energy barrier [23]. Figure 2-13 shows the energy-level scheme that illustrates the changes in effective grain-boundary barrier caused by the DH exposure. A humid and hot environment increases the potential-energy barrier, which limits the carrier-transport characteristics, resulting in the degradation of electrical properties in TCO.

Table. 2-1. Fitted parameters ( $\omega_p$ ,  $\tau$ ) and calculated values of optical carrier concentration ( $n_{opt}$ ) and mobility ( $\mu_{opt}$ ) for the ZnO:Al films with various DH exposure times.

<b>Damp-Heat Exposure Time</b>	<b><math>\omega_p</math> (eV)</b>	<b><math>\tau</math> (<math>10^{-15}</math> s)</b>	<b><math>n_{opt}</math> (<math>10^{20}</math> cm<math>^{-3}</math>)</b>	<b><math>\mu_{opt}</math> (cm<math>^2</math>/Vs)</b>
<b>0 h</b>	1.48	5.92	4.45	37.7
<b>140 h</b>	1.45	6.17	4.31	39.3
<b>240 h</b>	1.46	5.51	4.34	35.0
<b>500 h</b>	1.36	3.80	3.76	24.2
<b>800 h</b>	1.36	2.60	3.76	16.5

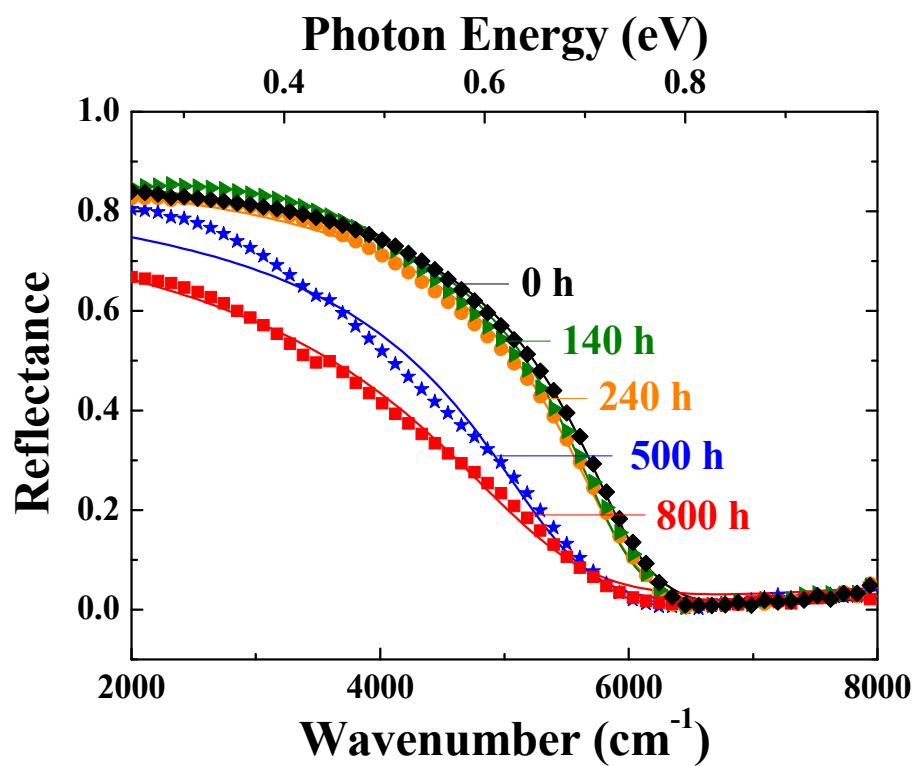


Fig. 2-7. (Color) IR reflectance with various DH exposure times, with the fitting results (solid lines) using the Drude model.

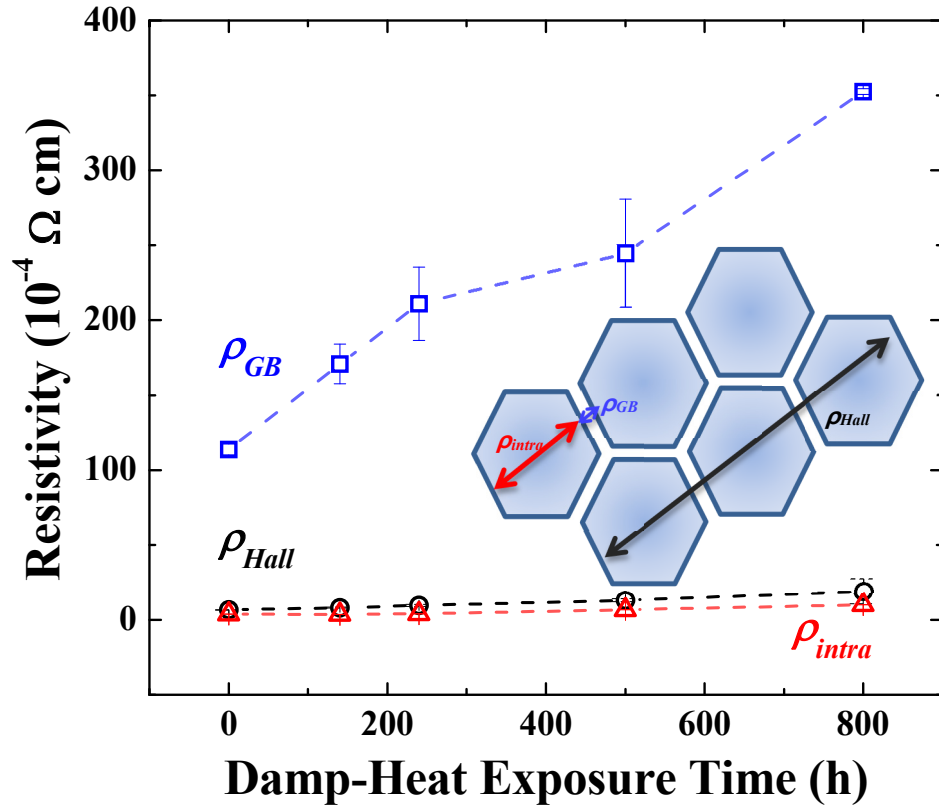


Fig. 2-8. (Color) Changes in the grain-boundary resistivity  $\rho_{GB}$  (calculated by Eq. (5)), Hall resistivity  $\rho_{Hall}$ , and intragrain resistivity  $\rho_{intra}$  as a function of DH exposure time.

Table. 2-1. Measured values of Hall-carrier concentration ( $n_{Hall}$ ) and mobility ( $\mu_{Hall}$ ), calculated values of intragrain-carrier concentration ( $n_{opt}$ ), mobility ( $\mu_{intra}$ ), Hall resistivity ( $\rho_{Hall}$ ), intragrain resistivity ( $\rho_{intra}$ ), and grain-boundary resistivity ( $\rho_{GB}$ ) for the ZnO:Al films with various DH exposure times.

DH Exposure Time	$n_{Hall}$ ( $10^{20} \text{ cm}^{-3}$ )	$\mu_{Hall}$ ( $\text{cm}^2/\text{Vs}$ )	$n_{intra}$ ( $10^{20} \text{ cm}^{-3}$ )	$\mu_{intra}$ ( $\text{cm}^2/\text{Vs}$ )	$\rho_{Hall}$ ( $10^{-4} \Omega \text{ cm}$ )	$\rho_{intra}$ ( $10^{-4} \Omega \text{ cm}$ )	$\rho_{GB}$ ( $10^{-4} \Omega \text{ cm}$ )
<b>0 h</b>	3.02	31.5	4.41	37.7	6.66	3.73	113.8
<b>140 h</b>	2.81	27.4	4.27	39.3	8.15	3.69	170.7
<b>240 h</b>	2.54	26.3	4.30	36.0	9.63	4.11	211.0
<b>500 h</b>	2.12	23.0	3.66	25.8	13.2	6.86	244.8
<b>800 h</b>	1.92	17.0	3.73	16.5	19.2	10.01	352.6

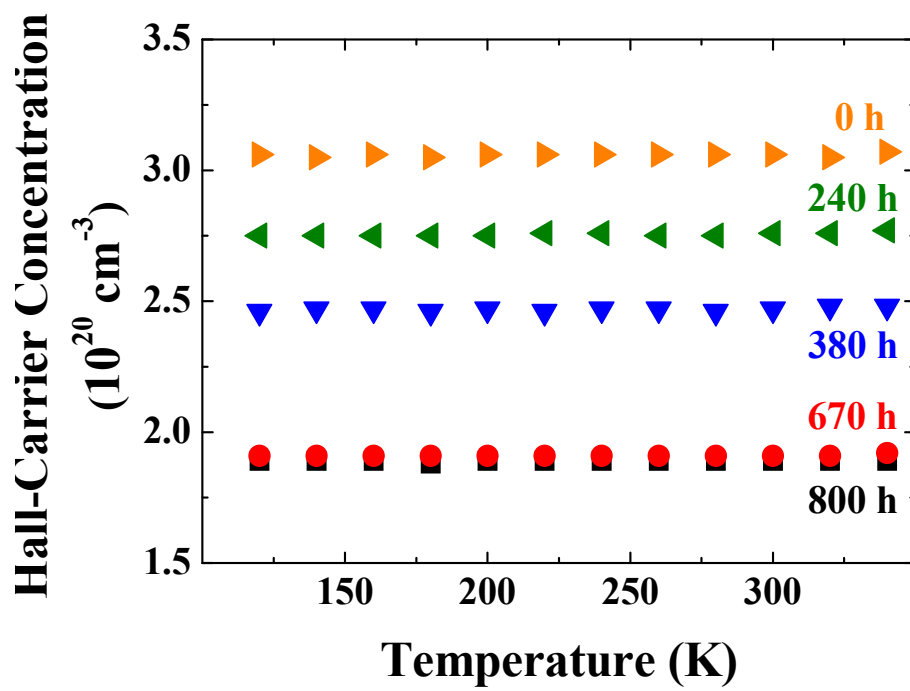


Fig. 2-9. (Color) Temperature dependence on electrical characteristics with various DH exposure times: Hall-carrier concentration.

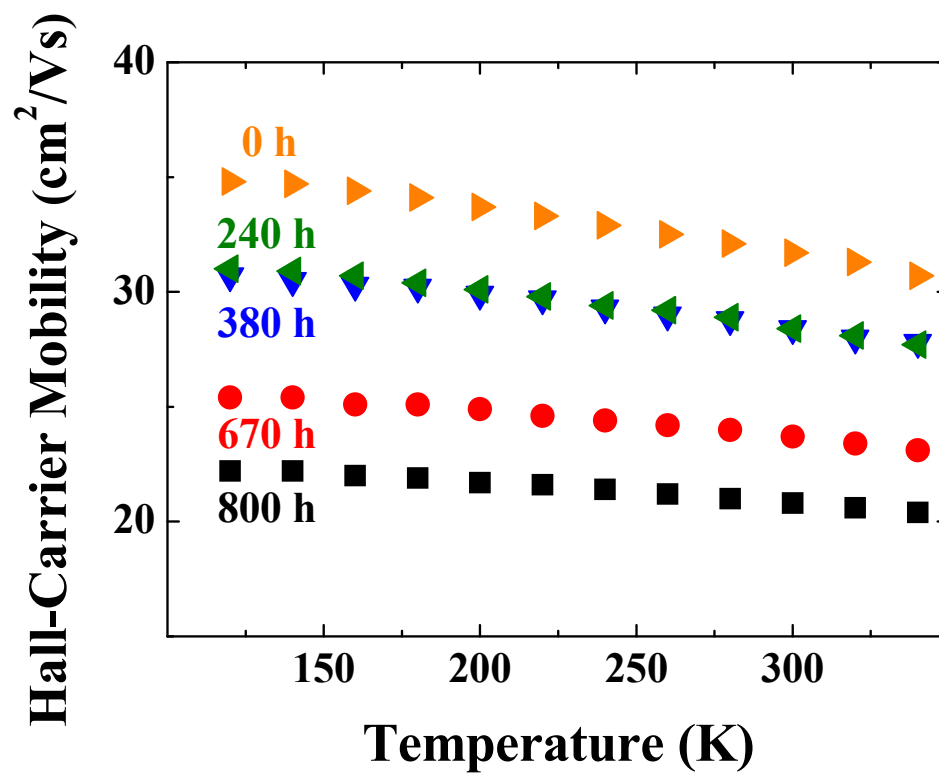


Fig. 2-10. (Color) Temperature dependence on electrical characteristics with various DH exposure times: Hall-carrier mobility.

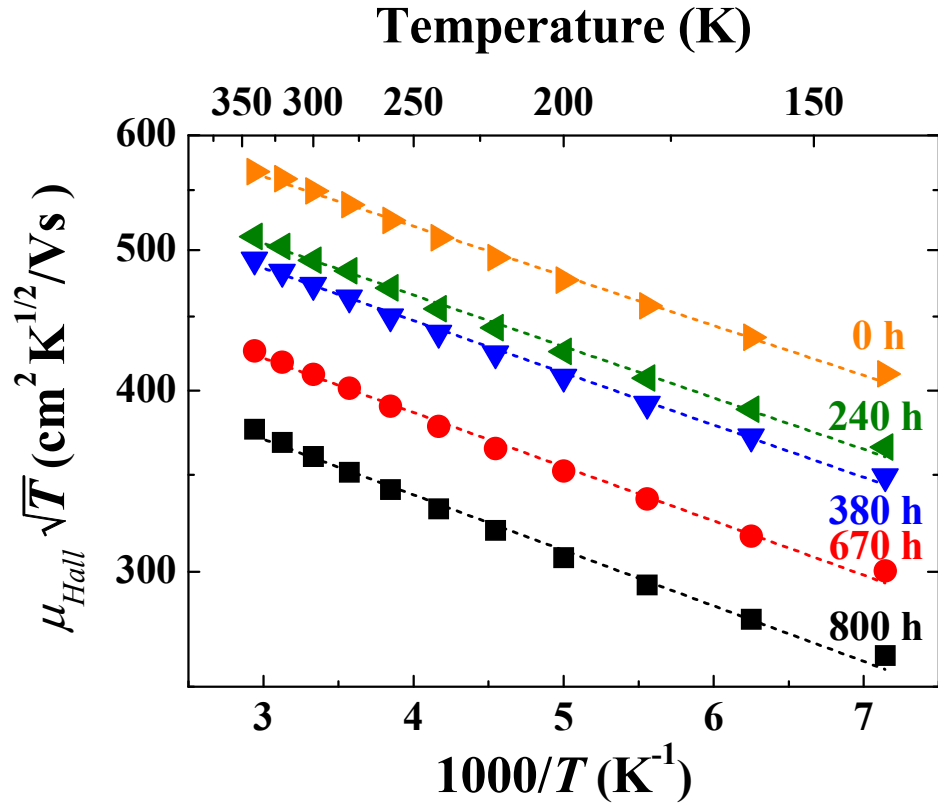


Fig. 2-11. (Color) Temperature dependence on electrical characteristics with various DH exposure times. Plot of  $\mu_{Hall} \sqrt{T}$  vs. inverse temperature, with the fitted lines by Eq. (15).



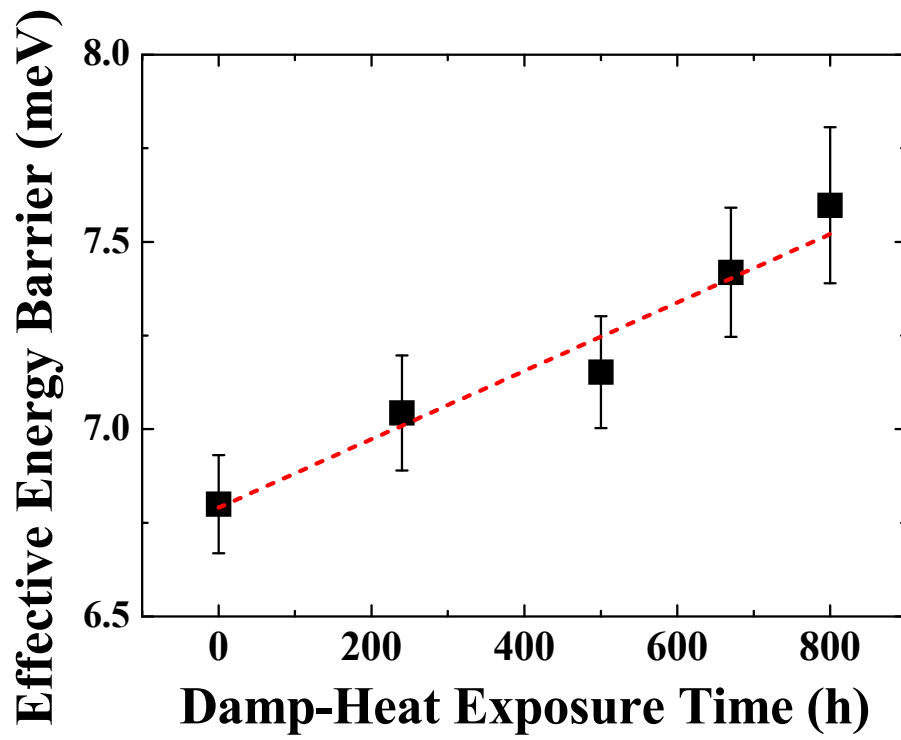


Fig. 2-12. (Color) Temperature dependence on electrical characteristics with various DH exposure times: Changes in the effective energy barrier  $E_{b,eff}$  obtained from the slopes in Fig. 2-11 as a function of DH exposure.

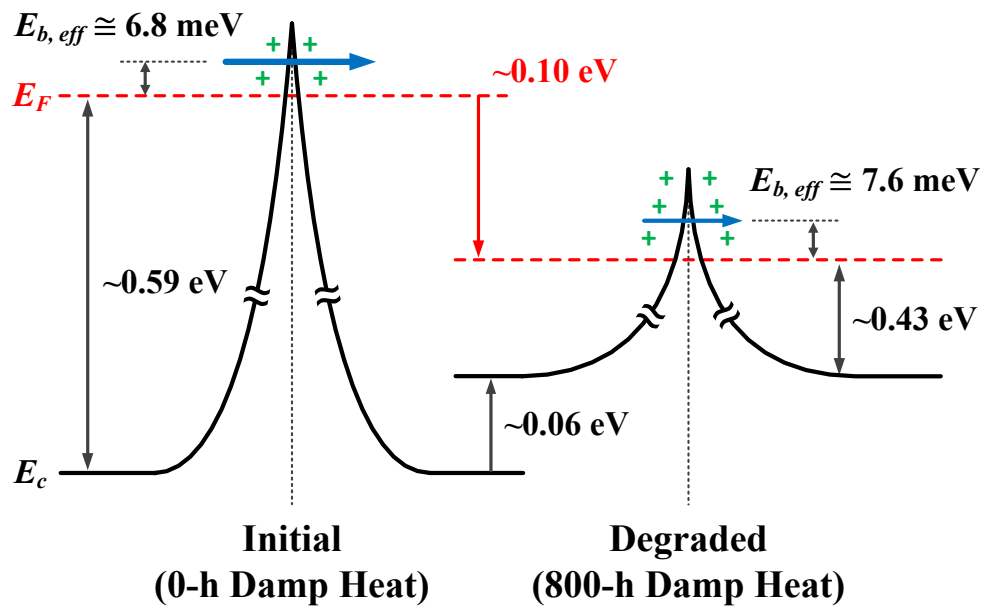


Fig. 2-13. (Color) Schematic figure showing the change in effective grain-boundary barrier  $E_{b,eff}$  (Figs. 2-11 and 12) caused by the damp-heat tests, with other energy levels from Fig. 2-6.

## 2.4. Conclusions

The stability and degradation mechanisms of ZnO:Al films were investigated under a controlled damp-heat environment. The degradation behavior was comparatively analyzed in the aspects of both Fermi-level shifts and changes in carrier-transport characteristics of the grain boundary and intragrain. The x-ray photoelectron spectroscopy and temperature-dependent electrical properties reveal that the chemisorbed OH<sup>-</sup> in grain boundaries acts as charge trapping and scattering centers, causing the degradation of carrier concentration and mobility. The comprehensive study of degradation behavior in such harsh environment opens up the window of developing highly reliable photovoltaic devices and displays for stable outdoor performance.

## 2.5. References

1. K. Schulze, B. Maennig, K. Leo, Y. Tomita, C. May, J. Hüpkes, E. Brier, E. Reinold, and P. Bäuerle, “Organic Solar Cells on Indium Tin Oxide and Aluminum Doped Zinc Oxide Anodes,” *Appl. Phys. Lett.* **91**, 073521 (2007).
2. T. K. Todorov, K. B. Reuter, and D. B. Mitzi, “High-Efficiency Solar Cell with Earth-Abundant Liquid-Processed Absorber,” *Adv. Mater.* **22**, E156 (2010).
3. J. Piriš, N. Kopidakis, D. C. Olson, S. E. Shaheen, D. S. Ginley, and G. Rumbles, “The Locus of Free Charge-Carrier Generation in Solution-Cast  $\text{Zn}_{1-x}\text{Mg}_x\text{O}$ /Poly(3-hexylthiophene) Bilayers for Photovoltaic Applications,” *Adv. Funct. Mater.* **17**, 3849 (2007).
4. J. Müller, B. Rech, J. Springer, and M. Vanecek, “TCO and Light Trapping in Silicon Thin Film Solar Cells,” *Sol. Energy* **77**, 917 (2004).
5. Y. Kim, W. Lee, D.-R. Jung, J. Kim, S. Nam, H. Kim, and B. Park, “Optical and Electronic Properties of Post-Annealed ZnO:Al Thin Films,” *Appl. Phys. Lett.* **96**, 171902 (2010).
6. W. Lee, S. Shin, D.-R. Jung, J. Kim, C. Nahm, T. Moon, and B. Park, “Investigation of Electronic and Optical Properties in Al-Ga Codoped ZnO Thin Films,” *Curr. Appl. Phys.* **12**, 628 (2012).
7. T. Moon, J. H. Jun, H. Lee, W. Yoon, S. Kim, B.-K. Lee, H.-C. Lee, W. Kim, S.-W. Ahn, S. Lee, and H.-M. Lee, “Additional Coating Effects on Textured

- ZnO:Al Thin Films as Transparent Conducting Oxides for Thin-Film Si Solar Cells,” *Prog. Photovoltaics* **20**, 294 (2012).
8. C.-H. Lin, S. Chattopadhyay, C.-W. Hsu, M.-H. Wu, W.-C. Chen, C.-T. Wu, S.-C. Tseng, J.-S. Hwang, J.-H. Lee, C.-W. Chen, C.-H. Chen, L.-C. Chen, and K.-H. Chen, “Enhanced Charge Separation by Sieve-Layer Mediation in High-Efficiency Inorganic-Organic Solar Cells,” *Adv. Mater.* **21**, 759 (2009).
  9. S. Park, S. J. Tark, J. S. Lee, H. Lim, and D. Kim, “Effects of Intrinsic ZnO Buffer Layer based on P3HT/PCBM Organic Solar Cells with Al-doped ZnO Electrode,” *Solar Energ. Mater. Solar C.* **93**, 1020 (2009).
  10. M. Berginski, J. Hüpkes, M. Schulte, G. Schöpe, H. Stiebig, and B. Rech, The Effect of Front ZnO:Al Surface Texture and Optical Transparency on Efficient Light Trapping in Silicon Thin-Film Solar Cells,” *J. Appl. Phys.* **101**, 074903 (2002).
  11. T. Miyata, Y. Ohtani, T. Kuboi, and T. Minami, “Stability of Nano-Thick Transparent Conducting Oxide Films for use in a Moist Environment,” *Thin Solid Films* **516**, 1354 (2008).
  12. F. Ruske, M. Roczen, K. Lee, M. Wimmer, S. Gall, J. Hüpkes, D. Hrunski, and B. Rech, “Improved Electrical Transport in Al-Doped Zinc Oxide by Thermal Treatment,” *J. Appl Phys.* **107**, 013708 (2010).
  13. W. Lin, R. Ma, J. Xue, and B. Kang, “RF Magnetron Sputtered ZnO:Al Thin

- Films on Glass Substrates: A Study of Damp Heat Stability on their Optical and Electrical Properties,” *Solar Energ. Mater. Solar C.* **91**, 1902 (2007).
14. F. J. Pern, S. H. Glick, X. Li, C. DeHart, T. Gennett, M. Contreras, and T. Gessert, “Stability of TCO Window Layers for Thin-Film CIGS Solar Cells upon Damp Heat Exposure – Part III,” *Proc. SPIE* **7412**, 74120K (2009).
  15. T. L. Chen, D. S. Ghosh, D. Krautz, S. Cheylan, and V. Pruneri, “Highly Stable Al-Doped ZnO Transparent Conductors using an Oxidized Ultrathin Metal Capping Layer at its Percolation Thickness,” *Appl. Phys. Lett.* **99**, 093302 (2011).
  16. D.-W. Kang, J.-Y. Kwon, D.-J. Lee, and M.-K. Han, “Boron and Aluminum Codoped ZnO Transparent Conducting Films with High Electrical Stability,” *J. Electrochem. Soc.* **159**, H61 (2012).
  17. E. Burstein, “Anomalous Absorption Limit in InSb,” *Phys. Rev.* **93**, 632 (1954).
  18. T. S. Moss, “The Interpretation of the Properties of Indium Antimonide,” *Proc. Phys. Soc. B* **67**, 775 (1954).
  19. E. Mollwo and R. Till, “Optical Properties of Single Crystals of Cadmium Selenide in the Infrared,” *Z. Physik* **216**, 315 (1968).
  20. M. N. Islam, T. B. Ghosh, K. L. Chopra, and H. N. Acharya, “XPS and X-ray Diffraction Studies of Aluminum-Doped Zinc Oxide Transparent Conducting Films,” *Thin Solid Films* **280**, 20 (1996).

21. J. F. Chang and M. H. Hon, “The Effect of Deposition Temperature on the Properties of Al-Doped Zinc Oxide Thin Films,” *Thin Solid Films* **386**, 79 (2001).
22. J.-H. Kang, D. W. Kim, J. H. Kim, Y. S. Lim, M.-H. Lee, W.-S. Seo, H. J. Choi, K. H. Seo, and M. G. Park, “Improved Thermal Stability of ZnO Transparent Conducting Films with a ZnO Overlayer,” *Thin Solid Films* **519**, 6840 (2011).
23. J. Steinhauser, S. Meyer, M. Schwab, S. Faÿ, C. Ballif, U. Kroll, and D. Borrello, “Humid Environment Stability of Low Pressure Chemical Vapor Deposited Boron Doped Zinc Oxide used as Transparent Electrodes in Thin Film Silicon Solar Cells,” *Thin Solid Films* **520**, 558 (2011).
24. S. C. Jain, J. M. McGregor, and Roulston, “Band-Gap Narrowing in Novel III-V Semiconductors,” *J. Appl. Phys.* **68**, 3747 (1990).
25. K. Ellmer, A. Klein, and B. Rech, “Transparent Conductive Zinc Oxide: Basics and Applications in Thin Film Solar Cells,” *Springer, Berlin*, 2008.
26. R. Jaramillo and S. Ramanathan, “Electronic Granularity and the Work Function of Transparent Conducting ZnO:Al Thin Films,” *Adv. Funct. Mater.* **21**, 4068 (2011).
27. A. Rothschild, Y. Komem, A. Levakov, N. Ashkenasy, and Y. Shapira, “Electronic and Transport Properties of Reduced and Oxidized Nanocrystalline TiO<sub>2</sub> Films,” *Appl. Phys. Lett.* **82**, 574 (2003).

28. Z. C. Jin, I. Hamberg, and C. G. Granqvist, "Optical Properties of Sputter-Deposited ZnO:Al Thin Films," *J. Appl. Phys.* **64**, 5117 (1988).
29. I. Hamberg and C. G. Granqvist, "Evaporated Sn-Doped In<sub>2</sub>O<sub>3</sub> Films: Basic Optical Properties and Applications to Energy-Efficient Windows," *J. Appl. Phys.* **60**, R123 (1986).
30. J. Steinhauser, S. Fay, N. Oliveira, E. Vallat-Sauvain, and C. Ballif, "Transition between Grain Boundary and Intragrain Scattering Transport Mechanisms in Boron-Doped Zinc Oxide Thin Films," *Appl. Phys. Lett.* **90**, 142107 (2007).
31. M. M. Mandurah, K. C. Saraswat, and T. I. Kamins, "A Model for Conduction in Polycrystalline Silicon-Part I: Theory," *IEEE Trans. Electron Devices* **28**, 1163 (1981).
32. N. C. C. Lu, L. Gerzberg, C.-Y. Lu, and J. D. Meindl, "Modeling and Optimization of Monolithic Polycrystalline Silicon Resistors," *IEEE Trans. Electron Devices* **28**, 818 (1981).
33. R. W. Siegel, "Cluster-Assembled Nanophase Materials," *Annu. Rev. Mater. Sci.* **21**, 559 (1991).
34. J. C. Fisher, "Calculation of Diffusion Penetration Curves for Surface and Grain Boundary Diffusion," *J. Appl. Phys.* **22**, 74 (1951).
35. K. Ellmer and R. Mientus, "Carrier Transport in Polycrystalline ITO and ZnO:Al II: The Influence of Grain Barriers and Boundaries," *Thin Solid Films*



- 516**, 5829 (2008).
36. J. W. Orton, "Interpretation of Hall Mobility in Polycrystalline Thin Films," *Thin Solid Films* **86**, 351 (1981).
37. J. Y. Seto, "The Electrical Properties of Polycrystalline Silicon Films," *J. Appl. Phys.* **46**, 5247 (1975).
38. S. Y. Myong, J. Steinhauser, R. Schlüchter, S. Fay, E. Vallat-Sauvain, A. Shah, C. Ballif, and A. Rüfenacht, "Temperature Dependence of the Conductivity in Large-Grained Boron-Doped ZnO Films," *Solar Energ. Mater. Solar C.* **91**, 1269 (2007).

## Chapter 3.

### Summary

In this thesis, quantitative investigation on degradation behaviors in a controlled damp-heat (DH) environment (humid and hot atmosphere) is introduced for aluminum-doped ZnO (ZnO:Al) thin films. ZnO:Al thin films (thickness of 1.5  $\mu\text{m}$ ) were deposited by rf magnetron sputtering using the ZnO:Al target. The sputtering was performed under an Ar atmosphere at 400°C, with an rf power of 75 W and an operating pressure of 5 mTorr. After deposition, the ZnO:Al films were exposed to a damp-heat (DH) atmosphere of a relative humidity of 85% and a temperature of 85°C, for up to 800 h.

The continuous degradation behaviors of the carrier mobility and carrier concentration were observed after 800 h of DH exposure. To characterize the carrier-concentration degradation, the optical bandgap was evaluated by Tauc's relation, and the conduction-band filling was quantitatively estimated to be ~0.59 eV and ~0.43 eV for 0-h and 800-h DH exposure, respectively, from the Burstein-Moss model. Then, to correlate the energy-level shifts of  $E_g^{op}$  and the carrier-concentration degradation, the XPS core-level spectra of Zn 2p were analyzed. For the pristine ZnO:Al compared to ZnO, the upshift of the Fermi level by ~0.6 eV is shown due to the electron population within the conduction band. After the DH treatment of 800 h, the Fermi energy is decreased by ~0.1 eV, which is well correlated with the  $E_g^{op}$  analyses and deduced conduction-band filling.

The O 1s peaks of the ZnO:Al films were also analyzed to identify the chemisorbed hydroxyl groups in humid atmosphere. With two XPS peaks at  $\sim 530.9$  eV ( $\text{O}^{2-}$  binding with Zn or substitutional Al) and  $\sim 532.5$  eV ( $\text{OH}^-$  in metal-OH bonds), the integrated-intensity ratio of  $\text{OH}^-/\text{O}^{2-}$  was  $\sim 23\%$  for the initial ZnO:Al film, while the ratio significantly increases to  $\sim 44\%$  after the DH exposure of 800 h. This result indicates the increase of chemisorbed  $\text{OH}^-$  with the exposure to the humid environment, probably along the grain boundaries which are easy diffusion paths for the  $\text{OH}^-$  species.

To support that the degradation centers are located in grain boundaries, infrared-reflectance spectra were also investigated to separately analyze the electrical characteristics of intragains. Consequently, the strong dependence of the grain-boundary resistivity on the DH exposure time is clearly observed, and it is confirming that the degradations arise from the grain boundaries. The carrier-transport properties were also examined from the temperature dependence on the electrical characteristics. The effective energy barriers increased from  $6.8 \pm 0.1$  to  $7.6 \pm 0.2$  meV with the increasing DH exposure. The increases of the trap-state density and the accumulated positive carriers towards the depleted regions lead to a higher and wider energy barrier. In conclusion, a humid and hot environment increases the potential-energy barrier, which limits the carrier-transport characteristics, resulting in the degradation of electrical properties in TCO. The comprehensive study of degradation behavior in such harsh environment opens up the window of developing highly reliable photovoltaic devices and displays for stable outdoor performance.

## Appendix 1.

### **\*Oriented Hierarchical TiO<sub>2</sub> Nanotubes on Ti Substrate: Evolution of Nanostructures for Dye-Sensitized Solar Cells**

#### **A.1.1. Introduction**

Flexible electrodes have been widely used to various applications such as solar cells, liquid crystal displays (LCD), transparent conducting films (TCFs), lithium-ion batteries, etc. [1-4]. In particular, lightweight and flexible dye-sensitized solar cells (DSSCs) have received much attention due to their low cost and extensive applications in portable devices [5-7]. Therefore, metal substrates or transparent plastic substrates (ITO/PET or ITO/PEN) are intensively investigated as a photoanode substrate for DSSCs [8-11]. Among them, Ti foil substrates have attracted more due to its good flexibility, superior electrical conductivity, high-temperature tolerance, and superior corrosion resistance.

On the other hand, vertically oriented one-dimensional (1-D) TiO<sub>2</sub> nanostructures including nanorods and nanotubes have been employed as

---

\*The work presented in Appendix 1 was submitted to *Electrochim. Acta* (2014) entitled, "Oriented Hierarchical TiO<sub>2</sub> Nanotubes on Ti Substrate: Evolution of Nanostructures for Dye-Sensitized Solar Cells,"  
Byungho Lee,<sup>+</sup> **Jae Ik Kim,**<sup>+</sup> Sangheon Lee, Taehyun Hwang, Seunghoon Nam, Jaewon Kim, Chohui Kim, Woojin Lee, and Byungwoo Park.\*

photoelectrode materials to provide direct electrical pathways for photogenerated electrons, thereby enhancing the charge transport and markedly improving the charge collection efficiency [12,13]. It is worth-noting that despite the advantages mentioned above, the device efficiency of DSSCs using the 1-D nanostructured photoanode remains primarily low due to their insufficient surface area in comparison to the nanoparticle network, resulting in limited dye adsorption capacity. Thus, the common strategy for improving the surface area of TiO<sub>2</sub> 1-D nanostructure-based DSSCs is the decoration of the mother-phase nanowire or nanotube with a large number of smaller nanoparticles or branches by a secondary nucleation [14]. However, the mentioned synthetic methods are generally complicated and time-consuming. Furthermore, the proposed mechanisms of nanostructural formation are still lacking, even though the understanding on the establishment of the nanostructures is essential for the practical applications to photovoltaic devices.

Herein, we report a facile route to hierarchically structured porous TiO<sub>2</sub> nanotube arrays composed of a highly-oriented anatase TiO<sub>2</sub> nanocrystals on Ti substrate, and investigate the hydrothermal dehydration process on the topotactic transformation of nanostructures. The resulting hierarchically structured porous nanotubes are adopted as photoelectrodes in DSSCs, exhibiting a higher dye loading due to the presence of large surface area, related to their truncated wedge-

shape nanostructures. Also, the optimum nanostructures are examined for the light-harvesting efficiency, and correlated with the surface area, charge transport, and carrier lifetime.

### **A.1.2. Experimental Section**

Herein, we report a facile route to hierarchically structured porous TiO<sub>2</sub> nanotube arrays composed of a highly-oriented anatase TiO<sub>2</sub> nanocrystals on Ti substrate, and investigate the hydrothermal dehydration process on the topotactic transformation of nanostructures. The resulting hierarchically structured porous nanotubes are adopted as photoelectrodes in DSSCs, exhibiting a higher dye loading due to the presence of large surface area, related to their truncated wedge-shape nanostructures. Also, the optimum nanostructures are examined for the light-harvesting efficiency, and correlated with the surface area, charge transport, and carrier lifetime.

#### **A.1.2.1. Synthesis of 1-D Nanostructures**

Oriented TiO<sub>2</sub> 1-D nanostructures on titanium foil are synthesized by the following three-step processes. First, vertically aligned sodium bititanate (Na<sub>2</sub>Ti<sub>2</sub>O<sub>5</sub>·H<sub>2</sub>O) nanowire arrays were prepared using a hydrothermal treatment in an alkaline environment. The titanium foil (0.25 mm: Sigma Aldrich) was cleaned

in an ultrasonic bath for 30 min in a mixture of acetone, deionized water, and isopropyl alcohol with the volume ratios of 1:1:1. Then, the as-cleaned foil was placed against the wall of a 210 mL Teflon-lined stainless steel autoclave containing 70 mL of 1 M NaOH aqueous solution. The sealed autoclave was kept at 220°C for 24 h. After the hydrothermal treatment, the prepared samples were rinsed with deionized water. In the second step, the nanostructured foil was dipped in a 0.6 M HCl aqueous solution for 1 h to exchange sodium ions by hydrogen ions, followed by washing the foil with deionized water. In the third step, as a dehydration process, the prepared samples were hydrothermally treated again in a 210 mL Teflon-lined stainless steel autoclave, filled with 70 mL of deionized water. The autoclave was kept at 180°C for 1.5 - 10 h. Then, the as-synthesized nanostructured titanium foil was rinsed with deionized water and ethanol, sequentially.

#### **A.1.2.2. Device Fabrication**

For a solar cell application, the as-prepared samples were annealed at 450°C for 1 h in ambient air. In order to improve the solar cell efficiency, the as-prepared samples (after the third step) were treated with 40 mM titanium chloride (TiCl<sub>4</sub>: Aldrich, St. Louis, U.S.A.) aqueous solution by immersing the samples in this solution for 30 min at 70°C. The films were then heat-treated at 450°C for 1 h.

The films were immersed in 0.3 mM anhydrous ethanol solution of N719 dye ( $\text{RuL}_2(\text{NCS})_2 \cdot 2\text{TBA}$ ,  $\text{L} = 2,2'$ -bipyridyl-4,4'-dicarboxylic acid,  $\text{TBA}$  = tetrabutylammonium; Solaronix) for 2 days at room temperature. The Pt counter electrode was deposited on the fluorine-doped tin oxide (FTO, TEC 8; Pilkington) substrate by rf magnetron sputtering. The sensitized electrode and Pt counter electrode were sealed with thermoplastic foil (25  $\mu\text{m}$ ; DuPont) for back-side illumination in which light comes to the cell through the Pt counter electrode, and the iodine-based redox electrolyte (AN-50; Solaronix) was injected between the two electrodes.

### **A.1.2.3. Characterization**

The prepared electrode was analyzed by x-ray diffraction (XRD, D8 Advance; Bruker), and the morphology of nanostructure was observed using field-emission scanning electron microscopy (FE-SEM, JSM-6330F; JEOL, Japan). High-resolution transmission electron microscopy (HRTEM, JEM-3000F; JEOL, Japan) was used to identify the crystal structures and morphological transitions. The photocurrent-voltage ( $J$ - $V$ ) curves were obtained using a solar cell measurement system (K3000; McScience, Korea) under a solar simulator (Xenon lamp, air mass (AM) 1.5, 100  $\text{mW}/\text{cm}^2$ ). Electrochemical impedance spectra and open-circuit voltage decay curves were measured from a potentiostat (CHI 608C; CH



Instrumental Inc., Austin, U.S.A.) under AM 1.5 illumination at open-circuit voltage. The amount of adsorbed dye on photoanode was obtained by measuring absorption spectra of desorbed dye in a mixture of 0.1 M NaOH/ethanol with a volume ratio of 1:1 using an UV/Vis spectrophotometer (Lambda 20; Perkin-Elmer, Waltham, U.S.A.).

### **A.1.3. Results and Discussion**

In the second step of the synthesis, the  $\text{Na}_2\text{Ti}_2\text{O}_5 \cdot \text{H}_2\text{O}$  nanowires are converted to protonated bititanate ( $\text{H}_2\text{Ti}_2\text{O}_5 \cdot \text{H}_2\text{O}$ ) nanowires through an ion-exchange reaction with its prior morphology unchanged [15]. Afterwards, the hydrothermal dehydration process leads to the  $\text{TiO}_2$  nanostructures (third step,  $180^\circ\text{C}$  in  $\text{H}_2\text{O}$ ). The effects of the dehydration time on the crystal structure and phase transition were investigated with XRD (Fig. A1-1). Complete transformation from orthorhombic  $\text{H}_2\text{Ti}_2\text{O}_5 \cdot \text{H}_2\text{O}$  (JCPDS #47-0124) to tetragonal  $\text{TiO}_2$  (anatase, JCPDS #21-1272) takes more than 4.5-h dehydration. The  $\text{H}_2\text{Ti}_2\text{O}_5 \cdot \text{H}_2\text{O}$  and  $\text{TiO}_2$  arrays exhibit the oriented direction of [010] and [100] and primarily normal to the titanium foil, respectively; and was confirmed by TEM (in the following Fig. A1-3).

Figures A1-2(a) and (b) are the cross-sectional SEM images of the  $\text{H}_2\text{Ti}_2\text{O}_5 \cdot \text{H}_2\text{O}$  nanowire array, and the average thickness is observed to be  $\sim 19 \mu\text{m}$ .

After the hydrothermal dehydration of the  $\text{H}_2\text{Ti}_2\text{O}_5\cdot\text{H}_2\text{O}$  nanowire in water, the morphology and thickness of the nanowire array underwent significant changes. The grown nanoparticles on the surface of nanowires are observed after 1.5 h of hydrothermal dehydration (Fig. A1-2(c)). When the dehydration time extended, the size and the number of nanoparticles increased accordingly, and afterward changed into hierarchical nanotube whose diameter is thicker than that of the  $\text{H}_2\text{Ti}_2\text{O}_5\cdot\text{H}_2\text{O}$  nanowire (Figs. A1-2(d) and (e)). The continuous growth of anatase crystallites was estimated from  $\sim 14.4$  nm (1.5 h) to  $\sim 29.4$  nm for [100] direction, and  $\sim 4.6$  nm (1.5 h) to  $\sim 13.0$  nm for [001] direction after 10 h, as shown in Fig. A1-2(f). The sizes along the [100] direction were estimated by a Scherrer formula from the full width at half maximum (FWHM) of diffraction peaks (Fig. A1-1) [16,17]. Meanwhile, the 1-D nanostructures tend to be cut off as the time of hydrothermal treatment increases. For this reason, the thickness of nanostructure arrays decreases from  $\sim 19$   $\mu\text{m}$  (as-prepared  $\text{H}_2\text{Ti}_2\text{O}_5\cdot\text{H}_2\text{O}$ ) to  $\sim 13$   $\mu\text{m}$  (hydrothermal treatment time of 10 h, anatase) (Table A1-1).

The morphological and structural changes are further characterized by TEM and HRTEM. The  $\text{H}_2\text{Ti}_2\text{O}_5\cdot\text{H}_2\text{O}$  nanowire with the diameter of  $\sim 75$  nm is shown in Fig. A1-3(a). The spacing between lattice fringes corresponds to the (110) planes of  $\text{H}_2\text{Ti}_2\text{O}_5\cdot\text{H}_2\text{O}$  with  $d_{(110)} = 0.37$  nm. Figure A1-3(b) shows the morphology of 1.5-h dehydration. It is confirmed that  $\text{TiO}_2$  nanocrystals with the

exposed (001) facets gradually grow from the surface of nanowire. The interplanar spacing of 0.35 nm (Fig. A1-3(b)) corresponds to the  $d$ -spacing of anatase (101) planes. Moreover, the measured interfacial angle between the truncated facet and the surrounding facet is  $68.3^\circ$ , confirming the angle between (101) and (001) [18]. This process can be explained by the consecutive dissolution and nucleation which accompany the volume change during the phase transition. Nucleation of  $\text{TiO}_2$  occurs on the surface of nanowire where  $\text{H}_2\text{Ti}_2\text{O}_5 \cdot \text{H}_2\text{O}$  acts as a Ti source by dissolution during the dehydration step [19]. Consequently, the  $\text{H}_2\text{Ti}_2\text{O}_5 \cdot \text{H}_2\text{O}$  nanowires transform to anatase nanotubes through the dehydration step in which the diameter of 1-D nanostructures diminishes from  $\sim 75$  nm ( $\text{H}_2\text{Ti}_2\text{O}_5 \cdot \text{H}_2\text{O}$  nanowire) to  $\sim 60$  nm (after 1.5 h), and finally changes to 100% anatase  $\text{TiO}_2$  nanotube with a diameter of  $\sim 125$  nm (after 4.5 h).

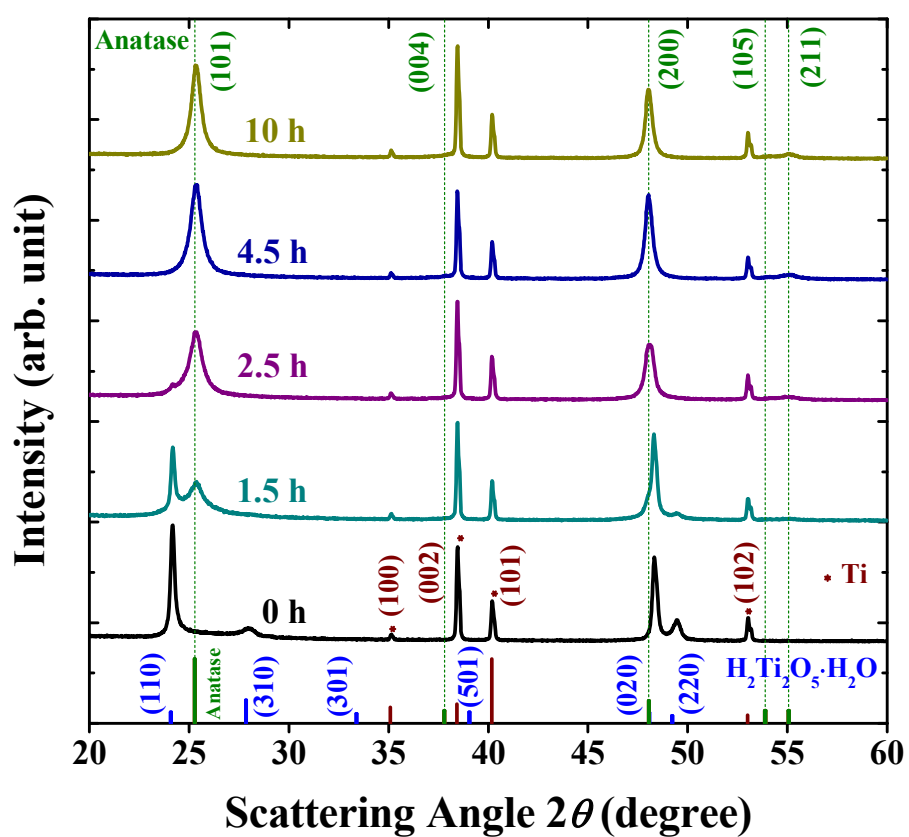


Fig. A1-1. (Color) X-ray diffraction of nanostructured titanium foils at various hydrothermal dehydration times.

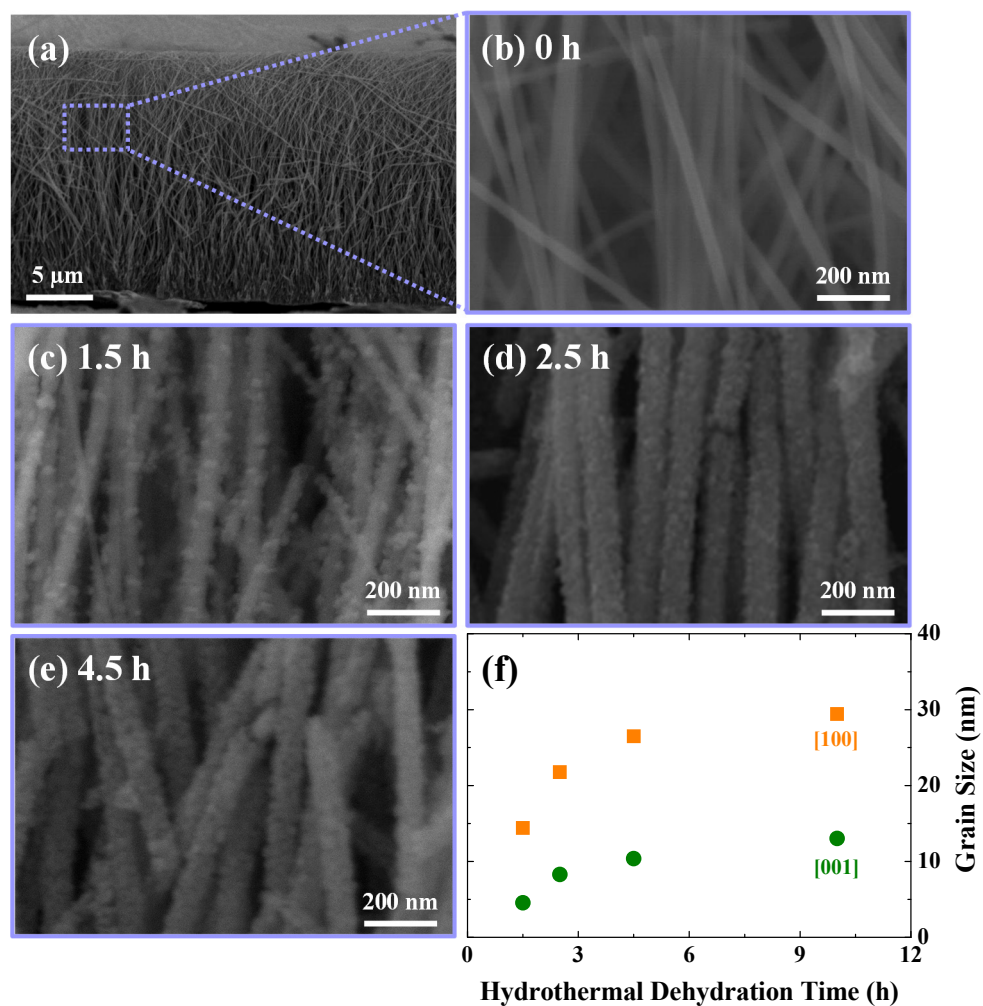


Fig. A1-2. (Color) Cross-sectional SEM images of 1-D nanostructures on titanium foils at various hydrothermal dehydration times: (a-b) 0 h, (c) 1.5 h, (d) 2.5 h, and (e) 4.5 h. (f) Grain size along the [100] and [001] directions for the nanostructures as a function of hydrothermal dehydration time.

During the 4.5-h hydrothermal dehydration, the morphology of nanostructure is changed to porous nanotube composed of densely-packed anatase nanocrystallite with truncated morphologies (Figs. A1-3(c) and (d)). Also, each nanocrystallite of nanotube exhibits highly faceted orientation which corresponds to the anatase (001) at the surface of the nanotube. It is widely known that the (001) facets of anatase  $\text{TiO}_2$  is much more reactive than the thermodynamically stable (101) facets, which are possibly favorable for the adsorption of dye, and effectively reduces charge recombination in DSSCs [18,20,21]. Thus, the nanotube made up of numerous nanocrystals of exposed (001) facet can be beneficial for the dye adsorption and charge transportation in DSSC system.

For the fabrication of DSSCs utilizing these nanostructures, the crystallinity of the arrays was confirmed by XRD (Fig. A1-4) with the grain-size evolution (Fig. A1-5). All of the samples after 1.5-h dehydration step exhibit pure anatase  $\text{TiO}_2$  with no other phases. Figure A1-6 shows the photocurrent-voltage curves of the DSSCs under back-side illumination. The improvements in the short-circuit current and power-conversion efficiency are observed as the dehydration increases (Table A1-1). However, after 10-h treatment, both the short-circuit current and open-circuit voltage decrease, indicating the existence of an optimum nanostructure for DSSCs.

Table A1-1. Photovoltaic performance of the DSSCs. Short-circuit current density ( $J_{sc}$ ), open-circuit voltage ( $V_{oc}$ ), fill factor ( $FF$ ), power-conversion efficiency ( $\eta$ ) of the DSSCs, dye adsorption, and average thickness with various hydrothermal dehydration times on the nanostructured photoelectrodes.

Cell	$J_{sc}$ (mA cm <sup>-2</sup> )	$V_{oc}$ (V)	$FF$	$\eta$	Dye Adsorption (mmol cm <sup>-3</sup> )	Thickness ( $\mu$ m)
0 h	1.93	0.49	0.68	0.64%	0.018	18.8
1.5 h	4.89	0.51	0.70	1.75%	0.037	17.2
2.5 h	5.53	0.52	0.68	1.96%	0.047	14.9
4.5 h	5.91	0.52	0.67	2.05%	0.061	12.7
10 h	5.56	0.50	0.71	1.96%	0.060	12.5
4.5 h (+ TiCl <sub>4</sub> )	9.94	0.56	0.66	3.66%	0.061	12.7

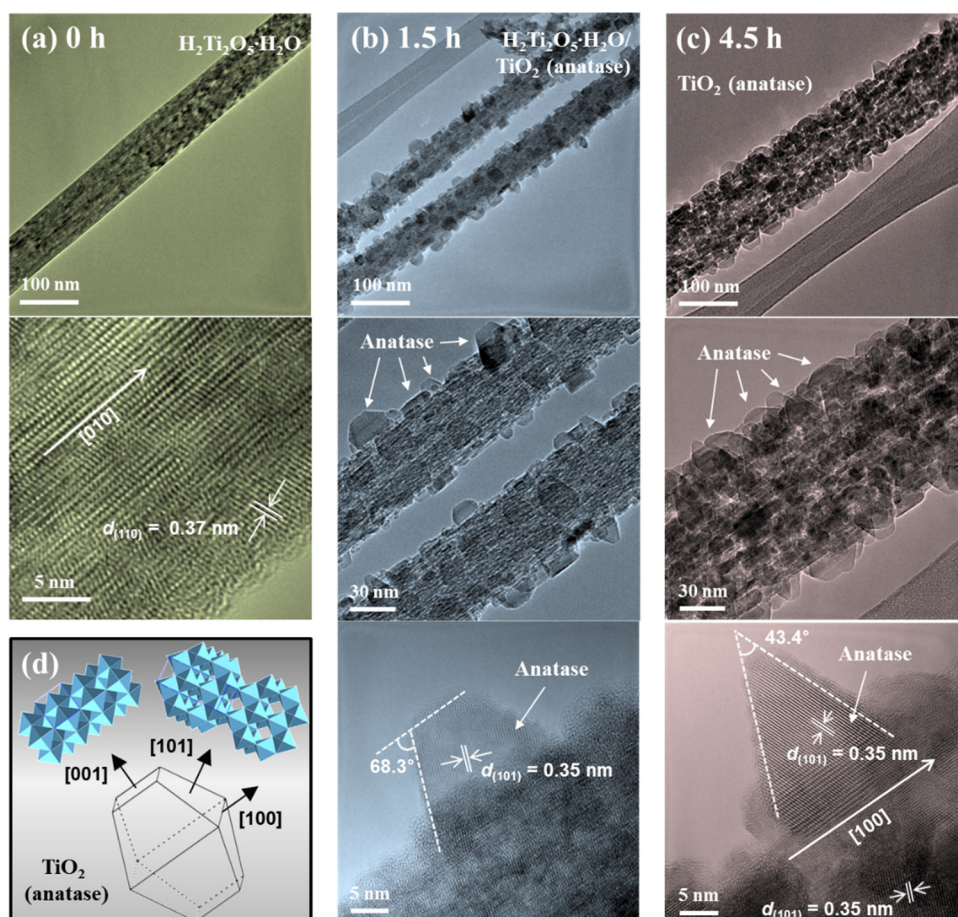


Fig. A1-3. (Color) Typical TEM and high-resolution TEM images of prepared nanostructures at various hydrothermal dehydration times: (a) 0 h, (b) 1.5 h, and (c) 4.5 h. (d) Schematic crystallographic structure of single-crystal TiO<sub>2</sub> (anatase).



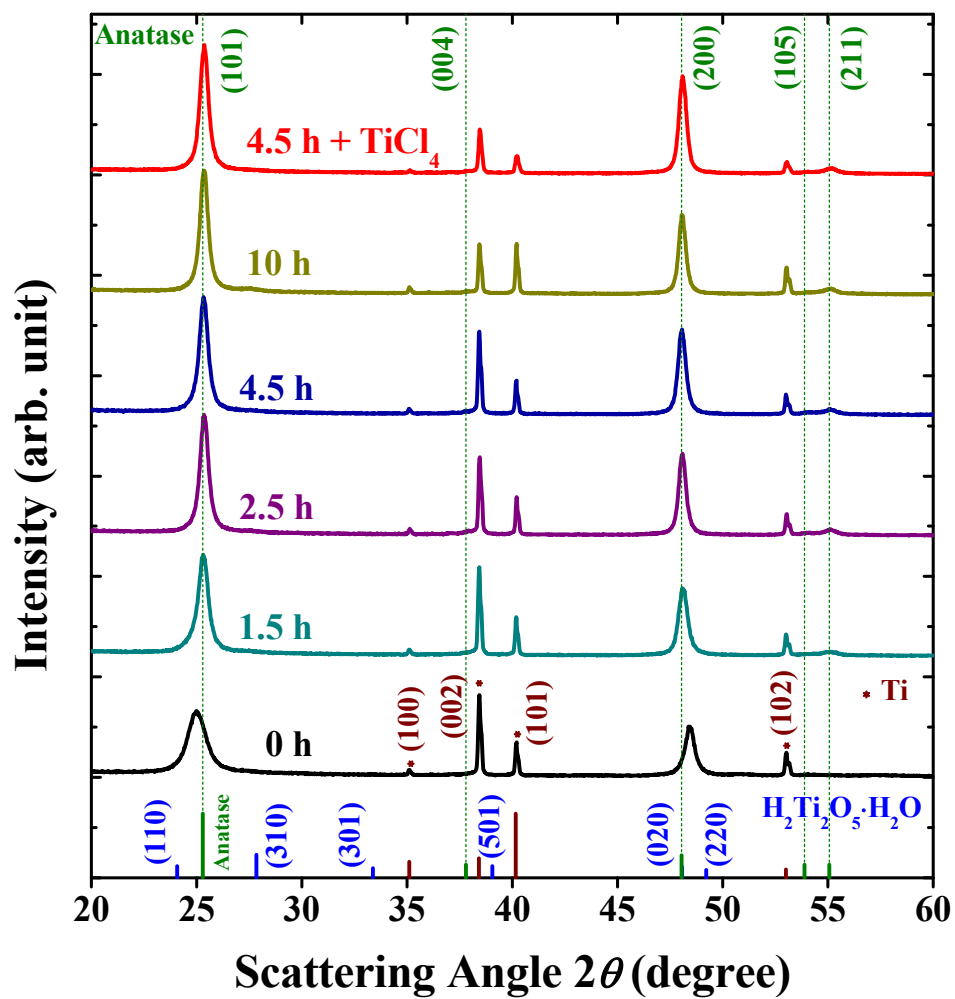


Fig. A1-4. (Color) X-ray diffraction of nanostructured titanium foils with various hydrothermal dehydration times (after annealing at 450°C for 1 h).

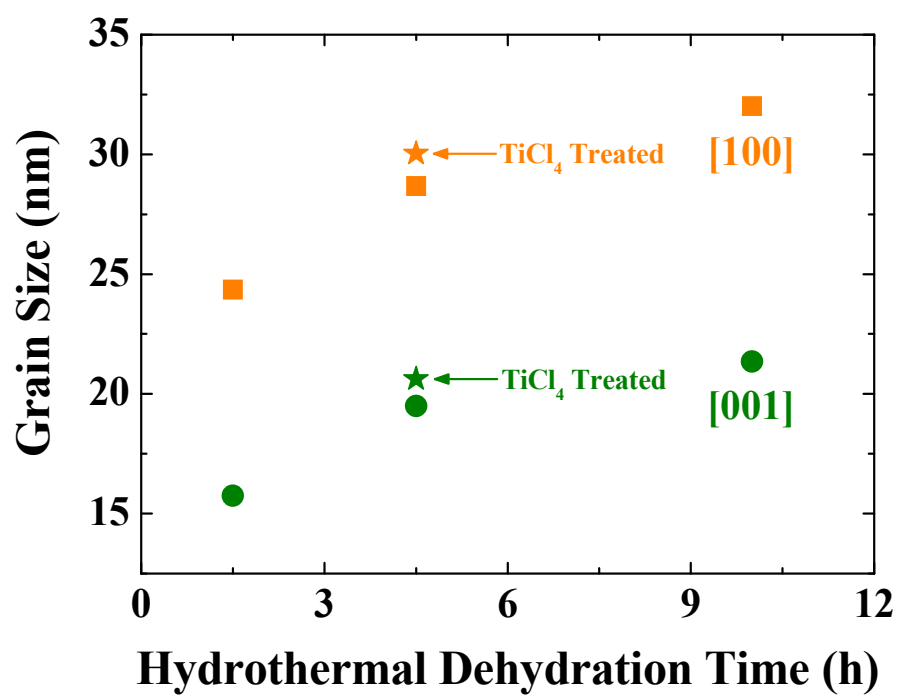


Fig. A1-5. (Color) Grain size along the [100] and [001] directions for the nanostructures as a function of hydrothermal dehydration time (after annealing at 450°C for 1 h). The grain size of TiCl<sub>4</sub> treated sample is also shown.

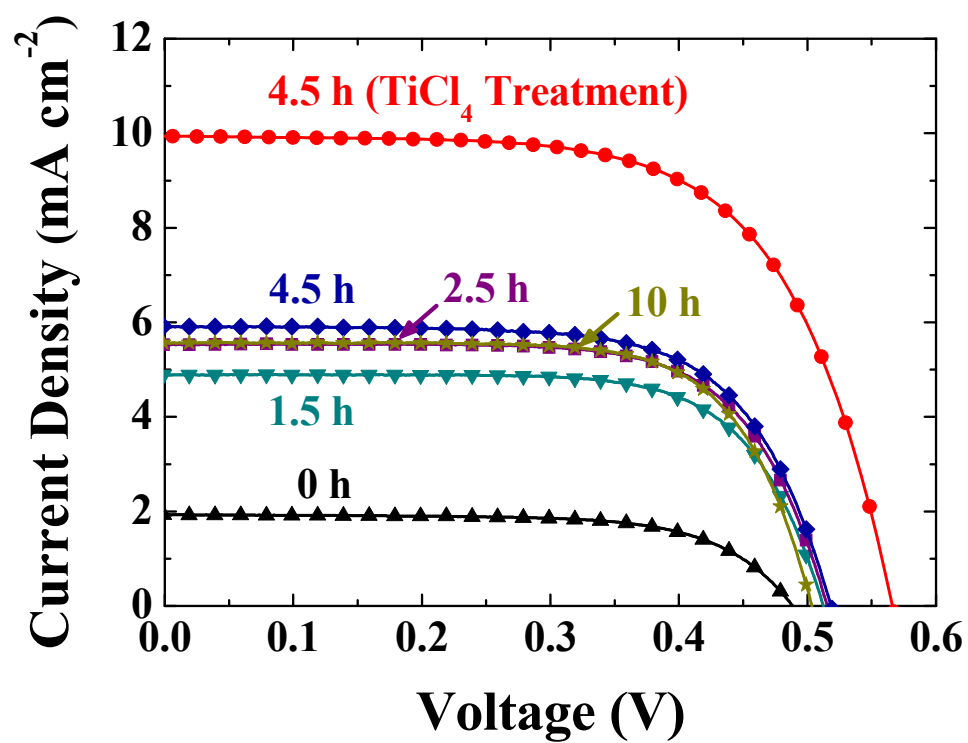


Fig. A1-6. (Color) Photocurrent-voltage curves of the DSSCs based on the nanostructured photoanodes (on the titanium foil) at various hydrothermal dehydration times.

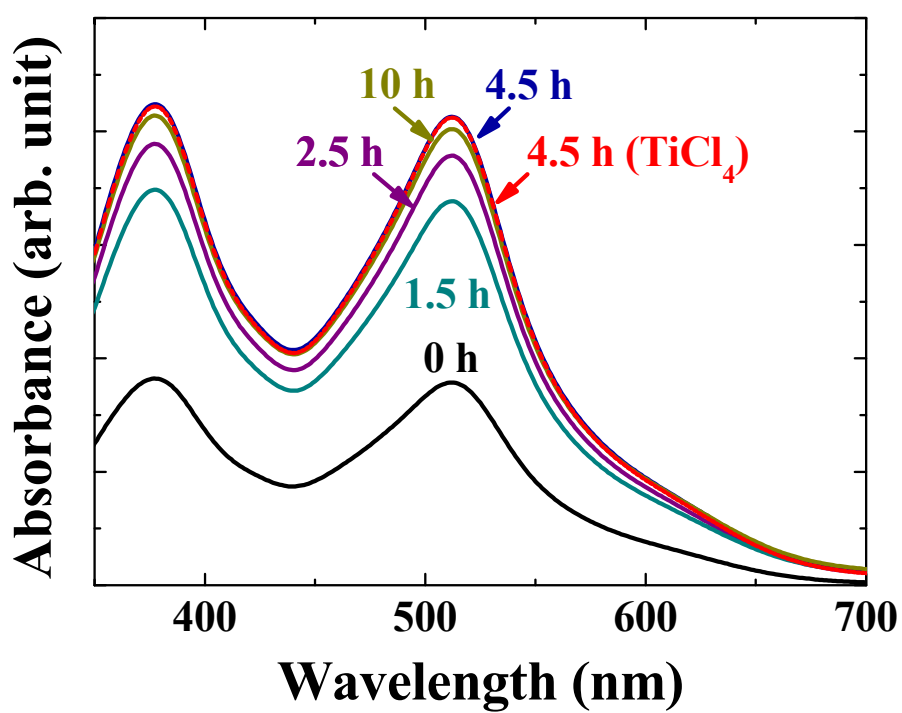


Fig. A1-7. (Color)) UV-Vis absorption spectra of N719 desorbed from photoanodes in 0.1 M NaOH solution.

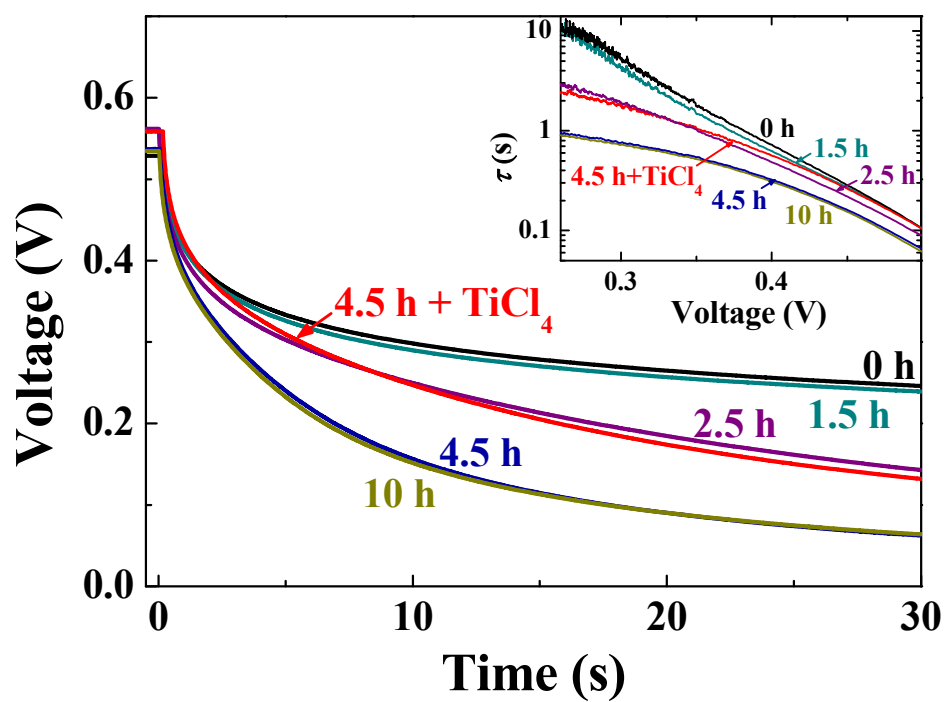


Fig. A1-8. (Color) Experimental decay results of  $V_{oc}$  for the DSSCs. The inset shows the electron lifetimes derived from the decay results.

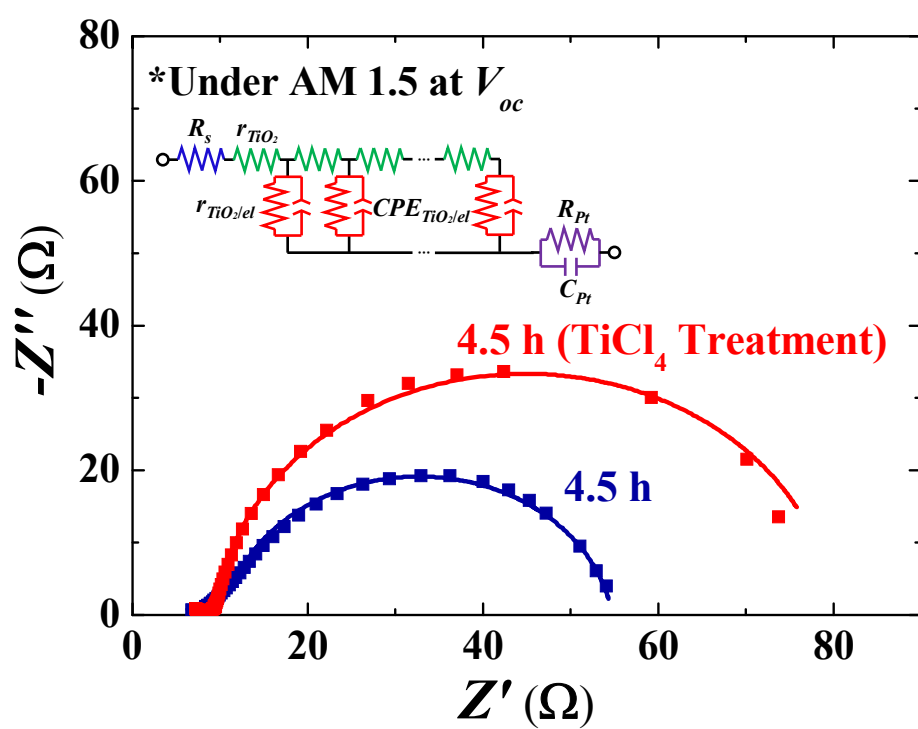


Fig. A1-9. (Color) Nyquist plots for the DSSCs (hydrothermal dehydration time of 4.5 h) with and without TiCl<sub>4</sub> treatment.

To achieve the optimum solar-cell performance, several factors need to be considered: the amount of dye adsorption and charge recombination [22-24]. The UV-Vis absorption spectra was used to quantify the amount of adsorbed dye, as shown in Fig. A1-7 and Table A1-1. While the amount of adsorbed dye increased with dehydration, the 10-h sample showed slightly reduced dye adsorption. The prolonged reaction time leads to the grain growth at the surface of the 1-D nanotubes which causes the diminished dye adsorption.

To examine the charge-recombination rate, open-circuit voltage decay measurement was carried out (Fig. A1-8) and the corresponding decay time was calculated (inset of Fig. A1-8) [25-29]. The rate of decay is found to be more rapid when the hydrothermal dehydration time is increased. This is because the enlarged surface area of the 1-D TiO<sub>2</sub> porous nanostructures provides more trapping sites, and facilitating the charge recombination with I<sub>3</sub><sup>-</sup> in the electrolyte. Various types of defects can exist at the surface of TiO<sub>2</sub> nanostructures, such as hydroxyl group, oxygen vacancy, bridge-bonded oxygen, five-fold coordinated Ti, etc. [30,31]. Consequently, the net effect of the amount of adsorbed dye and charge recombination gives rise to the optimum efficiency with the 4.5-h dehydration. The photovoltaic properties are summarized in Table A1-1.

To suppress the recombination of charge in photoelectrode, surface passivation using TiCl<sub>4</sub> was carried out (Fig. A1-6). The TiCl<sub>4</sub> treatment enhanced

the short-circuit current and power-conversion efficiency of DSSC by ~68% (5.91 to 9.94 mA cm<sup>-2</sup>) and ~79% (2.05% to 3.66%), respectively, despite the similar dye-loading amount (Fig. A1-7). Furthermore, the decay rate improved (Fig. A1-8), which indicates reduced recombination at the TiO<sub>2</sub>/electrolyte interface by the TiO<sub>2</sub> passivation [32]. The thickness of passivation layer (approximately 1 nm) can be deduced by diffraction (Fig. A1-4). Therefore,  $V_{oc}$  of TiCl<sub>4</sub>-treated cell increase ~0.04 V due to the increased carrier lifetime.

To further characterize the charge recombination and transport behavior, the impedance analysis was performed (Fig. A1-9) [33,34]. By fitting the Nyquist plot based on the equivalent-circuit model, the recombination resistance improved with the TiCl<sub>4</sub> treatment (from  $44.0 \pm 0.6$  to  $70.2 \pm 0.8 \Omega$ ). Furthermore, the charge-transport resistance within TiO<sub>2</sub> nanotube is also improved from  $11.5 \pm 0.5$  to  $5.4 \pm 0.2 \Omega$ . Both of these changes can be explained by the existence of thin TiO<sub>2</sub>-coating layer induced from TiCl<sub>4</sub> treatment, which passivates charge-trapping sites on the nanotube surface and enhances the connectivity among the highly-oriented porous nanotube array.

A schematic illustration is shown in Fig. A1-10 for the nanostructural evolution on the Ti foil with various treatments. First, vertically aligned Na<sub>2</sub>Ti<sub>2</sub>O<sub>5</sub>·H<sub>2</sub>O nanowire array are obtained, and converted to protonated 1-D bititanate (H<sub>2</sub>Ti<sub>2</sub>O<sub>5</sub>·H<sub>2</sub>O) nanowires through an ion-exchange reactions. After



hydrothermal dehydration, highly-oriented TiO<sub>2</sub> nanocrystallites begin to form on nanowires by dissolution and nucleation processes. During the course of reaction, nanotubes composed of oriented and truncated octahedra are straightforwardly synthesized. Finally, with the TiCl<sub>4</sub> passivation, optimized photoelectrode is obtained with the improved carrier lifetime.

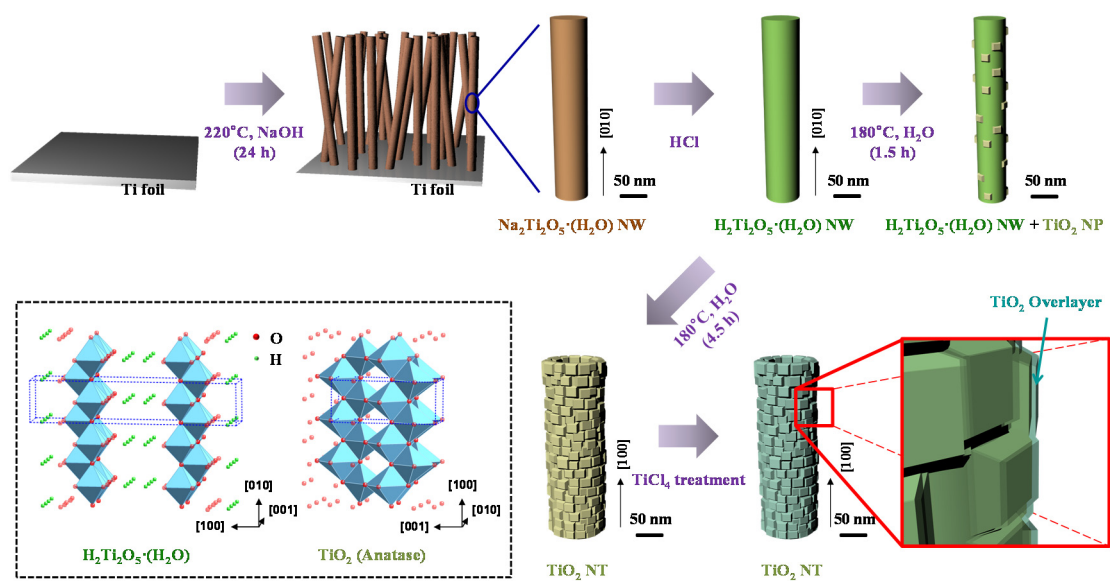


Fig. A1-10. (Color) Schematic flow of nanostructured electrodes with various treatments, and a scheme for the crystal structures of  $\text{H}_2\text{Ti}_2\text{O}_5 \cdot \text{H}_2\text{O}$  and anatase  $\text{TiO}_2$  in the inset.

#### **A.1.4. Conclusion**

Vertically-oriented and hierarchical 1-D TiO<sub>2</sub> nanostructures are synthesized on Ti substrate through a facile hydrothermal route, and the topotactic transformation of nanostructures in association with the hydrothermal dehydration process is systematically investigated. The resulting porous 1-D nanotubes are adopted as photoelectrodes in DSSCs, and the cells exhibit an enhanced dye loading by more than a factor of three by taking advantage of truncated wedge-shape nanostructures, compared to that of the as-prepared nanowire DSSC. The TiCl<sub>4</sub> treatment on the porous nanostructure effectively reduces the charge transfer from TiO<sub>2</sub> to electrolyte by passivating the surface defects, and also enhances charge transport by improving connectivity within nanoparticles. As a result, power-conversion efficiency is increased ~79% under back-side illumination.

### A.1.5. References

1. D. Kuang, J. Brilliet, P. Chen, M. Takata, S. Uchida, H. Miura, K. Sumioka, S. M. Zakeeruddin, and M. Grätzel, "Application of Highly Ordered TiO<sub>2</sub> Nanotube Arrays in Flexible Dye-Sensitized Solar Cells," *ACS Nano* **2**, 1113 (2008).
2. Y.-T. Kim, S. Hwang, J.-H. Hong, and S.-D. Lee, "Alignment Layerless Flexible Liquid Crystal Display Fabricated by an Imprinting Technique at Ambient Temperature," *Appl. Phys. Lett.* **89**, 173506 (2006).
3. Y.-C. Chen, Y.-K. Hsu, Y.-G. Lin, Y.-K. Lin, Y.-Y. Horng, L.-C. Chen, and K.-H. Chen, "Highly Flexible Supercapacitors with Manganese Oxide Nanosheet/Carbon Cloth Electrode," *Electrochim. Acta* **56**, 7124 (2011).
4. P. Zhang, J. Qiu, Z. Zheng, G. Liu, M. Ling, W. Martens, H. Wang, H. Zhao, and S. Zhang, "Free-Standing and Bendable Carbon Nanotubes/TiO<sub>2</sub> Nanofibres Composite Electrodes for Flexible Lithium Ion Batteries," *Electrochim. Acta* **104**, 41 (2013).
5. S. Ito, N. L. C. Ha, G. Rothenberger, P. Liska, P. Comte, S. M. Zakeeruddin, P. Pechy, M. K. Nazeeruddin, and M. Grätzel, "High-Efficiency (7.2%) Flexible Dye-Sensitized Solar Cells with Ti-Metal Substrate for Nanocrystalline-TiO<sub>2</sub> Photoanode," *Chem. Commun.* **38**, 4004 (2006).
6. A. Mihi, C. Zhang, and P. V. Braun, "Transfer of Preformed 3D Photonic

- Crystals onto Dye Sensitized Solar Cells,” *Angew. Chem. Int. Ed.* **50**, 5712 (2011).
7. J. W. Lee, J. O. Choi, J.-E. Jeong, S. Yang, S. H. Ahn, K.-W. Kwon, and C. S. Lee, “Energy Harvesting of Flexible and Translucent Dye-Sensitized Solar Cell Fabricated by Laser Assisted Nano Particle Deposition System,” *Electrochim. Acta* **103**, 252 (2013).
  8. M. Dürr, A. Schmid, M. Obermaier, S. Rosselli, A. Yasuda, and G. Nelles, “Low-Temperature Fabrication of Dye-Sensitized Solar Cells by Transfer of Composite Porous Layers,” *Nat. Mater.* **4**, 607 (2005).
  9. T. Miyasaka, and Y. Kijitori, “Low-Temperature Fabrication of Dye-Sensitized Plastic Electrodes by Electrophoretic Preparation of Mesoporous TiO<sub>2</sub> Layers,” *J. Electrochem. Soc.* **151**, A1767 (2004).
  10. K. Fan, J. Chen, F. Yang, and T. Peng, “Self-Organized Film of Ultra-Fine TiO<sub>2</sub> Nanotubes and its Application to Dye-Sensitized Solar Cells on a Flexible Ti-Foil Substrate,” *J. Mater. Chem.* **22**, 4681 (2012).
  11. Y. Xiao, J. Wu, G. Yue, J. Lin, M. Huang, Z. Lan, and L. Fan, “Electrodeposition of High Performance PEDOT/Ti Counter Electrodes on Ti Meshes for Large-Area Flexible Dye-Sensitized Solar Cells,” *Electrochim. Acta* **85**, 432 (2012).
  12. K. Shankar, J. I. Basham, N. K. Allam, O. K. Varghese, G. K. Mor, X. Feng,

- M. Paulose, J. A. Seabold, K.-S. Choi, and C. A. Grimes, "Recent Advances in the Use of TiO<sub>2</sub> Nanotube and Nanowire Arrays for Oxidative Photoelectrochemistry," *J. Phys. Chem. C* **113**, 6327 (2009).
13. J. Wang and Z. Lin, "Dye-Sensitized TiO<sub>2</sub> Nanotube Solar Cells: Rational Structural and Surface Engineering on TiO<sub>2</sub> Nanotubes," *Chem. Asian J.* **7**, 2754 (2012).
  14. M. Ye, D. Zheng, M. Lv, C. Chen, C. Lin, and Zhiqun Lin, "Hierarchically Structured Nanotubes for Highly Efficient Dye-Sensitized Solar Cells," *Adv. Mater.* **25**, 3039 (2013).
  15. B. Liu, J. E. Boercker, and E. S. Aydil, "Oriented Single Crystalline Titanium Dioxide Nanowires," *Nanotechnology* **19**, 505604 (2008).
  16. D.-R. Jung, D. Son, J. Kim, C. Kim, and B. Park, "Highly-Luminescent Surface-Passivated ZnS:Mn Nanoparticles by a Simple One-Step Synthesis," *Appl. Phys. Lett.* **93**, 163118 (2008).
  17. D. Son, D.-R. Jung, J. Kim, T. Moon, C. Kim, and B. Park, "Synthesis and Photoluminescence of Mn-Doped Zinc Sulfide Nanoparticles," *Appl. Phys. Lett.* **90**, 101910 (2007).
  18. X. Wu, Z. Chen, G. Q. (Max) Lu, and L. Wang, "Nanosized Anatase TiO<sub>2</sub> Single Crystals with Tunable Exposed (001) Facets for Enhanced Energy Conversion Efficiency of Dye-Sensitized Solar Cells," *Adv. Funct. Mater.* **21**,

4167 (2011).

19. H. G. Yang and H. C. Zeng, "Synthetic Architectures of  $\text{TiO}_2/\text{H}_2\text{Ti}_5\text{O}_{11} \cdot \text{H}_2\text{O}$ ,  $\text{ZnO}/\text{H}_2\text{Ti}_5\text{O}_{11} \cdot \text{H}_2\text{O}$ ,  $\text{ZnO}/\text{TiO}_2/\text{H}_2\text{Ti}_5\text{O}_{11} \cdot \text{H}_2\text{O}$ , and  $\text{ZnO}/\text{TiO}_2$  Nanocomposites," *J. Am. Chem. Soc.* **127**, 270 (2005).
20. G. S. Herman, Z. Dohnalek, N. Ruzyski, and U. Diebold, "Experimental Investigation of the Interaction of Water and Methanol with Anatase- $\text{TiO}_2$  (101)," *J. Phys. Chem. B* **107**, 2788 (2003).
21. A. Vittadini, A. Selloni, F. P. Rotzinger, and M. Grätzel, "Structure and Energetics of Water Adsorbed at  $\text{TiO}_2$  Anatase 101 and 001 Surfaces," *Phys. Rev. Lett.* **81**, 2954 (1998).
22. J. Kim, H. Choi, C. Nahm, C. Kim, S. Nam, S. Kang, D.-R. Jung, J. I. Kim, J. Kang, and B. Park, "The Role of a  $\text{TiCl}_4$  Treatment on the Performance of CdS Quantum-Dot-Sensitized Solar Cells," *J. Power Sources* **220**, 108 (2012).
23. P. Tiwana, P. Parkinson, M. B. Johnston, H. J. Snaith, and L. M. Herz, "Ultrafast Terahertz Conductivity Dynamics in Mesoporous  $\text{TiO}_2$ : Influence of Dye Sensitization and Surface Treatment in Solid-State Dye-Sensitized Solar Cells," *J. Phys. Chem. C* **114**, 1365 (2010).
24. C. Kim, J. Kim, H. Choi, C. Nahm, S. Kang, S. Lee, B. Lee, and B. Park, "The Effect of  $\text{TiO}_2$ -Coating Layer on the Performance in Nanoporous  $\text{ZnO}$ -Based Dye-Sensitized Solar Cells," *J. Power Sources* **232**, 159 (2013).

25. A. Zaban, M. Greenshtein, and J. Bisquert, "Determination of the Electron Lifetime in Nanocrystalline Dye Solar Cells by Open-Circuit Voltage Decay Measurements," *ChemPhysChem* **4**, 859 (2003).
26. J. Bisquert, A. Zaban, M. Greenshtein, and I. Mora-Seró, "Determination of Rate Constants for Charge Transfer and the Distribution of Semiconductor and Electrolyte Electronic Energy Levels in Dye-Sensitized Solar Cells by Open-Circuit Photovoltage Decay Method," *J. Am. Chem. Soc.* **126**, 13550 (2004).
27. H. Choi, J. Kim, C. Nahm, C. Kim, S. Nam, J. Kang, B. lee, T. Hwang, S. Kang, D. J. Choi, Y.-H. Kim, and B. Park, "The Role of ZnO-Coating-Layer Thickness on the Recombination in CdS Quantum-Dot-Sensitized Solar Cells," *Nano Energy* **2**, 1218 (2013).
28. J. Kim, H. Choi, C. Nahm, J. Moon, C. Kim, S. Nam, D.-R. Jung, and B. Park, "The Effect of a Blocking Layer on the Photovoltaic Performance in CdS Quantum-Dot-Sensitized Solar Cells," *J. Power Sources* **196**, 10526 (2011).
29. J. Kim, H. Choi, C. Nahm, C. Kim, J. I. Kim, W. Lee, S. Kang, B. Lee, T. Hwang, H. H. Park, and B. Park, "Graded Bandgap Structure for PbS/CdS/ZnS Quantum-Dot-Sensitized Solar Cells with a  $\text{Pb}_x\text{Cd}_{1-x}\text{S}$  Interlayer," *Appl. Phys. Lett.* **102**, 183901 (2013).
30. S. Wendt, P. T. Sprunger, E. Lira, G. K. H. Madsen, Z. Li, J. Ø. Hansen, J. Matthiesen, A. Blekinge-Rasmussen, E. Lægsgaard, B. Hammer, and F.



- Besenbacher, “The Role of Interstitial Sites in the  $Ti_3d$  Defect State in the Band Gap of Titania,” *Science* **320**, 1755 (2008).
31. S. M. Prokes, J. L. Gole, X. B. Chen, C. Burda, and W. E. Carlos, “Defect-Related Optical Behavior in Surface Modified  $TiO_2$  Nanostructures,” *Adv. Funct. Mater.* **15**, 161 (2005).
  32. H. Choi, C. Nahm, J. Kim, J. Moon, S. Nam, C. Kim, D.-R. Jung, and B. Park, “The Effect of  $TiCl_4$ -Treated  $TiO_2$  Compact Layer on the Performance of Dye-Sensitized Solar Cell,” *Curr. Appl. Phys.* **12**, 737 (2012).
  33. C. Nahm, H. Choi, J. Kim, S. Byun, S. Kang, T. Hwang, H. H. Park, J. Ko, and B. Park, “A Simple Template-Free 'Sputtering Deposition and Selective Etching' Process for Nanoporous Thin Films and Its Application to Dye-Sensitized Solar Cells,” *Nanotechnology* **24**, 365604 (2013).
  34. C. Nahm, H. Choi, J. Kim, D.-R. Jung, C. Kim, J. Moon, B. Lee, and B. Park, “The Effects of 100 nm-Diameter Au Nanoparticles on Dye-Sensitized Solar Cells,” *Appl. Phys. Lett.* **99**, 253107 (2011).

## Appendix 2.

### **\* Surface-Plasmon-Coupled Photoluminescence from CdS Nanoparticles with Au Films**

#### **A.2.1. Introduction**

Over the past few years, surface-plasmon effects have received much attention because they have provided unique optical properties for a wide range of applications, such as light emitting diodes (LEDs), sensor technology, solar cells, and nanophosphors [1-8]. Surface plasmon modes are waves that propagate along metallic surfaces; namely, they are essentially light waves trapped on the surface by the collective oscillations of free electrons in the metal with photons through their interactions. These phenomena between the surface charges and light waves make the electromagnetic field decay exponentially with distance from the surface [9]. The electromagnetic fields near metallic surfaces strongly affect the optical properties of semiconductor materials. Thus, the density of surface-plasmon states should be modified to enhance the spontaneous emission rate and improve the quantum efficiency of the semiconductor materials [10].

---

\*The work presented in Appendix 2 was accepted for *Solid State Commun.* **152**, 1767 (2012) entitled, "Surface-Plasmon-Coupled Photoluminescence from CdS Nanoparticles with Au Films"

**Jae Ik Kim**, Dae-Ryong Jung, Jongmin Kim, Changwoo Nahm, Sujin Byun, Sungjun Lee, and Byungwoo Park.\*

Strong photoluminescence (PL) emission by surface-plasmon resonance has been reported in several inorganic and organic semiconductors. For example, when Scherer's group changed the type of metal, they obtained a 17-fold enhanced emission of the InGaN quantum wells, which resulted from the energy transfer between the quantum wells and surface plasmons [11]. Pompa's group and Nurmikko's group have shown, respectively, that by using highly-ordered gold nanopatterns and periodic Ag nanoparticle arrays, the fluorescence of CdSe/ZnS core/shell quantum dots was enhanced by 30- and 50-fold [12,13]. Furthermore, several attempts have been made to control the surface-plasmon-resonance frequency by modifying the density of surface-plasmon states with use of metal alloy, metal-poor cermet, or double metallic layer [14-16].

On the other hand, to excite surface-plasmon modes by photon momentum [11,17], special experimental configurations have been designed, such as the dielectric-prism coupler [18,19], grating coupler [20-22], and surface roughness [23-25]. Thus, controlling the density of surface-plasmon states and the plasmon-excitation configuration is considered important for enhancing luminescence properties.

However, there are few reports considering the PL enhancement with respect to the metal-thickness control and its morphological changes at the same time. In this study, the surface-plasmon effects on the PL properties were investigated by

varying the thickness and roughness of Au, combining with the theoretical calculations for the uniform interface. The contribution from the prolonged optical paths was also excluded to consider only the surface-plasmon effect on the PL enhancement.

### **A.2.2. Experimental Section**

Nearly monodispersed CdS nanoparticles were prepared via a liquid-solid-solution method [26-29]. Cadmium chloride ( $\text{CdCl}_2$ , 0.182 g) and sodium sulfide ( $\text{Na}_2\text{S}$ , 0.078 g) were dissolved separately in distilled water (15 ml) by stirring. The  $\text{CdCl}_2$  solution was placed into an autoclave with sodium linoleate ( $((\text{C}_{17}\text{H}_{31})\text{COONa}$ , 0.1 g) and linoleic acid ( $((\text{C}_{17}\text{H}_{31})\text{COOH}$ , 0.2 ml) dissolved in ethanol, and then  $\text{Na}_2\text{S}$  solution was added to the resulting solution. The autoclave was sealed and maintained at  $100^\circ\text{C}$  for 12 h. Then, the resulting mixture was centrifuged and rinsed several times with ethanol, and dried at  $60^\circ\text{C}$  for 5 h.

The Au was deposited on a glass substrate (Corning Pyrex 7740) by rf magnetron sputtering at room temperature. The deposition time was varied from 20 to 3000 s to obtain different Au thicknesses between 1.5 - 220 nm. The sputtered Au films were then post-annealed in a vacuum at  $400^\circ\text{C}$  for 0.5 h to obtain rough surfaces. The CdS nanoparticles dispersed in chloroform ( $\text{CHCl}_3$ ) were mixed with a poly(methyl methacrylate) (PMMA, weight-average molecular

weight ( $M_w$ ) ~996 kg/mol, Aldrich) solution in chlorobenzene ( $C_6H_5Cl$ ) at a volume ratio of 1:15. The PMMA solution was stirred for several hours for complete dissolution, drop-coated onto the substrate, and cured at room temperature to create a 90 nm thin film.

The sample geometry with the PL measurement is shown in the inset of Fig. A2-1. The PL spectra were measured using a spectrofluorometer (FP-6500: JASCO), and the diffused reflectance spectra were recorded on a UV/Vis spectrophotometer (Lambda 20: Perkin-Elmer). Atomic force microscopy (AFM, SPA-400: Seiko Instruments) was used to obtain topographic images of the Au films.

### **A.2.3. Results and Discussion**

Figure A2-1(a) shows the PL spectra from the CdS nanocrystals on different thicknesses of as-deposited Au. For comparison, the emission from the CdS nanocrystals on bare glass without Au film is also included. The PL intensity increased with increasing the Au thickness and gradually saturated at 220 nm, ultimately reaching ~4-fold enhancement at ~550 nm. However, with annealing of the Au film, the PL spectra were further enhanced (~6-fold enhanced with 220 nm thick Au), as shown in Fig. A2-1(b).

The surface-plasmon dispersion relation at the Au/PMMA interface for various Au film thicknesses are illustrated in Fig. A2-2. The dispersion relation can be derived by Maxwell's equations for a three-layer system (dielectric/metal/dielectric) with the dielectric properties known for each layer [30-34]:

$$\frac{\gamma_2 \varepsilon_3}{\gamma_3 \varepsilon_2} + \frac{(\varepsilon_1 \gamma_2 + \varepsilon_2 \gamma_1) + (\varepsilon_1 \gamma_2 - \varepsilon_2 \gamma_1) \exp(-2 \gamma_2 t)}{(\varepsilon_1 \gamma_2 + \varepsilon_2 \gamma_1) - (\varepsilon_1 \gamma_2 - \varepsilon_2 \gamma_1) \exp(-2 \gamma_2 t)} = 0, \quad (1)$$

and the decay constants perpendicular to the interface (parallel to  $z$ -direction) for the three media are:

$$\gamma_i^2 = k^2 - k_0^2 \varepsilon_i = k^2 - \left(\frac{\omega}{c}\right)^2 \varepsilon_i, \quad (2)$$

where  $\varepsilon_i$  and  $\gamma_i$  are the dielectric constant and decay constant for material  $i$ , respectively ( $i = 1$  for glass, 2 for Au, and 3 for PMMA), and  $t$  is the thickness of the Au film. With the free-space wavevector  $k_0 (= 2\pi/\lambda)$ , the surface-plasmon wavevector propagating parallel to the interface ( $x$ -direction) is  $k$ , while the density of surface-plasmon states  $\rho(\hbar\omega)$  in two-dimensional  $k$ -space is given as:

$$\rho(\hbar\omega) = \frac{2\pi k L^2 dk}{(2\pi)^2 d(\hbar\omega)} \frac{1}{L^2} = \frac{d(k^2)}{4\pi d(\hbar\omega)}, \quad (3)$$

where the in-plane area is  $L^2$ . Thus, the density of surface-plasmon states can be obtained by taking the derivative of the surface-plasmon dispersion relation, as shown in the inset of Fig. A2-2. The calculated results show that the density of surface-plasmon states depends strongly on the Au film thickness.

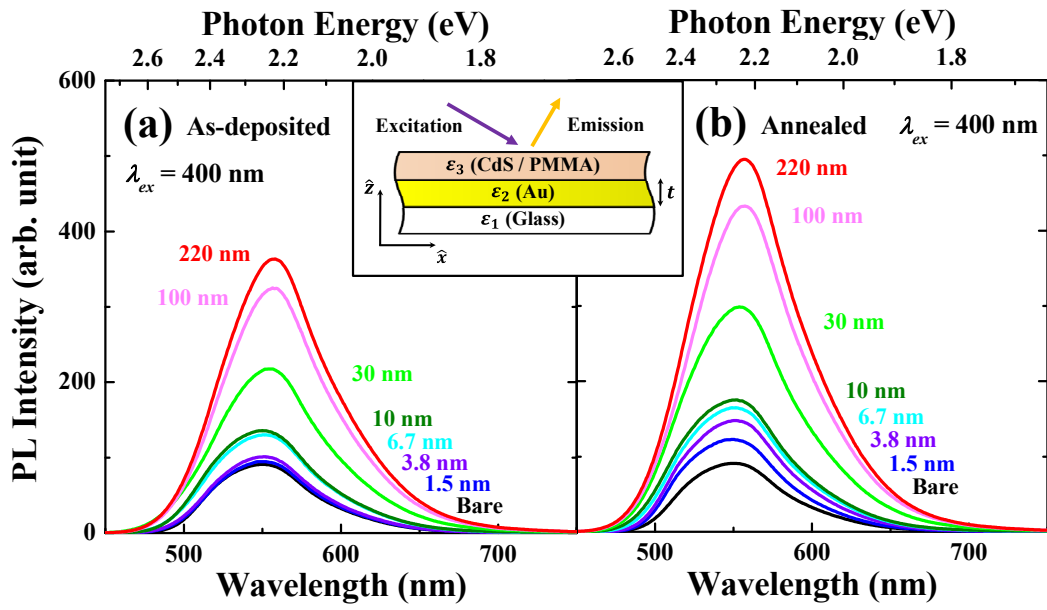


Fig. A2-1. (Color) Photoluminescence spectra of CdS nanoparticles with different thicknesses of Au film: (a) as-deposited and (b) annealed at 400°C for 30 min. The inset shows a schematic figure of a sample geometry and PL configuration.

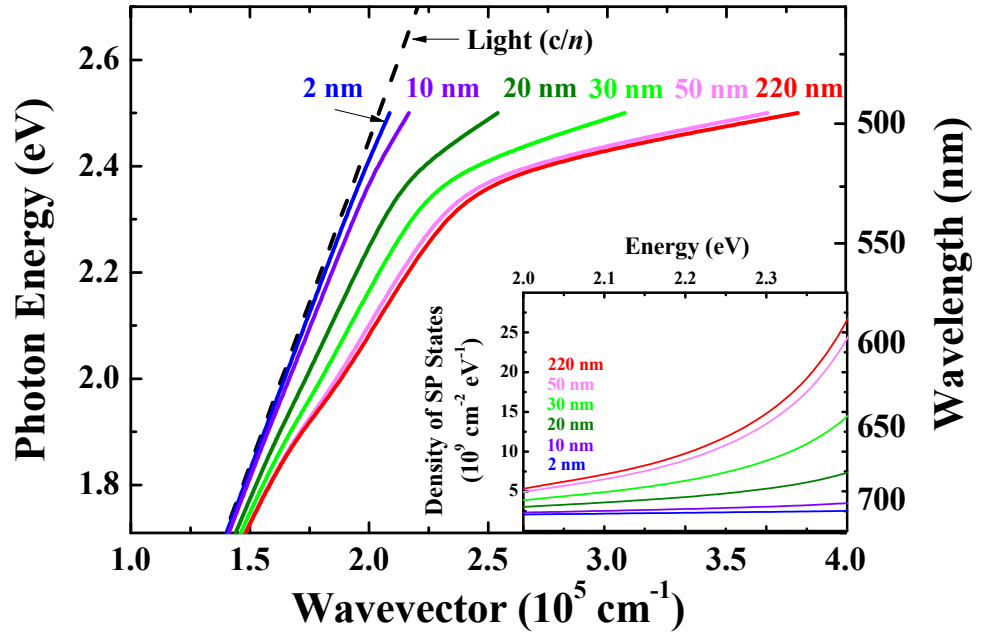


Fig. A2-2. (Color) Dispersion relation of surface plasmon at a planar Au/PMMA interface of a three-layer system for various Au film thicknesses. The light line in PMMA ( $n \cong 1.61$  for the index of refraction) is shown as a dashed line. The inset shows the calculated density of surface-plasmon (SP) states as a function of photon energy for different Au thicknesses.



Due to the back reflection from Au, it is necessary to extract only the plasmon-resonance effect in the PL enhancement, without including the light scattering, which can lead to prolonged optical paths [11,34]. Instead of the apparent PL enhancement factors (Fig. A2-1), the true PL enhancement factors are calculated as:

$$PL \text{ Enhancement Factor} = \frac{PL_{Au} [1 + R_{bare,emi} + (1 - A_{exc}) R_{bare,exc}]}{PL_{bare} [1 + R_{Au,emi} + (1 - A_{exc}) R_{Au,exc}]}, \quad (4)$$

where  $PL_{bare}$  and  $PL_{Au}$  are the PL intensities of bare and Au deposited samples, respectively, and  $R_{Au,emi}$  and  $R_{Au,exc}$  (or  $R_{bare,emi}$  and  $R_{bare,exc}$ ) are the diffused reflectance of the Au film (or bare sample) measured at emission (550 nm) and excitation (400 nm) wavelengths, respectively, as obtained in Fig. A2-3. The absorptance of the CdS/PMMA layer ( $A_{exc}$ ) is so small that it is neglected in Eq. (4).

Figure A2-4(a) shows the calculated PL enhancement, the density of surface-plasmon states (at 2.25 eV), and the lateral roughness (average valley-to-valley distance) for various nominal thicknesses of the Au film (with and without annealing). The density of surface-plasmon states (Eq. (3) and Fig. A2-2) increases with the increase of uniform Au-film thickness and gradually saturates above ~50 nm, which matches well with trend of the PL enhancement. The increased surface-plasmon coupling results from the higher density of surface-plasmon states enhancing the rate of energy transfer for spontaneous emission [35,36].

The AFM images were taken to investigate the changes in the morphologies of the Au films induced by annealing for varying thicknesses, as shown in Figs. A2-4(b) to (e). The increased surface roughness can excite the surface-plasmon resonance more effectively by the possible conversion of photons into the surface-plasmon modes [37-39]. Therefore, further enhanced PL emission was observed with increased lateral roughness, as shown in Fig. A2-4(a).

#### **A.2.4. Conclusions**

The surface-plasmon effects on the PL properties of CdS nanoparticles were examined by varying the thickness and roughness of the Au film. The PL enhancement matched well with the density of surface-plasmon states, which increases with the uniform Au-film thickness and gradually saturates above ~50 nm. By annealing the Au film, further enhanced PL emission was observed due to the improved excitation and coupling of the surface-plasmon modes.

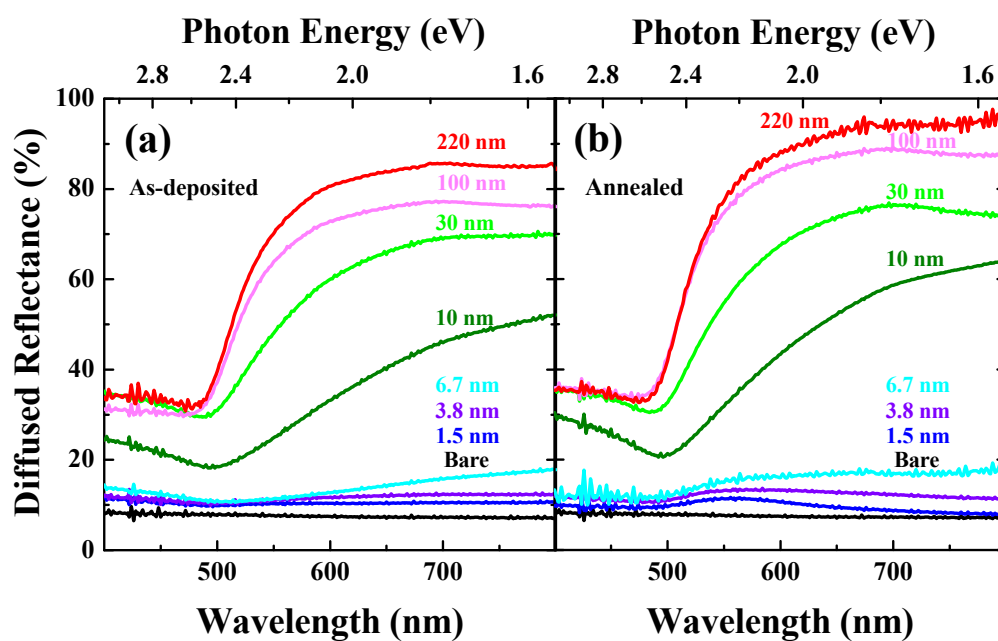


Fig. A2-3. (Color) Diffused reflectance of Au film on glass substrate for various thicknesses of Au film: (a) as-deposited and (b) annealed at 400°C for 30 min.

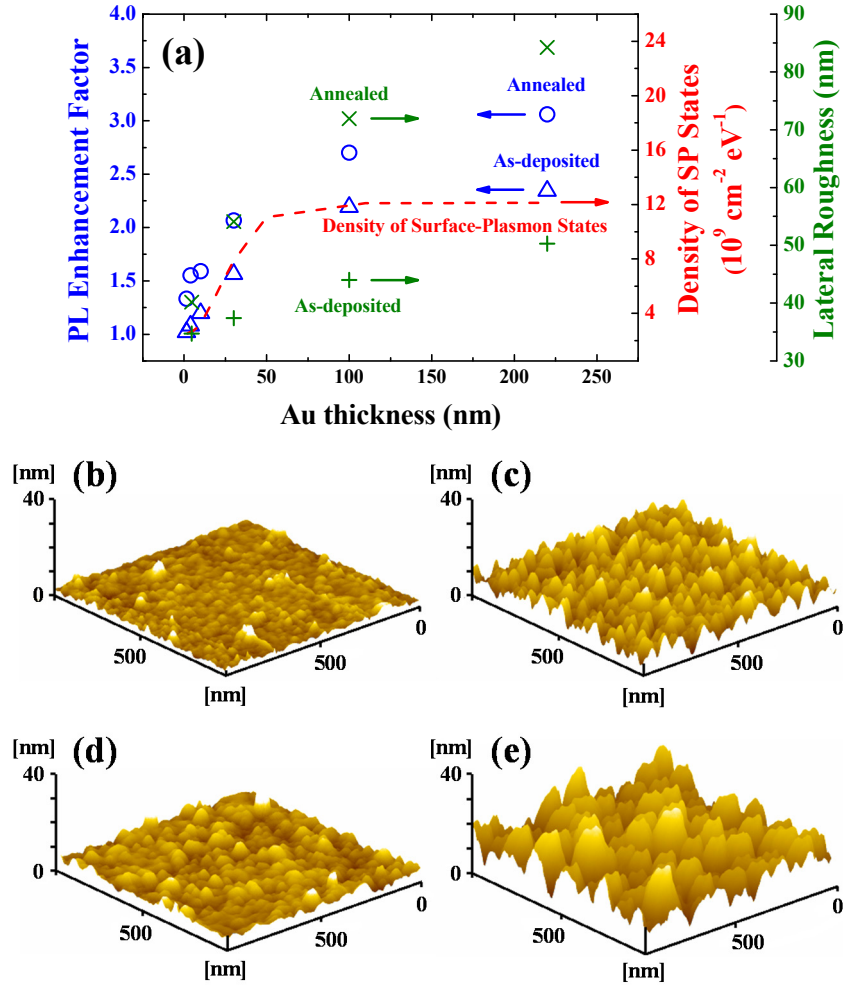


Fig. A2-4. (Color) (a) The calculated PL enhancement factor and lateral roughness as a function of nominal thickness of Au film with and without annealing. The density of surface-plasmon (SP) states at 2.25 eV (from the inset of Fig. A-2) is shown as a dashed line. The AFM images of Au film sputtered on glass substrate at (b) 4.5 nm thickness without annealing, (c) 4.5 nm thickness with annealing, (d) 30 nm thickness without annealing, and (e) 30 nm thickness with annealing.

### A.2.5. References

1. M.-K. Kwon, J.-Y. Kim, B.-H. Kim, I.-K. Park, C.-Y. Cho, C. C. Byeon, and S.-J. Park, “ Surface-Plasmon-Enhanced Light-Emitting Diodes,” *Adv. Mater.* **20**, 1253 (2008).
2. M.-S. Hu, H.-L. Chen, C.-H. Shen, L.-S. Hong, B.-R. Huang, K.-H. Chen, and L.-C. Chen, “Photosensitive Gold-Nanoparticle-Embedded Dielectric Nanowires,” *Nat. Mater.* **5**, 102 (2006).
3. A. B. Dahlin, J. O. Tegenfeldt, and F. Höök, “Improving the Instrumental Resolution of Sensors Based on Localized Surface Plasmon Resonance,” *Anal. Chem.* **78**, 4416 (2006).
4. H. Qi, D. Alexson, O. Glembocki, and S. M. Prokes, “The Effect of Size and Size Distribution on the Oxidation Kinetics and Plasmonics of Nanoscale Ag Particles,” *Nanotechnology* **21**, 085705 (2010).
5. D.-R. Jung, J. Kim, S. Nam, C. Nahm, H. Choi, J. I. Kim, J. Lee, C. Kim, and B. Park, “Photoluminescence Enhancement in CdS Nanoparticles by Surface-Plasmon Resonance,” *Appl. Phys. Lett.* **99**, 041906 (2011).
6. S. M. Lee, K. C. Choi, D. H. Kim, and D. Y. Jeon, “Localized Surface Plasmon Enhanced Cathodoluminescence from  $\text{Eu}^{3+}$ -Doped Phosphor Near the Nanoscaled Silver Particles,” *Opt. Express* **19**, 13209 (2011).
7. D.-R. Jung, J. Kim, C. Nahm, S. Nam, J. I. Kim, and B. Park, “Surface-

- Plasmon-Enhanced Photoluminescence of CdS Nanoparticles with Au/SiO<sub>2</sub> Nanocomposites,” *Mater. Res. Bull.* **47**, 453 (2012).
8. D.-R. Jung, J. Kim, C. Nahm, H. Choi, S. Nam, and B. Park, “Review Paper: Semiconductor Nanoparticles with Surface Passivation and Surface Plasmon,” *Electron. Mater. Lett.* **7**, 185 (2011).
  9. W. L. Barnes, A. Dereux, and T. W. Ebbesen, “Surface Plasmon Subwavelength Optics,” *Nature* **424**, 824 (2003).
  10. I. Gontijo, M. Boroditsky, E. Yablonovitch, S. Keller, U. K. Mishra, and S. P. DenBaars, “Coupling of InGaN Quantum-Well Photoluminescence to Silver Surface Plasmons,” *Phys. Rev. B* **60**, 11564 (1999).
  11. K. Okamoto, I. Niki, A. Shvartser, Y. Narukawa, T. Mukai, and A. Scherer, “Surface-Plasmon-Enhanced Light Emitters based on InGaN Quantum Wells,” *Nat. Mater.* **3**, 601 (2004).
  12. P. P. Pompa, L. Martiradonna, A. D. Torre, F. D. Sala, L. Manna, M. D. Vittorio, F. Calabi, B. Cingolani, and R. Rinaldi, “Metal-Enhanced Fluorescence of Colloidal Nanocrystals with Nanoscale Control,” *Nat. Nanotechnol.* **1**, 126 (2006).
  13. J. H. Song, T. Atay, S. Shi, H. Urabe, and A. V. Nurmikko, “Large Enhancement of Fluorescence Efficiency from CdSe/ZnS Quantum Dots Induced by Resonant Coupling to Spatially Controlled Surface Plasmons,”

- Nano Lett.* **5**, 1557 (2005).
14. D. Y. Lei, J. Li, and H. C. Ong, “Tunable Surface Plasmon Mediated Emission from Semiconductors by using Metal Alloys,” *Appl. Phys. Lett.* **91**, 021112 (2007).
  15. X. Tang, Y. Huang, Y. Wang, W. Zhang, and J. Peng, “Tunable Surface Plasmons for Emission Enhancement of Silicon Nanocrystals using Ag-poor Cermet Layer,” *Appl. Phys. Lett.* **92**, 251116 (2008).
  16. H. Zhao, J. Zhang, G. Liu, and N. Tansu, “Surface Plasmon Dispersion Engineering via Double-Metallic Au/Ag Layers for III-Nitride based Light-Emitting Diodes,” *Appl. Phys. Lett.* **98**, 151115 (2011).
  17. H. Raether, “Surface Plasmons on Smooth and Rough Surfaces and on Gratings,” *Springer Verlag*, Berlin, 1988.
  18. E. Kretschmann, “Die Bestimmung Optischer Konstanten von Metallen durch Anregung von Oberflächenplasmaschwingungen,” *Z. Phys.* **241**, 313 (1971).
  19. A. Otto, “Excitation of Nonradiative Surface Plasma Waves in Silver by the Method of Frustrated Total Reflection,” *Z. Phys.* **216**, 398 (1968).
  20. S. C. Kitson, W. L. Barnes, and J. R. Sambles, “Photoluminescence from Dye Molecules on Silver Gratings,” *Opt. Commun.* **122**, 147 (1996).
  21. J. Kalkman, C. Strohhofer, B. Gralak, and A. Polman, “Surface Plasmon Polariton Modified Emission of Erbium in a Metallodielectric Grating,” *Appl.*

- Phys. Lett.* **83**, 30 (2003).
22. Y.-J. Hung, I. I. Smolyaninov, C. C. Davis, and H.-C. Wu, "Fluorescence Enhancement by Surface Gratings," *Opt. Express* **14**, 10825 (2006).
  23. A. V. Zayats and I. I. Smolyaninov, "Near-Field Photonics: Surface Plasmon Polaritons and Localized Surface Plasmons," *J. Opt. A, Pure Appl. Opt.* **5**, S16 (2003).
  24. J. Zhang and J. R. Lakowicz, "Metal-Enhanced Fluorescence of an Organic Fluorophore using Gold Particles," *Opt. Express* **15**, 2598 (2007).
  25. J. B. You, X. W. Zhang, Y. M. Fan, Z. G. Yin, P. F. Cai, and N. F. Chen, "Effects of the Morphology of ZnO/Ag Interface on the Surface-Plasmon-Enhanced Emission of ZnO Films," *J. Phys. D: Appl. Phys.* **41**, 205101 (2008).
  26. D.-R. Jung, D. Son, J. Kim, C. Kim, and B. Park, "Highly-Luminescent Surface-Passivated ZnS:Mn Nanoparticles by a Simple One-Step Synthesis," *Appl. Phys. Lett.* **93**, 163118 (2008).
  27. D. Son, D.-R. Jung, J. Kim, T. Moon, C. Kim, and B. Park, "Synthesis and Photoluminescence of Mn-Doped Zinc Sulfide Nanoparticles," *Appl. Phys. Lett.* **90**, 101910 (2007).
  28. X. Wang, J. Zhuang, Q. Peng, and Y. Li, "A General Strategy for Nanocrystal Synthesis," *Nature* **437**, 121 (2005).
  29. J. Cho, Y.-W. Kim, B. Kim, J.-G. Lee, and B. Park, "A Breakthrough in the



- Safety of Lithium Secondary Batteries by Coating the Cathode Material with AlPO<sub>4</sub> Nanoparticles,” *Angew. Chem. Int. Ed.* **42**, 1618 (2003).
30. P. Ferguson R. F. Wallis, M. Belakhovsky, J. P. Jadot, and J. Tomkinson, “Surface Plasma Waves in Silver and Gold,” *Surf. Sci.* **76**, 483 (1978).
  31. F. A. Burton and S. A. Cassidy, “A Complete Description of the Dispersion Relation for Thin Metal Film Plasmon-Polaritons,” *J. Lightwave Technol.* **8**, 1843 (1990).
  32. A. Neogi, C.-W. Lee, H. O. Everitt, T. Kuroda, A. Tackeuchi, and E. Yablonovitch, “Enhancement of Spontaneous Recombination Rate in a Quantum Well by Resonant Surface Plasmon Coupling,” *Phys. Rev. B* **66**, 153305 (2002).
  33. W. H. Ni, J. An, C. W. Lai, H. C. Ong, and J. B. Xu, “Emission Enhancement from Metallodielectric-Capped ZnO Films,” *J. Appl. Phys.* **100**, 026103 (2006).
  34. K. H. Cho, S. I. Ahn, S. M. Lee, C. S. Choi, and K. C. Choi, “Surface Plasmonic Controllable Enhanced Emission from the Intrachain and Interchain Excitons of a Conjugated Polymer,” *Appl. Phys. Lett.* **97**, 193306 (2010).
  35. S. A. Maier, “Plasmonics: Fundamentals and Applications,” *Springer*, New York, 2007.
  36. M. J. Romero and J. van de Lagemaat, “Luminescence of Quantum Dots by Coupling with Nonradiative Surface Plasmon Modes in a Scanning Tunneling

- Microscope,” *Phys. Rev. B* **80**, 115432 (2009).
37. L. Salomon, G. Bassou, H. Aourag, J. P. Dufour, F. de Fornel, F. Carcenac, and A. V. Zayats, “Local Excitation of Surface Plasmon Polaritons at Discontinuities of a Metal Film: Theoretical Analysis and Optical Near-Field Measurements,” *Phys. Rev. B* **65**, 125409 (2002).
  38. N. E. Hecker, R. A. Höpfel, N. Sawaki, T. Maier, and G. Strasser, “Surface Plasmon-Enhanced Photoluminescence from a Single Quantum Well,” *Appl. Phys. Lett.* **75**, 1577 (1999).
  39. W. Barnes, “Surface Plasmon–Polariton Length Scales: a Route to Sub-Wavelength Optics,” *Nat. Mater.* **3**, 588 (2004).

## Appendix 3. List of Publications and Presentations

### A.3.1. Publications (International):

1. Byungho Lee,<sup>+</sup> **Jae Ik Kim**,<sup>+</sup> Jaewon Kim, Chohui Kim, Woojin Lee, and Byungwoo Park,<sup>\*</sup> "Oriented Hierarchical TiO<sub>2</sub> Nanowires on Ti Substrate: Evolution of Nanostructures for Dye-Sensitized Solar Cells," *Electrochim. Acta* (in press).
2. **Jae Ik Kim**, Woojin Lee, Taehyun Hwang, Jongmin Kim, Seung-Yoon Lee, Suji Kang, Hongsik Choi, Saeromi Hong, Helen Hejin Park, Taeho Moon,<sup>\*</sup> and Byungwoo Park,<sup>\*</sup> "Quantitative Analyses of Damp-Heat-Induced Degradation in Transparent Conducting Oxides," *Sol. Energ. Mat. Sol. C.* **122**, 282 (2014).
3. **Jae Ik Kim**,<sup>+</sup> Jongmin Kim,<sup>+</sup> Junhee Lee,<sup>+</sup> Dae-Ryong Jung, Hoechang Kim, Hongsik Choi, Sungjun Lee, Sujin Byun, Suji Kang, and Byungwoo Park,<sup>\*</sup> "Photoluminescence Enhancement in CdS Quantum Dots by Thermal Annealing," *Nanoscale Res. Lett.* **7**, 482 (2012).
4. **Jae Ik Kim**, Dae-Ryong Jung, Jongmin Kim, Changwoo Nahm, Sujin Byun, Sungjun Lee, and Byungwoo Park,<sup>\*</sup> "Surface-Plasmon-Coupled Photoluminescence from CdS Nanoparticles with Au Films," *Solid State Commun.* **152**, 1767 (2012).
5. **Jae Ik Kim**, Jae Won Choi, Wonjae Choi, Mallory Mativenga, Jin Jang,<sup>\*</sup> Carlo Kosik Williams, Chuan Che Wang, Eric Mozdy, Jeffrey Cites, Jackson Lai, and Timothy J. Tredwell, "High Performance pMOS Circuits with Silicon-on-Glass TFTs," *Solid-State Electron.* **54**, 299 (2010).

6. Woojin Lee, **Jae Ik Kim**, Seung-Yoon Lee, Jongmin Kim, Hongsik Choi, Joonhyeon Kang, Suji Kang, Taehyun Hwang, Helen Hejin Park, Taeho Moon\*, and Byungwoo Park,\* "Organic-Acid Texturing of Transparent Electrodes Toward Broadband Light Trapping in Thin-Film Solar Cells," *Prog. Photovoltaics*. (submitted)
7. Chohui Kim, Hongsik Choi, **Jae Ik Kim**, Sangheon Lee, Jinhyun Kim, Woojin Lee, Taehyun Hwang, Suji Kang, Taeho Moon,\* and Byungwoo Park,\* "Improving Scattering Layer through Mixture of Nanoporous Spheres and Nanoparticles in ZnO-Based Dye-Sensitized Solar Cells," *Nanoscale Res. Lett.* (2014).
8. Changwoo Nahm,<sup>+</sup> Sungjin Shin,<sup>+</sup> Woojin Lee, **Jae Ik Kim**, Dae-Ryong Jung, Jongmin Kim, Seunghoon Nam, Sujin Byun, and Byungwoo Park,\* "Electronic Transport and Carrier Concentration in Conductive ZnO:Ga Thin Films," *Curr. Appl. Phys.* **13**, 415 (2013).
9. Jongmin Kim, Hongsik Choi, Changwoo Nahm, Chohui Kim, **Jae Ik Kim**, Woojin Lee, Suji Kang, Byungho Lee, Taehyun Hwang, Helen Hejin Park, and Byungwoo Park,\* "Graded Bandgap Structure for PbS/CdS/ZnS Quantum-Dot-Sensitized Solar Cells with a Pb<sub>x</sub>Cd<sub>1-x</sub>S Interlayer," *Appl. Phys. Lett.* **102**, 183901 (2013).
10. Jongmin Kim, Hongsik Choi, Changwoo Nahm, Chohui Kim, Seunghoon Nam, Suji Kang, Dae-Ryong Jung, **Jae Ik Kim**, Joonhyeon Kang, and Byungwoo Park,\* "The Role of a TiCl<sub>4</sub> Treatment on the Performance of CdS Quantum-Dot-Sensitized Solar Cells," *J. Power Sources* **220**, 108 (2012).
11. Dae-Ryong Jung, Jongmin Kim, Seunghoon Nam, Changwoo Nahm, Hongsik Choi, **Jae Ik Kim**, Junhee Lee, Chohui Kim, and Byungwoo

Park, \* "Photoluminescence Enhancement in CdS Nanoparticles by Surface-Plasmon Resonance,"  
*Appl. Phys. Lett.* **99**, 041906 (2011).

### A.3.2. Presentations (International):

1. **Jae Ik Kim**, Woojin Lee, Taehyun Hwang, Seung-Yoon Lee, Suji Kang, Hongsik Choi, Saeromi Hong, Taeho Moon, and Byungwoo Park, "Quantitative Understanding of Damp-Heat-Induced Degradation in Transparent Conducting Oxides,"  
*Materials Research Society (MRS) Fall Meeting*, Boston, MA, December 2013. [Poster by **J. I. Kim**]
2. Byungwoo Park, Hongsik Choi, **Jae Ik Kim**, Seunghoon Nam, Woojin Lee, Sungun Wi, Chohui Kim, and Joonhyeon Kang, "Nanoscale Interface Control for Photoluminescence and Solar-Cell Applications,"  
*The 9th Tsinghua University - University of Tokyo - Seoul National University Student Workshop*, Seoul, Korea, October, 2013.
3. **Jae Ik Kim**, Woojin Lee, Jongmin Kim, Seung-Yoon Lee, Suji Kang, Taeho Moon, and Byungwoo Park, "The Stability and Degradation Mechanisms of ZnO:Al Thin Films in Damp-Heat Environment,"  
*Materials Research Society (MRS) Fall Meeting*, Boston, MA, November 2012. [Poster by **J. I. Kim**]
4. Woojin Lee, **Jae Ik Kim**, Seung-Yoon Lee, Jongmin Kim, Joonhyeon Kang, Suji Kang, Taeho Moon, and Byungwoo Park, "Light Scattering Behavior of Highly Textured ZnO:Al Thin Films by Oxalic and Hydrochloric Acids,"  
*Materials Research Society (MRS) Fall Meeting*, Boston, MA, November 2012. [Poster by **J. I. Kim**]

5. Woojin Lee, **Jae Ik Kim**, Seung-Yoon Lee, Jongmin Kim, Joonhyeon Kang, Suji Kang, Taeho Moon, and Byungwoo Park, "Light Scattering Behavior of Highly Textured ZnO:Al Thin Films by Oxalic and Hydrochloric Acids,"  
Global Photovoltaic Conference 2012 (GPVC2012), Busan, Korea, November, 2012.
6. **Jae Ik Kim**, Woojin Lee, Jongmin Kim, Seung-Yoon Lee, Suji Kang, Taehyun Hwang, Taeho Moon, and Byungwoo Park, "The Stability and Degradation Mechanisms of ZnO:Al Thin Films in Damp-Heat Environment,"  
The 13th Korea - Japan Student Symposium (Seoul National University - Tohoku University), Seoul, Korea, November, 2012.

### A.3.3. Presentations (Domestic):

1. Byungwoo Park, Hongsik Choi, **Jae Ik Kim**, Seunghoon Nam, Woojin Lee, Sungun Wi, Chohui Kim, and Joonhyeon Kang, "Nanoscale Interface Control for Photoluminescence and Solar-Cell Applications,"  
추계 한국세라믹 학회, Jeju, Korea, October 16-18, 2013.
2. Byungwoo Park, Changwoo Nahm, Hongsik Choi, **Jae Ik Kim**, Seunghoon Nam, and Chohui Kim, "Surface Passivation and Surface Plasmon for Luminescence and Solar-Cell Applications,"  
춘계 금속재료 학회, Jeju, Korea, April 25-26, 2013.
3. Byungwoo Park, Changwoo Nahm, Hongsik Choi, **Jae Ik Kim**, Seunghoon Nam, and Chohui Kim, "Surface Passivation and Surface Plasmon for Luminescence and Solar-Cell Applications,"  
춘계 한국전기화학 학회, Changwon, Korea, April 11-12, 2013.

## 국문 초록

태양전지의 고효율, 저가격화를 달성하기 위해, 최근까지 광전 변환 효율에 중요한 역할을 하고 있는 전극 재료들에 대한 집중적으로 연구가 진행되고 있다. 박막 태양전지용 투명전극 재료에 대해서는, 우수한 전기적 특성과 광산란 특성을 갖고, 가격 경쟁력을 갖춘 아연 산화물 기반의 산화물 투명전극이 크게 주목을 받고 있다. 하지만, 이러한 아연 산화물 기반의 투명전극은 내습 안정성이 취약한 특성이 보고되고 있다. 그렇기 때문에, 실제적으로 태양전지의 상용화를 위해 필요한 장기안정성 측면에 문제를 갖게 되어 태양전지에 사용되는 것이 지연되고 있다. 이를 해결하기 위해 전기적 특성이 저하되는 메커니즘을 규명하고, 해결하기 위한 기술 개발이 요구되고 있다.

본 학위논문은 아연 산화물 기반의 투명전극의 내습 안정성과 전기적 특성 저하의 메커니즘에 대하여 보고하고 있다. 1 장에서는 태양전지의 소개로 시작하고 있다. 태양전지의 작동 원리와 구성요소에 대한 설명이 수록되어 있으며, 특히 박막 태양전지 기술의 장점과 특징들을 포함하고 있다. 또한 박막 태양전지의 투명전극 필요성과 요구되는 조건, 재료들에 대해 설명하고 있다. 마지막으로, 이 연구의 필요성과 목적을 제시하였다.

2 장에서는, 아연 산화물 기반의 투명전극 박막의 신뢰성

메커니즘에 대해 자세히 설명하고 있다. 이를 위하여 스퍼터 방법으로 증착된 알루미늄이 도핑된 아연 산화물 박막을 고온·고습 환경에서 신뢰성과 전기적 특성 변화의 메커니즘에 대해 분석하였다. 특성 저하 과정에서 투명전극 박막의 캐리어의 농도와 이동도 변화를 동반한 페르미 준위 이동 관찰되었다. 추가적인 전기적 성질의 온도의존성 및 x-ray photoelectron spectroscopy 를 이용한 표면미세구조 변화 파악 등의 다각적 박막 분석 조합과 모델을 통하여 결정립과 결정립 경계의 전기적 특성 변화를 개별적으로 추출하는 방법을 제안하고, 이를 통해 아연 산화물 기반 투명전극의 신뢰성 저하 메커니즘을 설명하였다. 그리고 3 장에서 결과와 결론에 대해 정리하였다.

마지막으로 부록에서는 염료감응형 태양전지에서 활용될 수 있는 1차원 구조의 다공성 이산화 티타늄 광전극을 제안하고, 그 구조 최적화에 대해 연구한 결과를 정리하였다.

**주요어:** 박막 태양전지, 투명 산화물 전극, 알루미늄 도핑된 아연 산화물, 페르미 준위, 에너지 장벽, 항온·항습 신뢰성 테스트, 염료감응형 태양전지, 다공성 이산화 티타늄 광전극, 수열합성법

학번 : 2010-30776